

# In situ detection of single ions implanted in diamond

---

**Vićentijević, Milan**

**Doctoral thesis / Disertacija**

**2024**

*Degree Grantor / Ustanova koja je dodijelila akademski / stručni stupanj:* **University of Zagreb, Faculty of Electrical Engineering and Computing / Sveučilište u Zagrebu, Fakultet elektrotehnike i računarstva**

*Permanent link / Trajna poveznica:* <https://um.nsk.hr/um:nbn:hr:168:985416>

*Rights / Prava:* [In copyright](#) / [Zaštićeno autorskim pravom.](#)

*Download date / Datum preuzimanja:* **2024-07-01**



*Repository / Repozitorij:*

[FER Repository - University of Zagreb Faculty of Electrical Engineering and Computing repository](#)





University of Zagreb

FACULTY OF ELECTRICAL ENGINEERING AND COMPUTING

Milan Vićentijević

**IN SITU DETECTION OF SINGLE IONS IMPLANTED  
IN DIAMOND**

DOCTORAL THESIS

Zagreb, 2024



University of Zagreb

FACULTY OF ELECTRICAL ENGINEERING AND COMPUTING

Milan Vićentijević

# **IN SITU DETECTION OF SINGLE IONS IMPLANTED IN DIAMOND**

DOCTORAL THESIS

Supervisors: Professor Tomislav Suligoj, PhD  
Milko Jakšić, F. C. A.

Zagreb, 2024



Sveučilište u Zagrebu

FAKULTET ELEKTROTEHNIKE I RAČUNARSTVA

Milan Vićentijević

# **IN SITU DETEKCIJA POJEDINAČNIH IONA IMPLANTIRANIH U DIJAMANT**

DOKTORSKI RAD

Mentori: prof. dr. sc. Tomislav Suligoj  
akademik Milko Jakšić

Zagreb, 2024.

The doctoral thesis was done at the University of Zagreb, Faculty of Electrical Engineering and Computing, at the Department of electronics, microelectronics, computer and intelligent systems and Ruđer Bošković Institute, Division of Experimental Physics, Laboratory for Ion Beam Interactions.

Supervisors: Professor Tomislav Suligoj, PhD  
Milko Jakšić, F.C.A.

This doctoral thesis contains: 107 pages.

Doctoral thesis no.: \_\_\_\_\_

## About the supervisors

Tomislav Suligoj received his Engineer Diploma, MSc, and PhD degrees in electrical engineering from the University of Zagreb, Faculty of Electrical Engineering and Computing (FER), Croatia, in 1995, 1998, and 2001, respectively. Currently, he is a full professor at FER, Department of Electronics, Microelectronics, Computer and Intelligent Systems, teaching courses in electronics and microelectronics. He was a visiting researcher at the University of California, Los Angeles (1999-2001.) and a postdoctoral researcher at the Hong Kong University of Science and Technology (2001-2002.). He has been a Principal Investigator of more than 20 projects so far, supported by government agencies, international companies, and universities. He has published 19 patents and more than 140 papers in journals and conference proceedings in design, measurements, and modelling of electron devices, micro- and nano-electronics, semiconductor technology and integrated circuit design. Prof. Suligoj has received 14 scientific awards including the National Science Award in 2015; the Golden plaque at the innovation exhibition ARCA; Best paper awards at the MIPROMEET conference, Faculty medals "Josip Lončar" for outstanding Doctoral Dissertation, and a Fulbright scholarship. He is a Technical Program Committee member and Chairman of Device Physics Subcommittee at IEEE Bipolar/BiCMOS Circuits and Technology Meeting (BCTM). He is a Steering Committee member of the MIPROMEET conference. He was the President of the Electron Devices/Solid State Circuits Joint Chapter, IEEE Croatia Section from 2010. until 2013. He gave numerous invited talks at conferences, universities, institutions, and companies.

Milko Jakšić was born in 1958. in Požega. He graduated in 1982, got a magister degree in 1986. and a PhD degree in 1989. from the University of Zagreb, Faculty of Science, Department of Physics. He is a senior scientist at the Experimental physics division of Ruđer Bošković Institute in Zagreb. During the last two decades he has been leading the Laboratory for ion beam interactions, that operates accelerator infrastructure based on two electrostatic tandem ion beam accelerators. A wide range of experimental end stations are dedicated to ion beam analysis and ion beam material modification applications. Currently, these are accessible internationally through different contracts and agreements with IAEA, EU projects and CERIC-ERIC consortium. The main research field of Milko Jakšić is development and applications of ion beam analysis as well as material modification techniques based on MeV ion beams. He has published more than 250 research papers, cited more than 3000 times. His current specific

interests include development of techniques using focused ion beams, in particular those based on single ions including deterministic ion implantation. Among them is also an IBIC–ion beam induced charge technique for detector characterization, through which applications RBI group became widely recognized. As a conference chair or co-chair, he organized several most important international conferences in the field of ion beam applications and has also been a leader or associate of many EU and IAEA funded projects. He mentored 4 PhD students, more than 10 master students and in a number of occasions he supervised foreign postdocs and IAEA trainees. Since 2016, he is also a member of Croatian Academy of Sciences and Arts.

## O mentorima

Tomislav Suligoj je diplomirao, magistrirao i doktorirao u polju elektrotehnike na Sveučilištu u Zagrebu, Fakultetu elektrotehnike i računarstva (FER), 1995, 1998. Odnosno 2001. godine. Trenutno je redoviti profesor na Zavodu za elektroniku, mikroelektroniku, računalne i inteligentne sustave FER-a, gdje predaje kolegije u području elektronike i mikroelektronike. Bio je gostujući istraživač na University of California, Los Angeles od 1999. Do 2001. godine te na poslijedoktorskom usavršavanju na Hong Kong University of Science and Technology od 2001. Do 2002. Dosada je vodio više od 20 projekata financiranih od strane državnih institucija, međunarodnih kompanija i sveučilišta. Objavio je 19 patenata i više od 140 radova u časopisima i zbornicima konferencija u području projektiranja, mjerenja i modeliranja elektroničkih elemenata, mikro- i nano-elektronike, poluvodičke tehnologije i projektiranja integriranih sklopova. Prof. Suligoj dobitnik je 14 nagrada uključujući Državnu nagradu za znanost 2015. g., Zlatnu plaketu na izložbi inovacija ARCA, Best paper award na MIPROMEET konferenciji, srebrnu plaketu "Josip Lončar" za posebno istaknutu doktorsku disertaciju te Fulbrightovu stipendiju. Član je Technical Program Committee i Chairman of Device Physics Subcommittee konferencije IEEE Bipolar/BiCMOS Circuits and Technology Meeting (BCTM). Član je Steering Committee konferencije MIPROMEET. Bio je predsjednik Odjela za elektroničke elemente i poluvodičke integrirane sklopove Hrvatske sekcije IEEE 2010. - 2013. Održao je velik broj pozvanih predavanja na međunarodnim konferencijama, sveučilištima, institutima i kompanijama.

Milko Jakšić rođen je 1958. godine u Požegi. Diplomirao je 1982, magistrirao 1986. i doktorirao 1989. na Prirodoslovno-matematičkom fakultetu, Sveučilišta u Zagrebu. Znanstveni je savjetnik u Odjelu za eksperimentalnu fiziku Instituta Ruđer Bošković (RBI) u Zagrebu. Tijekom posljednja dva desetljeća vodio je Laboratorij za interakcije snopa iona koji upravlja akceleratorskom infrastrukturom koja se temelji na dva elektrostatska tandem akceleratora. Širok raspon eksperimentalnih linija posvećen je analizi i modifikaciji materijala ionskim snopovima. Laboratorij, u sklopu međunarodne suradnje, sudjeluje u više projekata s IAEA-om, na EU projektima a također je i dio CERIC-ERIC konzorcija. Glavno istraživačko područje Milka Jakšića je razvoj i primjena analize ionskim snopovima kao i tehnike modifikacije materijala MeVskim ionima. Objavio je više od 250 znanstvenih radova, citiranih više od 3000 puta. Njegovi trenutni interesi uključuju razvoj tehnika koje koriste fokusirane ionske snopove,



posebice one temeljene na pojedinačnim ionima uključujući determinističku ionsku implantaciju. Među njima je i tehnika karakterizacije detektora mjerenjem naboja induciranog ionskim snopom, IBIC, za koju je RBI grupa postala nadaleko priznata. Organizirao je neke od najvažnijih međunarodnih konferencija u području primjene ionskih snopova, a također je kao voditelj ili suradnik sudjelovao u mnogim projektima financiranim od strane EU i IAEA. Bio je mentor 4 doktoranda, više od 10 magistara te je u više navrata bio supervizor inozemnih poslijedoktoranada i IAEA pripravnika. Od 2016. godine je član je Hrvatske akademije znanosti i umjetnosti.

# Acknowledgement

I would like to thank my supervisor at Ruđer Bošković Institute, Dr. Milko Jakšić for help and guidance throughout this PhD project. The high standards and expectations he set are what motivated me to work harder toward my goals. I would also like to thank my supervisor at the University of Zagreb, Prof. Tomislav Suligoj for his support during the PhD. I'm grateful to Michal Pomorski for fabrication of detector electrodes. Many thanks to Tonči Tadić, Zdravko Siketić, Donny Cosic, Andro Kovačić and the rest of the LIBI staff for their help and advice throughout the research process. Special thanks to Željko Periša, for pushing the boundaries of Tandetron particle accelerator in the attempts to obtain exotic, low energy ion beams, used for the research presented in this thesis. I am grateful to Anja, Karla and Matija for putting up with me in the office and for the best farewell party ever. Finally, I'd like to thank my family, especially my wife Barbara, for their love and support in the best and the worst of times.

This work has been carried out within the framework of the EUROfusion Consortium, funded by the European Union via the Euratom Research and Training Programme (Grant Agreement No 101052200 — EUROfusion).

## **Abstract**

Diamond has great potential as substrate material for future quantum devices. Ions implanted into diamond can be activated into color centers. These color centers, also called quantum centers, due to their unique properties, can be used as information carriers in quantum computers – qubits, as well as sensing elements for high precision measurements – quantum sensing or as single photon emitters in quantum optics. Fabrication of devices based on diamond quantum centers requires precise placement of each implanted ion and its efficient subsequent activation. In this work we present deterministic single ion implantation technique for diamond, as a method to precisely place ions into the diamond substrate while detecting each implanted ion by ion beam induced charge. An ion microprobe was used to map the spatial distribution of charge collection efficiency of three diamond detectors with different electrode layout. A printed circuit board was designed as a carrier for both the detector and low noise preamplifier. In this way successful detection of 140 keV copper ions that penetrate on average less than 60 nm was achieved over 800  $\mu\text{m}^2$  implantation site with 100 % detection efficiency and with high uniformity of charge collection efficiency. The proposed detector/preamplifier system with energy resolution of 1.15 keV represents an effective and cost-efficient way of implanting ions in a precise and deterministic way.

**Key words:** ion implantation, diamond, solid-state detectors, low-noise electronics, ion beams

# In situ detekcija pojedinačnih iona implantiranih u dijamant

Kvantna računala svojim mogućnostima daleko premašuju mogućnosti klasičnih računala, dok kvantni senzori zbog svoje visoke osjetljivosti i malih dimenzija, omogućavaju mjerenja najviše preciznosti. Kako bi se iskoristili kvantni efekti u svrhu računanja ili mjerenja razvijeno je više vrsta kvantnih elektroničkih elemenata: elementi bazirani na spinu jezgri atoma unutar poluvodiča, elementi bazirani na elektronskom spinu kvantnih centara u poluvodiču, elementi bazirani na spregnutim elektronima unutar supravodiča koji su trenutno najpopularnije kvantne naprave. Međutim, za pravilno funkcioniranje supravodičkih kvantnih elemenata potrebna je iznimno niska temperatura (ispod 10 mK), što predstavlja glavni problem suvremenih kvantnih računala jer značajno povećava njihove dimenzije i cijenu izrade, a također i ograničava dostupnost takvih komponenata široj populaciji. S druge strane, kvantni elementi bazirani na elektronskom spinu kvantnih centara u poluvodičima bile bi znatno manjih dimenzija, jeftinije i u određenim slučajevima posjedovale mogućnost rada na sobnoj temperaturi. Najpogodniji materijali za realizaciju kako kvantnih računala tako i kvantnih senzora su svakako silicij i dijamant. Dijamant je posebno zanimljiv zbog optički aktivnih centara, od kojih je najpoznatiji kompleks dušik-vakancija (engl. nitrogen vacancy NV), a koji su stabilni na sobnoj temperaturi. Stabilnost dijamantnih kvantnih centara na sobnoj temperaturi, posljedica širokog zabranjenog pojasa (engl. bandgap), koji iznosi 5.47 eV, glavna je prednost dijamanta u odnosu na silicij, i u odnosu na supravodičke kvantne elemente.

Implantacija pojedinačnih iona i njihova naknadna aktivacija jedan je od načina stvaranja kvantnog sustava unutar poluvodičkog materijala. Kako je kvantni sustav zapravo uređeni skup čestica, nužno je implantirati ione na određene pozicije, prema utvrđenom predlošku, da bi se ostvarilo međusobno sprezanje pojedinačnih kvantnih centara. Postoji više načina da se to učini: implantacijom kroz maske, implantacijom kroz vrh sonde mikroskopa atomskih sila (engl. atomic force microscope, AFM), korištenjem fokusiranog ionskog snopa. Od svih navedenih tehnika, implantacija kroz vrh sonde AFM-a ima najbolju nominalnu prostornu rezoluciju (manje od 1 nm). Međutim, prostorna rezolucija implantacije nije definirana isključivo otvorom maske, ili veličinom točke fokusiranog ionskog snopa, već lateralnim rasipanjem implantiranih iona na atomima podloge (kristala). Pri putu iona kroz kristal, dolazi do raspršenja na atomskim elektronima i jezgrama. Efekt raspršenja izraženiji je za ione viših energija i za ione manje mase, jer oni prodiru dublje u kristal. Prema tome, za poboljšanje prostorne rezolucije bolje je

implantirati ione niske energije (manje od 100 keV). Drugi uvjet, za uspješnu implantaciju pojedinačnih iona, je mogućnost detekcije svakog implantiranog iona, u svrhu potvrde broja implantiranih iona. Ion se može detektirati ili prije same implantacije (u ionskim stupicama) ili neposredno po ulasku iona u kristal putem detekcije induciranog naboja u kristalu ili detekcije sekundarnih elektrona ili fotona, emitiranih sa površine kristala.

U ovom radu predstaviti ćemo tehniku detekcije iona, implantiranih u dijamant fokusiranim ionskim snopom, mjerenjem naboja koji upadni ioni induciraju u podlozi (engl. ion beam induced charge, IBIC). Prilikom interakcije upadnog iona sa atomima poluvodiča dolazi do stvaranja parova elektron-šupljina. U prisustvu električnog polja elektroni i šupljine se kreću, driftaju, inducirajući električni signal na obližnje elektrode. Na poluvodički materijal se nanose metalne elektrode (naparavanjem, rasprašivanjem ili drugim postupcima) uz pomoć kojih se postiže razlika električnog potencijala koja uzrokuje električno polje unutar poluvodiča. Poluvodički materijal (kristal) sa dvije ili više elektroda koje uzrokuju električno polje unutar kristala je poluvodički detektor. Broj stvorenih parova elektron-šupljina ovisi o energiji upadnog iona i energiji potrebnoj za stvaranje jednog para elektron-šupljina u materijalu. U dijamantu ta energija iznosi 13 eV dok u siliciju iznosi 3.62 eV. To znači da ista upadna energija iona u dijamantu stvori skoro četiri puta manje parova elektron-šupljina nego u siliciju, što rezultira skoro četiri puta manjim signalom dijamantskog detektora u odnosu na silicijski.

Prostorna razlučivost je, kao što je već navedeno, obrnuto proporcionalna energiji implantiranog iona. Međutim, što je energija iona niža, to manju količinu naboja svaki ion inducira unutar podloge, te je teže detektirati spomenuti ion. Uz to, amplituda signala induciranog na elektrodama detektora ovisi i o raspodjeli električnog polja, tj. o jačini polja u određenom dijelu kristala. Zbog toga veličina koja se mjeri IBIC tehnikom predstavlja odnos induciranog (izmjenjenog) naboja i ukupnog naboja koji je upadni ion kreirao, i naziva se efikasnost kolekcije naboja (engl. charge collection efficiency, CCE). Za detekciju niskih energija potrebno je maksimizirati odnos signal/šum detektora i pretpojačala. Pretpojačalo se koristi u svrhu pojačanja detektorskog signala (naboja induciranog na elektrodama). Pretpojačalo se može pojednostavljeno predstaviti kao operacijsko pojačalo sa kondenzatorom u povratnoj vezi (engl. feedback capacitor,  $C_f$ ) spojenim na invertirajući ulaz, te funkcionira kao integrator naboja, a napon na izlazu proporcionalan je detektorskom naboju. Samo pojačanje pretpojačala ovisi o više faktora ali, ukoliko operacijsko pojačalo ima veliko pojačanje, približno je jednako  $1/C_f$ . Kako bi odnos signal/šum bio visok potrebno je da pretpojačalo ima veliko pojačanje ali i da ukupan šum ne bude veliki. Može se pokazati da je šum minimalan ukoliko je kapacitet ulaznog stupnja pretpojačala jednak ukupnom kapacitetu

na ulaznom čvoru pretpojačala (kapacitet detektora + paraziti kapaciteti). Kako bi se smanjio paraziti kapacitet, detektor se postavlja vrlo blizu pretpojačala. Također, hlađenje pretpojačala i samog kristala se koristi kako bi se smanjio termički šum, iako je u slučaju dijamanta termički šum zanemariv.

Sva mjerenja u sklopu istraživanja predstavljenog u ovom radu izvršena su uz pomoć ionske mikroprobe u Laboratoriju za interakcije ionskih snopova, u Zavodu za eksperimentalnu fiziku Instituta Ruđer Bošković. Ionska mikroproba omogućuje snimanje karakteristika detektora fokusiranim ionskim snopom, što daje visoku prostornu razlučivost snimljenih parametara. Također, variranjem energije i vrste iona mogu se ispitivati karakteristike na različitim dubinama unutar detektora. U predstavljenom istraživanju korišteno je ukupno pet ionskih snopova: protoni energija 4 MeV, 1 MeV, 400 keV i 100 keV, kao i ioni bakra energije 140 keV. Ioni bakra od 140 keV su najmanje prodirući ioni koji se mogu ubrzati u Laboratoriju za interakcije ionskih snopova i koje ionska mikroproba može fokusirati, sa projiciranim dometom od 59 nm u dijamantu. Domet je približno jednak dometu iona dušika energije 50 keV (62 nm), pogodnih za stvaranje dušičnih vakancija sa velikom prostornom preciznošću. U svakom od mjerenja domet iona bio je manji od debljine detektora, tj. ioni su se potpuno zaustavljali u kristalu predajući mu svu svoju energiju. Ukupno četiri dijamanta su korištena, od kojih tri za ispitivanje utjecaja različitog rasporeda elektroda dijamantskog detektora na efikasnost kolekcije naboja. Uzorak D11 je dijamant veličine 4.5 mm × 4.5 mm × 0.3 mm s 12 trakastih elektroda na gornjoj površini i jednom elektrodom koja pokriva cijelu donju površinu kristala. D12 je kristal veličine 3 mm × 3 mm × 0.1 mm s 8 trakastih elektroda na gornjoj i 6 trakastih elektroda na donjoj površini, gdje su donje elektrode okrenute za 90° u odnosu na gornje. Uzorak D13 je dimenzija 3 mm × 3 mm × 0.04 mm s ukupno četiri elektrode na gornjoj površini i jednom elektrodom koja pokriva skoro cijelu donju površinu. Od četiri gornje elektrode samo dvije su korištene u mjerenjima: elektroda spojena direktno na pretpojačalo (osjetljiva elektroda) sa 8 kružnih otvora (jednim promjera 50 μm, tri promjera 30 μm i četiri promjera 10 μm); i elektroda spojena na izvor napona napajanja. Između osjetljive i elektrode napajanja nalazi se nekoliko područja slobodne površine dijamanta koje su, uz kružne otvore osjetljive elektrode, pogodne za ionsku implantaciju.

Za pojačanje detektorskog signala korištena su dva niskošumna pretpojačala: Amptek A250 i XGLab CUBE PRE\_031. Oba pretpojačala se mogu koristiti na niskom tlaku ( $< 10^{-6}$  mbar) te su pogodna za uporabu unutar vakuumske komore ionske mikroprobe. Stoga se oba pretpojačala mogu postaviti blizu detektora i na taj način smanjiti šum. Amptek A250 ima diskretan JFET na ulazu, koji se može mijenjati tako da ulazni kapacitet pretpojačala odgovara

kapacitetu detektora. Također, pojačanje A250 prepojačala se može mijenjati spajanjem jednog od kondenzatora dostupnih na testnoj pločici u povratnu vezu, ili dodavanjem kondenzatora željenog kapaciteta na za to predviđeno mjesto. U ovom istraživanju A250 je korišteno sa  $C_f = 0.1$  pF što daje nominalnu osjetljivost od 185 mV/MeV za dijamantske detektore. XGLab CUBE PRE\_031 je integrirano CMOS prepojačalo sa MOSFET ulazom. Predviđeno je za detektore kapaciteta manjeg od 0.5 pF i za dijamantske detektore ima osjetljivost od 757 mV/MeV. Iako ima bolje performanse u odnosu na A250, karakteristike CUBE PRE\_031 prepojačala se ne mogu mijenjati, tj. ne mogu se prilagoditi različitim detektorima. Štoviše, pošto je malih dimenzija, jednom postavljeno na tiskanu pločicu (engl. printed circuit board, PCB) i spojeno na detektor, ne može se demontirati i koristiti sa drugim detektorom, za razliku od A250 koje se može koristiti sa neograničenim brojem detektora. To je ujedno i glavni nedostatak CUBE PRE\_031 prepojačala. Uzorak D11 korišten je isključivo sa Amptek A250 prepojačalom, dok su D12 i D13 korišteni sa XGLab CUBE PRE\_031. Za tu svrhu razvijene su dvije tiskane pločice. RBI Implantation Board V2.0 je FR4 tiskana pločica dizajnirana u sklopu istraživanja za CUBE PRE\_031 i dijamantski detektor veličine do 5 mm × 5 mm te omogućuje napajanje prepojačala (uz filtriranje napona) i mjerenje signala preko jednog DB9 konektora. RBI Implantation Board V2.0 korištena je s D12 dijamantom. Za D13 uzorak, dizajn tiskane pločice je unaprijeđen te je napravljena RBI Implantation Board v2.2 od AlN, keramičkog materijala visoke termičke vodljivosti, pogodna za hlađenje. Pored tri spomenuta dijamanta korišten je i N1 uzorak, dijamant veličine 2 mm × 2 mm × 0.5 mm sa planarnim rasporedom elektroda: kvadratne elektrode dimenzija 1 mm × 1 mm na gornjoj i 2 mm × 2 mm na donjoj površini. Planarni raspored elektroda rezultira približno ravnomjernom raspodjelom električnog polja unutar kristala (osim u neposrednoj blizini rubova elektroda). Pored toga, niski kapacitet N1 od samo 0.2 pF (najniži od svih korištenih detektora) čini ovaj uzorak pogodnim za energijsku kalibraciju (umjeravanje) rezultata. Stoga je N1 u prvom nizu eksperimenata (pokusa) spajan na Amptek A250 prepojačalo kako bi se kalibrirali rezultati dobijeni D11 detektorom. Kasnije je N1 montiran na RBI Implantation Board v2.2 i spojen na CUBE PRE\_031 kako bi se kalibrirali rezultati dobiveni sa D12 i D13 detektorima. Za umjeravanje korištene su gama zrake iz referentnog <sup>241</sup>Am radioaktivnog izvora.

Mjerenja sa 4 MeV i 400 keV protonima i D11 dijamantom pokazala su značajnu razliku u raspodjeli CCE-a duboko u kristalu i blizu površine, kada je aktivno područje detekcije između dvije trakaste elektrode na gornjoj površini kristala. Pri nižim energijama i dubinama prodiranja vrijednost i uniformnost CCE-a u aktivnom području značajno opada. Ovaj rezultat korišten je kao referentni za kasnija mjerenja sa D12. Nažalost, ova mjerenja su pokazala da D11 ima

velike nedostatke, što se vidjelo i iz mjerenja sa 400 keV protonima sa planarno spojenim elektrodama (tri gornje trakaste elektrode spojene na pretpojačalo dok je donja elektroda spojena na izvor napona) i iz strujno-naponske karakteristike. Neravnomjerna raspodjela CCE-a, nelinearna promjena struje curenja sa primijenjenim naponom i potreba za prethodnim ozračivanjem uzorka da bi se postigao stabilni odziv – takozvani efekt pripreme (engl. priming effect), efekti su koji onemogućuju korištenje D11 dijamanta za implantaciju niskoenergijskih iona. D11 je jedini od četiri korištena dijamanta koji ima nelinearnu strujno-naponsku karakteristiku i neželjene efekte. S obzirom da su sva četiri uzorka dijamanti najviše čistoće, komercijalno dostupni, vjerojatan uzrok je ispravljački kontakt između elektroda i samog kristala.

D12, spojen u takozvanom međutrakastom (engl. interstrip) načinu rada: jedna trakasta elektroda na gornjoj površini spojena na pretpojačalo a susjedna elektroda na izvor napajanja, dok su sve ostale elektrode “u zraku” (nisu spojene); demonstrirao je uspješnu detekciju 1 MeV, 400 keV i 100 keV protona kao i 140 keV iona bakra. Na svim mapama raspodjele CCE-a vide se konture osjetljive elektrode i elektrode napajanja. Uspješna detekcija plitkih iona, kao što su ioni bakra energije 140 keV, značajan je pokazatelj mogućnosti primjene tehnike determinističke implantacije pojedinačnih iona u dijamant. Međutim, nizak CCE (posebno u slučaju implantacije iona bakra) i još važnije, niska efikasnost detekcije iona pokazuje da ovakav raspored elektroda nije pogodan za procesiranje velikih kvantnih elemenata.

D13 detektor dizajniran je upravo kako bi riješio problem niske efikasnosti detekcije. Inicijalna testiranja sa 400 keV i 100 keV protonima rezultirala su efikasnošću detekcije od 100 % i vrijednosti CCE-a do 100%. Oba rezultata su značajni pomaci u odnosu na D12 gdje je maksimalna postignuta vrijednost CCE-a bila 50 %. Naknadnom implantacijom iona bakra energije 140 keV pokazano je da efikasnost detekcije ostaje jako visoka, 100 % u slučaju 10  $\mu\text{m}$  i 30  $\mu\text{m}$  otvora u osjetljivoj elektrodi, a u slučaju 50  $\mu\text{m}$  otvora efikasnost detekcije manja je od 100 % samo u centru. Važno je napomenuti da ioni bakra ovako niske energije ne mogu proći kroz elektrode, te je implantacija u dijamant moguća samo kroz kružne otvore u osjetljivoj elektrodi ili u regijama između osjetljive i elektrode napajanja. Iako su dobiveni rezultati obećavajući, uniformnost CCE-a ipak nije visoka. Naime, CCE je uvijek veći blizu rubova elektrode nego u sredini otvora. Ta neujednačenost je najizraženija u slučaju 50  $\mu\text{m}$  otvora u osjetljivoj elektrodi, a najmanje izražena za 10  $\mu\text{m}$  otvor. Jednostavno rješenje za povećanje uniformnosti bilo bi implantacija kroz male otvore u elektrodi, ali to bi značajno ograničilo veličine kvantnih elemenata koje se mogu na ovaj način proizvesti. Drugo rješenje je uvođenje lateralnog električnog polja. Naime, pri implantaciji kroz otvore u osjetljivoj elektrodi donja



elektroda je bila na visokom naponu, stvarajući električno polje paralelno s pravcem kretanja iona unutar dijamanta (longitudinalno polje). Ukoliko bi se visoki napon doveo i na gornju elektrodu napajanja, u područjima između osjetljive i gornje elektrode napajanja nastalo bi električno polje koje ima i longitudinalnu i lateralnu komponentu. Implantacija iona bakra energije 140 keV u jednom takvom području površine  $800 \mu\text{m}^2$  (dovoljno velikoj za implantaciju  $2 \times 10^5$  iona, tj. stvaranje jednakog broja potencijalnih kvantnih centara) rezultirala je većom uniformnošću CCE-a nego implantacija kroz  $10 \mu\text{m}$  otvor u osjetljivoj elektrodi, iako je površina tog otvora manja za red veličine. Pored toga, D13 spojen na CUBE PRE\_031 ostvario je energijsku razlučivost od  $1.15 \pm 0.08$  keV, ispod 1 % energije implantiranih iona bakra. Vrijednost CCE-a za 140 keV ione bakra povećana je sa 10 % postignutih za D12 na 20 % za D13. Iako je to povećanje značajno, ipak je vrijednost CCE-a još uvijek daleko od željenih 100 %. Uzimajući u obzir vrijednost CCE-a na malim dubinama u kristalu, procijenjeno je da donja granica detektibilne energije D13 detektora spojenog na CUBE PRE\_031 pretpojačalo iznosi  $18.7 \pm 0.2$  keV, što je bi omogućilo uspješnu detekciju 50 keV iona dušika.

Predstavljena metoda implantacije i sustav detektor/pretpojačalo ima značajnih prednosti u odnosu na ostale tehnike. Efikasnost detekcije od 100 % omogućuje determinističku implantaciju velikog broja iona čak i kada ioni imaju nisku energiju, što nije slučaj za metodu detekcije sekundarnih elektrona. U odnosu na implantaciju iz ionskih zamki, predložena metoda je jeftinija, energijski efikasnija i može implantirati veliki broj iona (do  $2 \times 10^5$ ) za relativno kratko vrijeme, što sa ionskim zamkama nije moguće, zbog njihovog ograničenog kapaciteta. Iako je fokus ovog istraživanja bila implantacija u dijamant, Implantation Board v2.2 i CUBE PRE\_031 pretpojačalo mogu biti korišteni i s ostalim poluvodičkim detektorima (na primjer SiC), što pokazuje svestranost predloženog sustava. Aktivacija implantiranih iona u funkcionalne kvantne centre ostaje značajan problem u stvaranju kvantnih elemenata. Iako predložena metoda ne nudi direktno rješenje, napredak u detekciji niskoenergijskih iona može doprinijeti određivanju procesnih parametara (kao što je optimalan broj implantiranih iona po poziciji) za efikasniju aktivaciju implantiranih iona.

**Ključne riječi:** ionska implantacija, dijamant, poluvodički detektori, niskošumna elektronika, ionski snopovi

# Contents

<b>1</b>	<b>Introduction.....</b>	<b>1</b>
1.1	Quantum computing.....	1
1.2	Quantum sensing.....	2
1.3	Fabrication of quantum devices.....	3
<b>2</b>	<b>Diamond as a detector material.....</b>	<b>6</b>
2.1	Diamond structure and basic properties.....	6
2.2	Defects in diamond.....	8
2.3	Surface properties of diamond.....	10
2.4	Production of diamond.....	11
<b>3</b>	<b>Signal generation and processing.....</b>	<b>13</b>
3.1	Interaction of ionizing radiation with diamond.....	13
3.2	Signal generation in diamond.....	16
3.3	Noise in detectors.....	20
3.4	Processing of detector signal.....	21
3.5	Noise in pulse processing systems.....	31
3.6	Methods for noise mitigation.....	34
<b>4</b>	<b>Detector development and experimental methods.....</b>	<b>36</b>
4.1	Ion microprobe end station and IBIC technique.....	36
4.2	Diamond samples.....	38
4.3	Readout electronics.....	41
4.3.1	Amptek A250.....	42
4.3.2	XGLab CUBE PRE_031.....	43
4.3.3	Signal processing system.....	44
4.4	PCB and detector development.....	45
4.5	Detector/preamplifier cooling system.....	50
4.6	Ion beam selection and measurement process.....	51
4.6.1	Ion beams.....	51

4.6.2	Measurement process .....	54
<b>5</b>	<b>Results and discussion .....</b>	<b>56</b>
5.1	Diamond sample with top strip electrodes .....	56
5.1.1	Calibration of Amptek A250 .....	57
5.1.2	Characterization in planar mode.....	59
5.1.3	Characterization in interstrip mode .....	61
5.2	Diamond sample with top and bottom strip electrodes .....	64
5.2.1	Floating bottom electrodes .....	65
5.2.2	Biased bottom electrodes.....	73
5.3	Diamond sample with circular implantation sites .....	74
5.3.1	Calibration of CUBE PRE_031 .....	75
5.3.2	Characterization without lateral electric field .....	77
5.3.3	Characterization with lateral electric field.....	83
5.3.4	Characterization at low temperature.....	87
<b>6</b>	<b>Conclusion .....</b>	<b>90</b>
	<b>Bibliography .....</b>	<b>93</b>
	<b>Biography .....</b>	<b>104</b>
	<b>Životopis .....</b>	<b>107</b>

# 1 Introduction

## 1.1 Quantum computing

Quantum computation refers to information processing accomplished by using quantum mechanical systems. The advantage of quantum computers over the classical ones is that quantum computers are significantly faster in performing specific tasks. One of the most well-known quantum algorithms is Shor's algorithm [1], which can factor large numbers exponentially faster than algorithms computable on classical computers. This has important implications for cryptography, which relies on the difficulty of factoring large numbers on classical computers. Further evidence of the power of quantum computers was given by Lov Grover in what's now called Grover's algorithm [2]. A quantum computer running Grover's algorithm could search an unsorted database with  $N$  items in  $O(\sqrt{N})$  time, whereas a classical computer would require  $O(N)$  time to perform the same search. The algorithm works by using the principles of quantum superposition and interference to amplify the amplitude of the correct solution state. Grover's algorithm is one of the most important algorithms in quantum computing and has been widely studied with several physical implementations by different groups [3], [4]. Quantum algorithms have many potential applications, including optimization problems, data analysis, and database searching. Essentially, quantum algorithms exploit the main feature of quantum computers: the ability to search through many possibilities simultaneously, and quickly identify the correct one. The idea of using quantum mechanical systems for computing isn't new. In the early 1980s, Richard Feynman proposed the idea of using quantum computers to simulate complex quantum systems [5], since it proved to be very difficult for classical computers. In 2019, Google had demonstrated, with the Sycamore processor, the supremacy of quantum computers over the classical supercomputers, in performing specific tasks [6].

Quantum bits, or qubits, are the basic function blocks of quantum computers, in the same way bits are the basic function blocks of classical computers. Classical bits can be in one of the two possible states – either 0 or 1. Similarly, a qubit can be in states  $|0\rangle$  and  $|1\rangle$ . However, a qubit can also be in a state formed by the linear combination of states, called superposition,  $\alpha|0\rangle + \beta|1\rangle$ , where  $\alpha$  and  $\beta$  are complex numbers [7, p. 13]. Superposition of states means that a single qubit can be in any state that lies on a sphere in complex space, called Bloch sphere. Representations of a classical bit and a quantum bit are given in fig. 1.1. The fact that qubits can have states other than  $|0\rangle$  and  $|1\rangle$ , unlike classical bits that cannot have state other than 0 or 1, is a fundamental advantage of quantum over the classical computers or even supercomputers. To determine the state of a bit, a simple measurement is performed. In the same way when a qubit is measured, the result is either  $|0\rangle$ , with probability  $|\alpha|^2$ , or it's  $|1\rangle$ , with probability  $|\beta|^2$ , where  $|\alpha|^2 + |\beta|^2 = 1$ . All other states can exist only between the initialization of a qubit and the measurement itself.

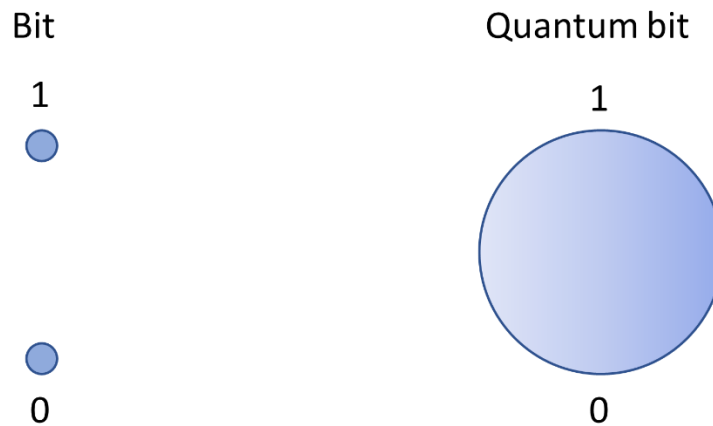


**Figure 1.1:** Representation of a classical bit (left) and a quantum bit (right).

## 1.2 Quantum sensing

In the same way quantum computers utilize quantum effects for faster computation, in quantum sensors, those effects are used to enhance measuring capabilities. The advantage of quantum sensors is the possibility of quantum systems to effectively measure with exceptional accuracy. Quantum sensors utilize the fact that a small change in some physical quantity can have a measurable effect on spin, energy level(s) or some other properties of a quantum system. A single type of quantum system can be used in different sensors. For example, nitrogen vacancy (NV) center, a quantum center in diamond, is used in: magnetic spectroscopy [8], [9], high-

sensitivity temperature measurement [10], nanoscale magnetism [11], [12], and other [13]–[15]. Compared to classical sensors, quantum sensors have much higher sensitivity and are usually designed for measurements at nanoscale [16].

### 1.3 Fabrication of quantum devices

Both quantum computers and quantum sensors are realized as an ordered ensemble of quantum centers, which can be referred to as the quantum system. There are several different ways of physical realization of a quantum system. Qubits based on nuclear spin were among the first to be proposed [17]. However, a single nuclear spin is not easy to measure due to the small size of the nucleus. Therefore, other types of qubits were proposed. The most widely used qubits are superconducting qubits [18]. They are based on Josephson junctions in order to create a two-level system [19]. Depending on the type of operation there are three different modalities of superconducting qubits (illustrated in fig 1.2) Big research groups such as Google [20] or IBM [21] use superconducting qubits as the core of quantum computers. The control of a qubit made of a Cooper pair with a Josephson junction [22] is done via microwave leads. The single qubit operations are performed by sending pulses of microwaves of specific frequencies into the qubit. Quantum computers based on superconducting qubits must be cooled to very low temperatures (below 10 mK) to operate [23, p. 56]. Since it's based on very small magnetic moments this type of quantum system needs to be shielded from external magnetic fields that could cause decoherence. An illustration of a quantum computer based on superconducting qubits is shown in fig 1.3.

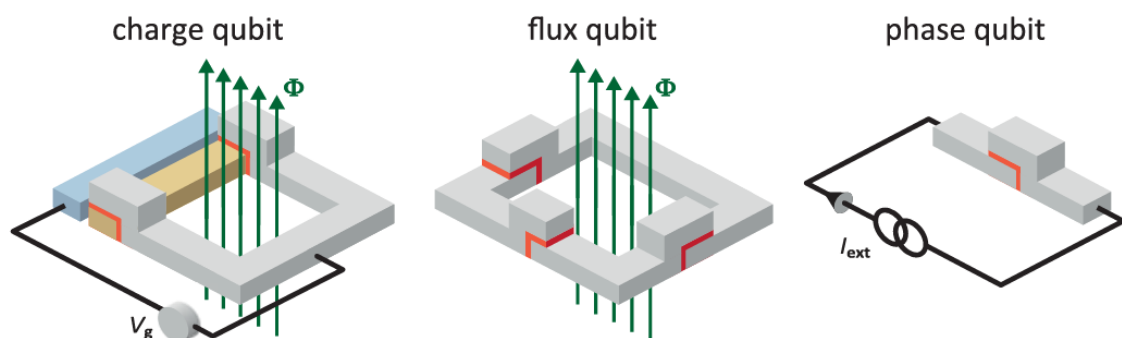


**Figure 1.2:** Three modalities of superconducting qubits: (a) charge, (b) flux and (c) phase. [24]

Another approach to quantum computer implementation is to use trapped ions [25]. In this

## Introduction

setup, lasers are used to ionize atoms which are then trapped in electric potentials [23, p. 58]. Another laser is then used to interact with the qubits. One of the significant advantages of this approach is that, unlike superconducting qubits, qubits based on trapped ions do not need extremely low temperatures to function [26].

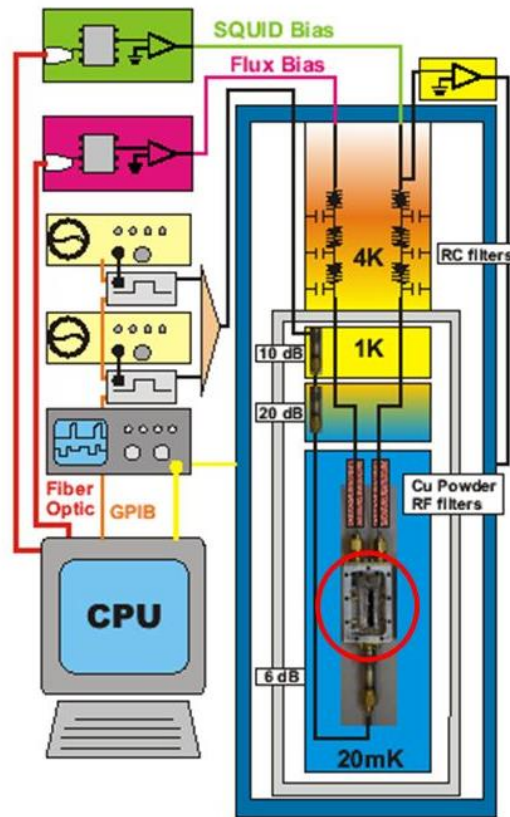


**Figure 1.3:** Illustration of a superconducting quantum computer. The quantum computer is enclosed inside a cooling vessel. The control of a quantum computer is performed by a classical computer. [23, p. 48]

Another approach to create quantum centers is single ion implantation in solid state substrate. It consists of implanting single ions in specific locations in a crystal [27]. A quantum system consists of many quantum centers in a single crystal. The advantage of quantum system in a crystal, over the quantum system in ion traps or a superconducting system, is in its small dimensions, and in case of quantum centers in diamond, functionality at room temperature [28]. For a successful single ion implantation, two requirements must be met: good localization of the implanted ions and ability to successfully detect a single implanted ion. The localization requirement enables implantation of ions in closely packed patterns. Since a quantum system relies on coupling between the individual quantum centers, the ions which create the quantum

## Introduction

centers need to be implanted close to each other. There are several ways to achieve good localization:

- Implantation through a mask [29], [30]
- Implantation through AFM tip [31], [32]
- Implantation using focused ion beams [33], [34]

Of all the techniques, implantation through the AFM tip has the best nominal spatial resolution (less than 1 nm). However, spatial resolution of the implantation is often defined not by the mask, or beam spot size, but by lateral straggling of the implanted ion.

The detection of the implanted ions can be done either before the implantation itself (in the ion traps) or after ions enter the crystal, by means of ion beam induced charge (IBIC) detection [29], [32], or detection of secondary electrons (or photons) emitted from the crystal [27]. Even though deterministic single ion implantation was successfully demonstrated for silicon substrate, further research is needed to increase the useful implantation area of the substrate as well as to adapt the technique for large bandgap materials. One of the most promising large bandgap materials is diamond. Commercially available diamonds can have significant differences in electronic properties between the samples of nominally the same purity. Therefore, further research is needed to determine whether commercially available diamond crystals can be used as substrate for deterministic single ion implantation.

The focus of this work is to determine whether commercial diamond crystal can be used as active substrate for deterministic single ion implantation, together with state-of-the-art readout electronics. In the following chapter a detailed overview of the properties of diamond as a particle detector material, as well as interaction of the ions with diamond, will be given. Also, we will explain the crucial parts of the readout system, their principle of operation and role in the signal processing. Chapter three will explain the development of diamond detectors for deterministic ion implantation. Also, in that chapter we will present the ion implantation system we used for this research. In chapter four we present and discuss the results of the performed measurements. The outcome of the research will be given in the last chapter. Moreover, in this chapter we propose the design of the detector/preamplifier system for ion implantation quantum centers substrate.



## 2 Diamond as a detector material

### 2.1 Diamond structure and basic properties

Diamond is an allotrope of carbon with cubic crystal structure, same as other elements in group IV of the periodic table, such as silicon or germanium. Its structure is a face-centered cubic lattice with two atoms per primitive unit cell as shown in fig. 2.1. The length of the edge of the lattice, lattice constant is  $a_0 = 0.357 \text{ nm}$  [35]. The characteristic of carbon atoms in diamond, compared to other allotropes, such as graphite or graphene, is the hybridization of s and p states form  $sp^3$  orbitals. Overlapping of those orbitals creates strong, covalent bonds between a carbon atom and its four neighbors, in tetrahedral shape. The lattice structure of diamond is the cause of its exceptional properties: high melting temperature, thermal conductivity, small dielectric constant, and mechanical hardness.

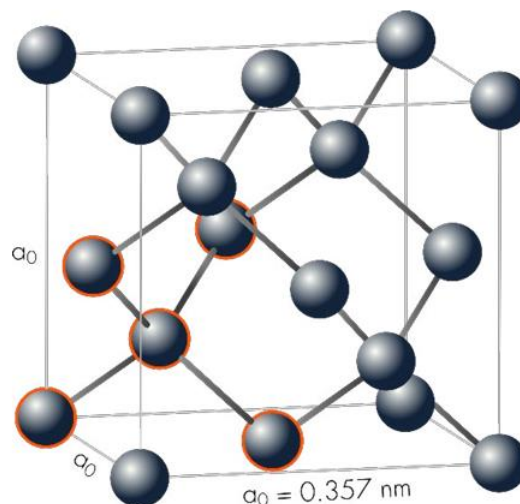


**Figure 2.1:** Crystal structure of diamond. [35]

Diamond has a very large bandgap:  $5.47 \text{ eV}$  [36], the highest among the semiconductors. It is

due to the high bandgap and high electrical resistivity that diamond is sometimes regarded as an insulator. In further discussion we will compare some of the properties of diamond and silicon. We chose silicon as a referent material since most of the semiconductor detectors, and semiconductor devices overall, are made of silicon. Table 2.1 shows basic properties of silicon and diamond.

**Table 2.1:** Basic properties of diamond and silicon [36]–[39].

	<b>Diamond</b>	<b>Silicon</b>
<b>Lattice constant [nm]</b>	0.357	0.543
<b>Electrical resistivity [<math>\Omega</math> m]</b>	$>10^{11}$	$2.3 \times 10^3$
<b>Relative permittivity</b>	5.7	11.9
<b>Breakdown field [MV/m]</b>	$10^6$	$3 \times 10^4$
<b>Bandgap [eV]</b>	5.47	1.12
<b>Electron-hole pair creation energy [eV]</b>	13	3.62
<b>Mobility electrons [<math>\text{cm}^2/\text{V s}</math>]</b>	1800	1450
<b>Mobility holes [<math>\text{cm}^2/\text{V s}</math>]</b>	1600	505

Even though the crystal lattice structure of both diamond and silicon is the same, diamond has a smaller lattice constant, which means that the atoms are more tightly packed. This is due to the strong carbon-carbon bonds in diamond which is the main reason for its exceptional hardness. Another similarity between diamond and silicon is that both materials are indirect bandgap semiconductors, meaning that the minimum of the conduction band and the maximum of the valence band have different k-vectors. For indirect semiconductors the transition of electron from the valence to the conduction band cannot be accomplished by photon absorption alone. For this reason, the energy needed to create one electron-hole pair (EHP) for indirect semiconductors is always larger than the bandgap. Diamond has both larger bandgap and EHP creation energy than silicon. Consequently, an impinging particle would create four times more EHP in silicon than in diamond. Therefore, a diamond detector would intrinsically have lower signal and worse energy resolution than a silicon detector, since the statistical fluctuation in the number of created EHP corresponds to detected energy uncertainty. On the other hand, high bandgap means lower thermal noise due to the lower chance of thermal excitation of charge carriers. Unlike silicon detectors, diamond detectors don't need cooling since the thermal noise is very low even at room temperature. Moreover, it was shown that diamond detectors can

function even at high temperatures ( $>700$  K [37]), a unique property of diamond. The ability to function at high temperatures combined with good radiation tolerance [37]–[39] make diamond an ideal material for detectors operating in harsh environments. Relative permittivity (dielectric constant) of diamond is around two times lower compared to silicon, making diamond a suitable material for low capacitance devices. Another advantage of diamond over silicon is significantly higher breakdown field and hole mobility. In fact, the mobilities of electrons and holes in diamond have similar value, whereas in silicon electrons have three times higher mobility than holes. Therefore, most silicon detectors are designed for electron collection whereas diamond detectors can be used both for electron and hole collection. Due to high mobility of both electrons and holes and high breakdown field, signals in diamond detectors are very fast. Therefore, diamond detectors are often used for timing purposes [40]–[42].

## 2.2 Defects in diamond

Defects are defined as any imperfections in the crystal structure. Defects create energy levels in the energy gap that can trap free charge carriers. Depending on the defect concentration, trapping of the free charge carriers can be significant and lower the output signal. Detrapping process also, can cause the fluctuation of the detector output signal which lowers the energy resolution of the system. There are different types of defects based on the defect geometry. Planar defects, grain boundaries or stacking faults, are present at the interface between two monocrystal parts of a polycrystalline diamond. Planar defects have a significant effect on the charge transport in a detector. Therefore, polycrystalline diamonds are rarely used for high performance diamond detectors. Linear defects can be created by dislocation propagation during the growth of the crystal. Even though linear defects don't have so severe effects on the detector performance, they can cause a local space charge buildup limiting detector functionality. With longer crystal growth times linear dislocations disappear from the crystal structure. Point defects are zero dimensional faults in the crystal. There are different types of point defect, shown in fig. 2.2. Interstitial defects are atoms (noncarbon or carbon) located in the space between the lattice atoms. Substitutions are noncarbon atoms that have replaced carbon atoms in the crystal lattice. Vacancies are defined as empty sites within the crystal lattice where a carbon atom should be, basically a missing carbon atom. Diamonds grown for particle detectors are usually made to be as pure as possible. High grade diamond crystals are always monocrystalline without planar and linear dislocations, with very low concentration of point defects. The purest crystals are labeled as single crystal (SC) electronic grade (EL) and contain

## Diamond as a detector material

< 1 ppb of nitrogen, which is the most common impurity in diamond. Unfortunately, the existence of point defects cannot be avoided even in the best quality diamond crystals. While all defects disrupt the crystal structure, not all defects are unwanted. Quantum centers in diamond are intentionally created point defects. Concentration of point defects can affect properties of diamond such as color, carrier mobilities, radiation hardness, etc. Therefore, grading diamond crystals for research purposes is based on the concentration of impurities i.e., noncarbon atoms within the crystal.

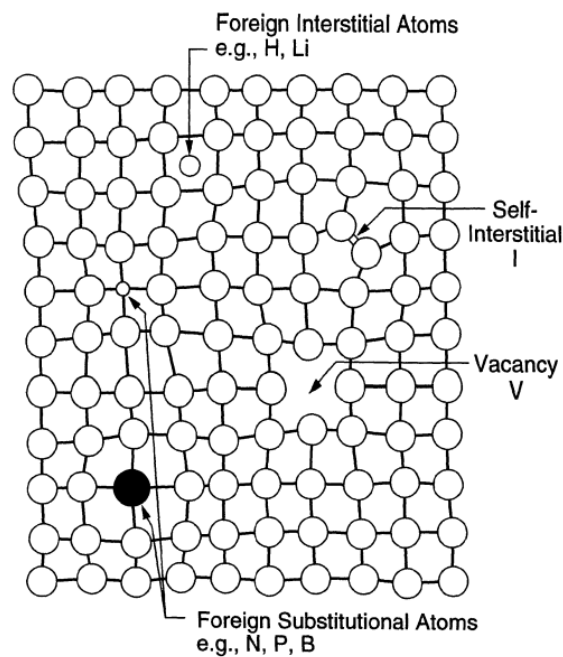


**Figure 2.2:** Point defects in diamond. [43, p. 193]

Fabrication of defects in diamond can be done by irradiation or ion implantation. Energetic neutrons, gamma rays, electrons or ions can displace carbon atoms from their lattice sites, thus creating interstitials and vacancies. In this work, we define ion irradiation as the process in which the impinging ions pass through the crystal losing a portion of their energy to the crystal, whereas ion implantation is defined as the process in which the ions lose all their energy to diamond, effectively stopping in the crystal. While interstitials created by irradiation are always self-interstitials, ion implantation creates foreign interstitials, as well. For successful quantum center fabrication, it is necessary to activate the defects after the irradiation/implantation, so quantum centers can be formed. Defect activation is achieved by annealing the samples at high temperatures [44]. High temperature makes vacancies mobile so they can diffuse in the diamond

crystal. This especially is important for quantum centers based on a vacancy combining with a foreign substitutional atom [45] such as the case in NV center formation, where two carbon atoms are dislocated from the crystal lattice, one is replaced by a nitrogen ion and the other site is vacant. In NV center production, two defects need to be very close to form a quantum center and mobile vacancies increase that chance significantly. In some cases, however, high vacancy mobility would result in lower vacancy concentration since some of the vacancies would recombine with the interstitial atoms. This process lowers the chance of quantum center fabrication, so lower annealing temperatures are sometimes preferred [46]. It should be noted that defect fabrication is a process that causes damage to the crystal structure, altering its characteristics, sometimes even causing amorphization. By using focused ion beams ion irradiation/implantation process can be localized, limiting the damage to only one part of the crystal. The damaging nature of the ions can sometimes, however, be very useful. For example, focused ion beam can be used for amorphization of diamond in a very controlled manner, creating buried graphitic electrodes [47], [48]. Also, ion beam implantation can be used for doping of diamond [49], [50].

### **2.3 Surface properties of diamond**

Diamond surface is the interface between the crystal and the surroundings. Due to the hybridization of carbon atoms in diamond crystal the crystal surface cannot exist as a truncated bulk lattice, because of the high surface energy caused by unsaturated covalent bonds. This is shown in fig 2.3 a) [51], for (100) plane. Therefore, the structure of diamond surface differs from the bulk. The surface atoms are bonded so the unsaturated bonds are removed, creating a stable surface structure. Figure 2.3 b) shows diamond surface structure for (100) plane. Characteristics of a material are determined by the atomic and electronic structure, but they are also sensitive to the impurities, surface, and interface structure. Due to its structure, diamond surface is prone to impurities, mainly hydrogen and oxygen. The influence of these impurities is noticeable in the Schottky barrier formation mechanisms in diamond [52] and also in the negative electron affinity [53] of diamond surface. The electron affinity is the energy difference between the minimum of the conduction band and the minimum free electron level in vacuum. In other words, electron affinity is the energy needed for an electron from the conduction band of a crystal to be released into vacuum. Negative electron affinity means that conductive electrons close to the diamond surface would spontaneously leave the crystal. As we will show

in chapter 4, this mechanism has measurable influence on the transport properties of diamond close to the surface.

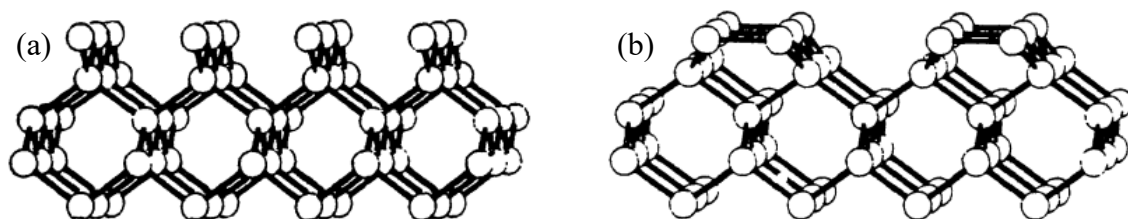


**Figure 2.3:** (a) Truncated diamond surface for (100) direction with dangling bonds. (b) Stable surface structure for (100) direction. [51]

## 2.4 Production of diamond

In nature diamond is created under very high pressure and temperature, deep below the Earth's surface [54]. Natural diamond is most often polycrystalline and is not used for detector fabrication because of too high impurity concentration. The quality of diamond crystals is determined by their impurity content. Diamonds of type Ia (most of the natural diamonds) have up to 3000 ppm of nitrogen. Type IIa diamonds have considerably less nitrogen, whereas type IIb has Boron impurities. Artificially grown, high quality single crystal diamonds can be of optical grade or electronic grade with the latter being the highest quality diamond currently available (with as low as 1 ppb of impurities). Production of industrial diamonds can be done by mimicking the conditions under which natural diamonds are formed, using a HPHT (high pressure high temperature) process. HPHT process can produce both polycrystalline and monocrystalline samples with size suitable for detector fabrication [55]. However, the concentration of impurities (usually nitrogen) within the HPHT diamond crystals is too high for applications that require low noise and high energy resolution.

Another method for fabrication of diamond crystals is CVD (chemical vapor deposition) process for epitaxial growth of diamond. During this process a mixture of hydrogen ( $H_2$ ) and methane ( $CH_4$ ) gas is introduced into the CVD reactor. Illustration of a CVD reactor is shown in fig 2.4 a). The gas mixture is activated, creating plasma, usually by microwaves, but RF (radio frequency) field, lasers, hot filament, or chemical reactions could also be used. For a microwave activated plasma the reactor vessel is designed to act as a microwave resonator sustaining plasma a few centimeters above the substrate. High plasma temperature (up to 3000 K) leads to thermal dissociation of hydrogen, which enables transfer of carbon from the

## Diamond as a detector material

plasma to the substrate. The substrate is cooled, creating a temperature gradient which causes material transfer from plasma. For diamond production the surface of the substrate should be between 800 K and 1100 K. At those temperatures nucleation of carbon into diamond is dominant to the graphite production.

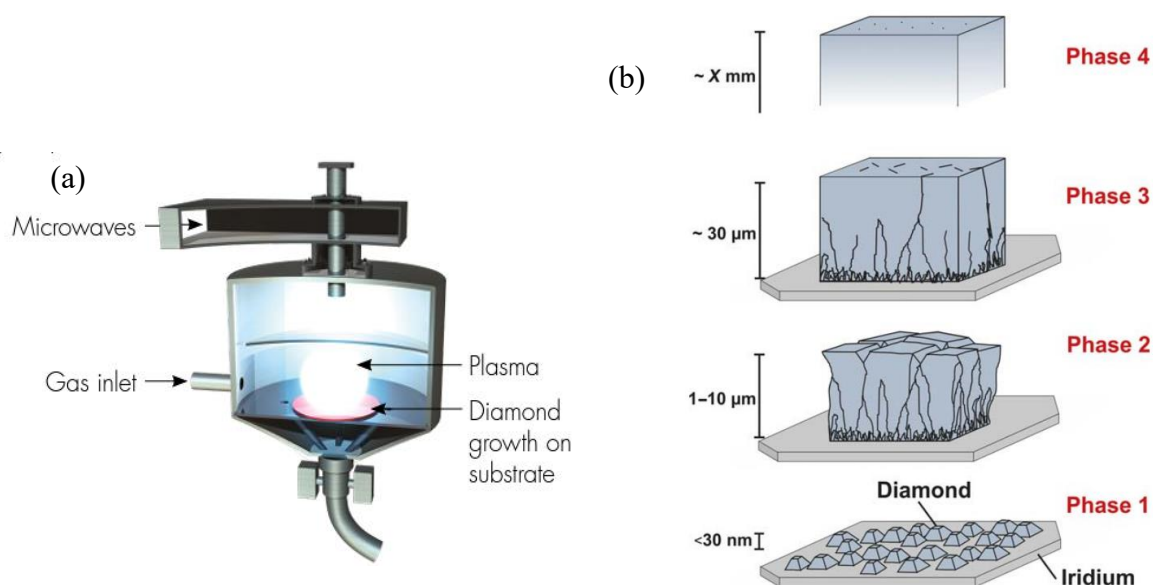


**Figure 2.4:** (a) Illustration of a CVD reactor for diamond growth. [56] (b) Stable surface structure for (100) direction. [57, p. 71]

The substrate for CVD diamond production is usually a HPHT diamond crystal, but other materials, such as iridium [58], [59] can be used, as well. The nucleation of carbon happens on the whole surface of the substrate, forming diamond “islands”. As the islands grow and start to cover the full area of the substrate, creating a diamond film, grain boundaries form at the points of contact between different islands. The structure of the diamond film at this point is polycrystalline. As the distance of the growth surface from the substrate increases the dislocations (grain boundaries) become fewer in number, creating larger volumes of monocrystalline diamond, as shown in fig 2.4 b). After a certain growth thickness there are no more grain boundaries – monocrystalline diamond layer is formed. The monocrystalline part can be subsequently cut from the rest of the crystal to create a single-crystal (sc) diamond sample. Homoepitaxial growth, i.e. growth of diamond on a diamond substrate, produces the highest quality results, especially when grown on a single-crystal substrate (highest quality single crystal diamonds are grown this way).

## 3 Signal generation and processing

In semiconductor radiation detectors, interaction of radiation (photons or energetic ions) with the sensitive volume of the detector, results in creation of free charge carriers – electron-hole pairs. The sensitive volume of the detector is the part of the semiconductor material with non-zero electric field across it, which is created by applying voltage on the detector electrodes. Under the influence of the electric field, the free charge carriers move toward the electrodes. Electrons move toward the positively charged anode, and holes toward the negative cathode. Depending on the detector design there can be more than one anode and/or cathode. The drift of charge carriers induces an electric pulse on the electrodes, which can be then read out (measured) and processed by a readout and processing electronic systems, respectively [60, p. 2].

### 3.1 Interaction of ionizing radiation with diamond

As ionizing radiation (energetic ions, photons, alpha particles, etc.) travels through the detector material, it loses its energy in interaction with atomic electrons and nuclei. Even though the mechanism of interaction is not the same for all types of ionizing radiation (interaction of energetic ions with semiconductors differs from the interaction of gamma rays) the result is always EHP generation. Here we assume that the impinging particle is energetic enough, i.e., its energy is higher than the energy needed for EHP creation. The creation of EHP happens when an electron from the valence band gains enough energy, from the interaction with the impinging particle, to become excited into the conduction band. At its place in the valence band there is an empty space left – a hole. For direct bandgap semiconductors (such as gallium arsenide, cadmium tellurite, etc.) the excitation of electron can take place solely due to the interaction with the impinging particle. For indirect bandgap semiconductors however, electron



excitation is only possible with interaction of both the impinging particle and the crystal lattice (phonons). Diamond, silicon, and germanium (among others) are indirect bandgap semiconductors. The energy needed to create one EHP (shown in table 2.1. for diamond and silicon) is equal to the bandgap for direct semiconductors while for indirect semiconductors it is always greater than bandgap. In this work we used energetic ions and gamma rays for EHP creation in diamond crystal. The energy loss of charged particles in a material (stopping power) is given by Bethe formula [61]:

$$-\frac{dE}{dx} = KZ^2 \frac{Z}{A} \left[ \frac{1}{2} \ln \left( \frac{2m_e c^2 \beta^2 \gamma^2 T_{max}}{I^2} \right) - \beta^2 - \frac{\delta}{2} \right] \quad (3.1)$$

Here  $K = 4\pi N_A r_e^2 m_e c^2$ , where  $r_e$  is classical electron radius and  $m_e$  is electron mass,  $N_A$  is Avogadro's constant,  $z$  is the charge of the impinging particle, and  $Z/A$  is the ratio of atomic and mass numbers of the material.  $\beta = v/c$ , and  $\gamma = 1/\sqrt{1 - \beta^2}$  are relativistic factors dependent on the velocity of the impinging particle  $v$ . The average electron excitation energy  $I$  can be approximated by  $I \approx 10Z \text{ eV}$  [62, p. 6]. Density correction  $\delta$  becomes important at relativistic energies of the impinging particle and it limits the stopping power of the material. For low impinging particle velocities  $\beta \ll 1$  and  $\gamma \approx 1$  therefore, the stopping power is proportional to  $1/\beta^2$ . This means that the stopping power increases as the velocity of the impinging particles decreases. On the other hand, at relativistic velocities the stopping power is proportional to  $\ln(\beta\gamma)$ , which increases with the velocity of the impinging particle. Unfortunately, Bethe formula can correctly predict energy loss only if the energy of the impinging particle is high enough so that the inner shell electrons can be considered static. Also, at very high energies corrections are added to the formula so it describes the energy loss of the impinging particle correctly [63]. The equation 3.1 describes energy loss due to the electromagnetic interaction of the energetic charged particles with the orbital electrons – electronic energy loss. Electronic energy loss is dominant interaction process at high energies ( $>1 \text{ MeV}$ ), whereas at low energies ( $<10 \text{ keV}$ ) nuclear energy loss is dominant. Nuclear energy loss is a process when an impinging particle transfers significant energy to the atomic nuclei of the substrate, resulting in atoms being displaced from their position in the crystal lattice. A single impinging particle can displace multiple atoms along its path.

For energetic ions the energy loss reaches its maximum at the end of the range. The electronic loss at that stage is the highest and so is the ionization of the material. Figure 3.1 shows stopping power of 1 MeV protons in diamond simulated by SRIM software [64]. The characteristic curve

is called Bragg curve, and the peak is called Bragg peak. Bragg peak represents maximum stopping power of a material for a specific ion species and energy.

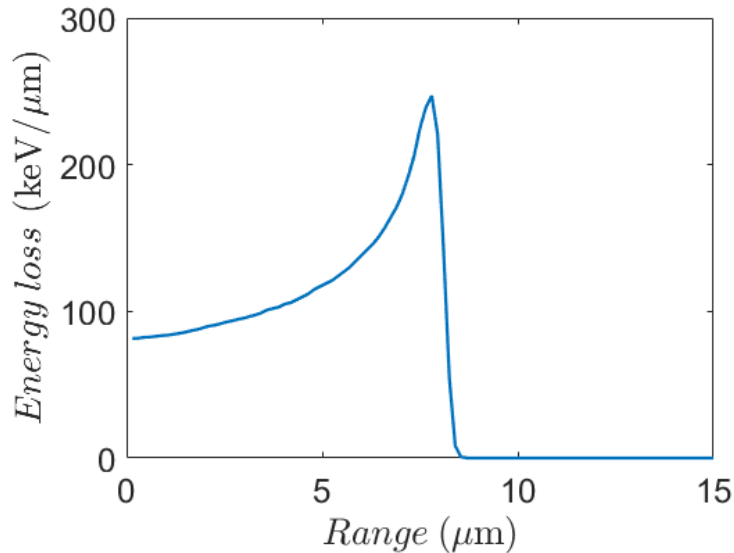


**Figure 3.1:** SRIM simulation of energy loss of 1 MeV protons in diamond.

For photon energies between 10 eV and 10 MeV, which includes x- and gamma-rays, only the photoelectric effect, pair production and Compton scattering mechanisms of interaction with semiconductor material are significant. Of these three, pair production is important only for high-energy photons. Compton scattering predominates at intermediate energies. And photoelectric effect is dominant at lower energies [65, p. 40]. Gamma-ray photons emitted in nuclear transition are usually energetic, with energies greater than a few tens of keV [66, p. 136]. However, their energy can be of the same order as x-rays. An example is  $^{241}\text{Am}$ , whose spectrum has two gamma lines, at 26.3keV and 59.5keV [67] which is low enough to overlap with x-ray spectrum of some elements such as antimony. Therefore, the fundamental difference between x- and gamma-rays is not in their energy (although gamma-rays are usually more energetic) but in their origin. Gamma-rays are emitted from the atomic nuclei when nuclear energy transitions occur, while x-rays are emitted in atomic electrons' transitions [68, p. 61]. Compton scattering is the effect when a photon scatters from an atomic electron resulting in a photon of lower energy (compared to the energy of incident photon) and an electron recoiling with an amount of energy which depends on the scattering angle. In pair production process, the entire incident photon energy is converted into the creation of an electron-positron pair. The pair production requires the presence of a heavy body (atomic nucleus) in order for both energy

and momentum to be conserved. Positron is anti-electron and, after it slows down and almost comes to rest, it will be attracted to an electron and annihilated. In the annihilation process the electron and positron rest masses are converted into two gamma-rays, each with energy of 0.511 MeV. These annihilation gamma rays are emitted in opposite directions in order to conserve momentum and they may in turn interact in the absorbing medium by either photoelectric absorption or Compton scattering [66, p. 141]. The photoelectric effect is, by far, the main interaction mechanism of x-ray photons in semiconductor detectors. The photon energies are usually 100 eV to ~30 keV. Photoelectric effect is a phenomenon where the incident photon is completely absorbed by the material and its energy transferred to an atomic electron called the photoelectron [68, p. 41,42]. The energy of the photoelectron, in comparison to the incident photon, will differ by the binding energy of the atomic electron. The loss of the atomic electron creates a vacancy in the inner atomic shell [65, p. 44] which is subsequently filled by an electron from a higher energy level resulting in an x-ray emission.

### 3.2 Signal generation in diamond

As an energetic ion or gamma photon moves through the detector, it creates EHP along its trajectory. Due to the electric field present in the active volume of the detector, free charge carriers drift towards the electrodes, as shown in fig 3.2, inducing electric signal. Electric pulse induced on the electrodes is a brief surge of current or voltage. The pulse characteristics such as shape, rise and fall time, and amplitude carry information about the type and energy of detected radiation, drift velocity of the free charge carriers and other. The signal induced on the electrodes by drift of the electrons and holes can be calculated by the theory proposed by W. Shockley [69] and S. Ramo [70] called Shockley-Ramo theorem. It states that a moving charge  $q$  will induce current  $i$  on an electrode  $a$ , defined by the equation 3.2.

$$i = -q\vec{v} \cdot \vec{E}_a(x) \quad (3.2)$$

where  $\vec{v}$  is drift velocity of the moving charge and  $\vec{E}_a$  is called the weighting field. The total charge induced on the electrode by the drift of the charge  $q$  from location  $x_i$  to location  $x_f$  is given by equation 3.3:

$$Q = -q [\varphi_a(x_f) - \varphi_a(x_i)] \quad (3.3)$$

where  $\varphi_a$  is called the weighting potential. The weighting field and weighting potential are defined as the electric field and potential that would exist at any position  $x$  of the charge  $q$  if the electrode  $a$  was set to unit potential and all other electrodes were at potential zero [60, p. 7]. Shockley-Ramo theorem is a powerful tool in analysis of the charge transport in semiconductor detectors. More detailed analysis and the proof of the Shockley–Ramo theorem can be found in [71]–[73].

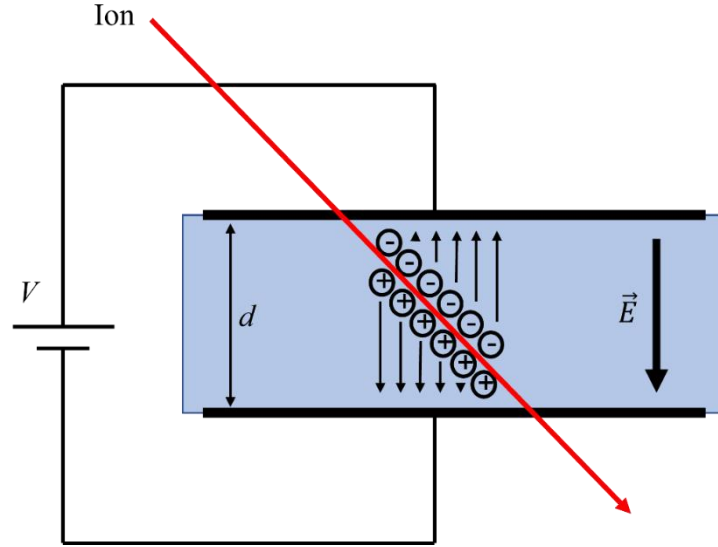


**Figure 3.2:** EHP creation by an energetic ion as it transverse diamond detector.

We will show how the induced charge can be calculated for a planar detector, the simplest form of a semiconductor detector. Therefore, the calculation using Shockley-Ramo theorem can be done analytically, unlike for some other, more complex detector geometries. The planar detector consists of a crystal sandwiched between two electrodes, as shown in fig. 3.2. We will assume that the electric field inside the detector is uniform. This assumption is valid for most planar diamond detectors and for the active volume of planar silicon detectors. In the following analysis we will approximate that the relation of the drift velocities and the applied electric field is linear, which is valid for moderate electric fields. As the free charge carriers (electrons and holes) drift toward the electrodes they induce a current on the electrodes given by Shockley-Ramo theorem as:

$$i(t) = \frac{e}{d} [v_e(t)n_e(t) + v_h(t)n_h(t)] \quad (3.4)$$

## Signal generation and processing

where  $e$  is the electron charge,  $d$  is the detector thickness and  $v_e$  ( $v_h$ ) and  $n_e$  ( $n_h$ ) are the drift velocity and concentration of electrons (holes), respectively. The concentration of electrons and holes can be written as:

$$n_e(t) = n_0 e^{\frac{-t}{\tau_e}} \text{ and } n_h(t) = n_0 e^{\frac{-t}{\tau_h}} \quad (3.5)$$

where  $n_0$  is the initial number of EHP and  $\tau_e$  ( $\tau_h$ ) it the electrons (holes) lifetime. By substituting expressions for electron and hole concentrations from equation 3.5 to equation 3.4 and integrating over electron and hole transit times, defined as:

$$T_e = \frac{d-x_0}{v_e} \text{ and } T_h = \frac{x_0}{v_h} \quad (3.6)$$

where  $x_0$  represents the point of interaction of either energetic ion or gamma ray with the detector material, and  $d$  is the detection thickness, we get:

$$Q = n_0 e \left\{ \frac{v_e \tau_e}{d} \left( 1 - e^{\left( \frac{x_0 - d}{v_e \tau_e} \right)} \right) + \frac{v_h \tau_h}{d} \left( 1 - e^{\left( \frac{-x_0}{v_h \tau_h} \right)} \right) \right\} \quad (3.7)$$

Equation 3.7 is called Hecht equation and describes how charge transport parameters influence the total charge induced on the electrodes. The induced charge is often referred to as collected charge. From equation 3.7 we can see that if there is a significant difference in drift velocities of electrons and holes the charge collection time will strongly depend on the location of interaction of the impinging particle. For diamond detector the mobility of electrons is around 1.7 times the mobility of holes (the ratio of the saturation drift velocities is the same), therefore the location dependency of the charge collection time in pristine diamond is not so strong [74, p. 70]. In the ideal crystal the total induced charge will be the same as the charge created by the impinging particle. However, recombination of EHP and impurities acting as charge traps (chapter 2.2), decrease the induced (detected) charge so it is always smaller than the created charge. If the impurity concentration is small and the electric field across the detector is high, the difference in created and detected charge is negligible. In that case the detector has 100 % charge collection efficiency (CCE). CCE is defined as the ratio of detected and created charge and is expressed in percentages. It is proportional to charge carrier mobility thus proportional to the electric field if the electric field is lower than the saturation field of the material. CCE is also sensitive to trapping effect. Trapping and recombination effects can significantly influence detector operation by decreasing the amount of free charge carriers. Depending on their type,

traps can interact with both electrons and holes, or only with one charge carrier type making the trapping effect asymmetrical. Trapping and recombination processes are described by Shockley-Reed-Hall recombination [75], also called trap-assisted recombination. Here we can distinguish four mechanisms, shown in fig 3.3 a)-d), respectively: capture of electron from the conduction band; emission of electron to the conduction band (electron detrapping); emission of hole to the valence band (hole detrapping); trapping of hole from the valence band. There are also two more trap-assisted processes. Trap-assisted recombination of electron and hole: when an electron deexcites from the conduction band to the trap level and subsequently to the valence band (combination of electron capture followed by a hole capture on a single trap level). Trap-assisted emission of electron and hole: when an electron is excited from a valence band to the trap level, and subsequently to the conduction band (combination of hole detrapping followed by electron detrapping on the same trap level).

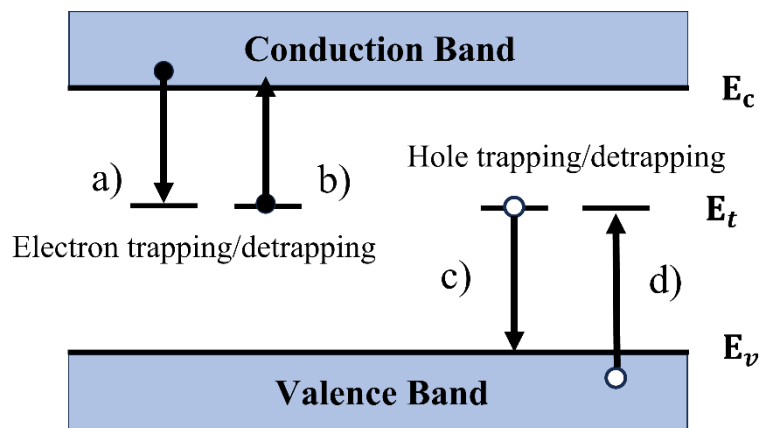


**Figure 3.3:** Mechanisms of trap interaction with electrons and holes. (a) Trapping of electron from the conduction band. (b) Electron emission (detrapping) to the conduction band. (c) Hole emission (detrapping) to the valence band. (d) Trapping of hole from the valence band.  $E_c$ ,  $E_v$  and  $E_t$  are minimum of conduction band, valence band and trap energy level, respectively.

When an electron or hole is trapped, it is temporarily bound to that specific position in a crystal, creating what is called a space charge. If the impurities are localized in the crystal and their concentration is high enough, space charge buildup can occur. In that case the electric field originating from the space charge can locally mask the external electric field degrading detector performance. This effect is called polarization. In extreme cases, polarization can cause total failure of the detector. Polarization can happen due to the impurities naturally present in the detector material (both bulk and surface defects can cause polarization), but it can also be a result of the damage created by radiation. The latter is the main cause of detector degradation

over time. Mild polarization can be reversed by illuminating the crystal, since light can cause release of the trapped charge, or reversing detector's biasing voltage, causing gradual detrapping which eventually results in neutralization of the space charge and restores normal detector operation. Severe polarization however, especially when caused by radiation damage can only be reversed by thermal annealing.

### 3.3 Noise in detectors

Electronic noise is a phenomenon that manifests as random fluctuations of current or voltage signals. Noise is a consequence of fundamental natural processes and therefore can't be fully separated (filtered) from a signal. In other words, there is no noiseless signal. Since electronic noise essentially represents randomness in some physical property of the devices used for signal generation, transport, or processing, we can distinguish different types of noise.

In any resistive material there will be some fluctuations in the velocity of charge carriers due to their thermal motion. These velocity fluctuations would cause fluctuations in voltage measured across the terminals, or across any two points of the conducting material. Even with no externally applied voltage across the conducting material the measured voltage would fluctuate around zero. This fluctuation in voltage is called thermal or Johnson noise. In case of a resistor spectral voltage density of thermal noise is given by:

$$e_n^2 = 4kTR \quad (3.8)$$

Where  $T$  is temperature in Kelvin,  $R$  is resistance and  $k$  is the Boltzmann constant. As can be seen, higher resistivity means higher voltage noise. Thermal noise does not exhibit a frequency dependence and therefore, it's referred to as white noise. In other words, the spectral power density of thermal noise is constant. That means that the power of thermal noise would increase as the measurement bandwidth increases.

The second type of noise is generated by individual injection of charge carriers. This is present in semiconductor devices, for example, where the electrical current is directly proportional to the number of discrete charge carriers. Therefore, fluctuations in the rate of charge carrier generation or injection would cause a current fluctuation, as well. This fluctuation is called shot noise, and its spectral current density is given by:

$$i_n^2 = 2eI \quad (3.9)$$

Where  $e$  is electron charge, and  $I$  is the mean current. Same as thermal noise, shot noise does not show any frequency dependence and is referred to as a white noise.

As was mentioned in section 2.2, in semiconductor material free charge carriers can be trapped by defects in the crystal, which decreases the measured signal. Trapped carriers could later be released and increase the signal amplitude. The time between the trapping and releasing the free charge carriers (trapping time) is specific to the type of defects and the semiconductor itself. For higher frequency signals, where the propagation time is much shorter than the trapping time the contribution of those fluctuations in the total signal would be far less significant compared to the lower frequency signals where the propagation time is of the same order of magnitude or higher than the trapping time. Therefore, the signal fluctuations caused by this phenomenon are frequency dependent. Spectral voltage density of this type of noise is:

$$e_n^2 = \frac{A_f}{f} \quad (3.10)$$

Where  $f$  is the frequency and  $A_f$  is a constant (equal to the spectral voltage density at 1 Hz). This type of signal fluctuation is called flicker noise or 1/f noise, low-frequency noise, excess noise, or pink noise, due to its frequency dependence. Flicker noise is characteristic for semiconductor devices, but it is present in other types of devices, as well (vacuum tubes, resistors...).

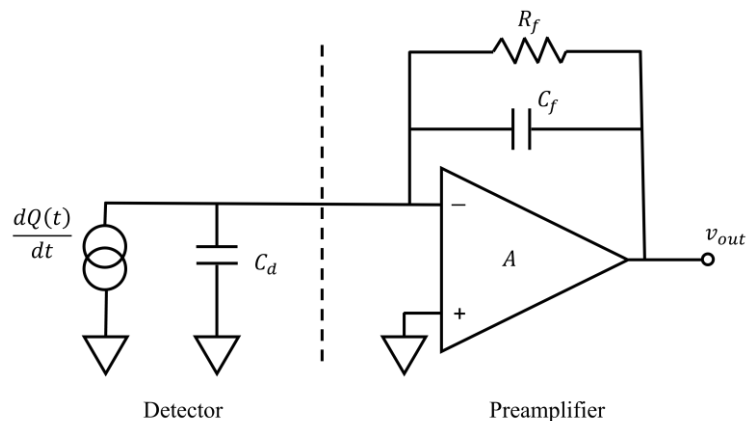
### 3.4 Processing of detector signal

The signals induced by the moving free charge on the detector electrodes are, in general, very small. For example, the signal generated by a 100 keV proton in a diamond detector with 1 pF electrode capacitance will be around 1.2 mV. Therefore, before any further processing the signal from the detector should be amplified. This is the primary function of a preamplifier – to extract and amplify the output signal of the detector. It is very important that the amplification is performed with minimum signal degradation. Otherwise, the information contained in the signal, or a part of it, might be lost. The information of interest can be the amplitude and/or the shape of the pulse. The amplitude of the pulse is proportional to the energy of the impinging particle, whereas the pulse profile as well as the rise and the fall time are used for pulse-shape discrimination applications, timing, and defect characterization. There are two main classes of amplifiers used for primary amplification of semiconductor detectors' signals, depending on the application: current-sensitive preamplifier and charge-sensitive preamplifier. Those



amplifiers are referred to as preamplifiers because they are used to amplify the raw signal from the detector and usually their output is connected to another amplifier, called shaping amplifier. Current-sensitive preamplifiers are used for measurements of high rates of particles [76], timing [77], pulse shape discrimination [78] and also for transient current technique [79], where high time resolution of the signal is required. The time constant of the current-sensitive preamplifier is small compared to the free charge carrier transition time in the detector. As a consequence, the output pulse of the current sensitive preamplifier is proportional to the instantaneous induced current in the detector. The other amplifier class used with the semiconductor detectors is charge-sensitive preamplifier, whose time constant is larger than the free carrier transition time which makes the amplitude of the output signal proportional to the energy deposited in the detector by an impinging particle. It is the most widely used type of preamplifier because it provides a fixed gain even if the detector capacitance is not constant. Moreover, the charge-sensitive preamplifiers provide good sensitivity and linearity, that are of critical importance for semiconductor detectors' applications. There are three basic elements of a charge sensitive preamplifier: an operational amplifier with open loop gain  $A$ , a feedback capacitor  $C_f$  connected between the output and the inverting input of the operational amplifier, and a reset mechanism. Simplified schematics of a charge sensitive preamplifier and its Miller equivalent circuit are shown in figure 3.4 a) and b), respectively. Here we represented preamplifier reset by a feedback resistor  $R_f$ .

(a)



(b)

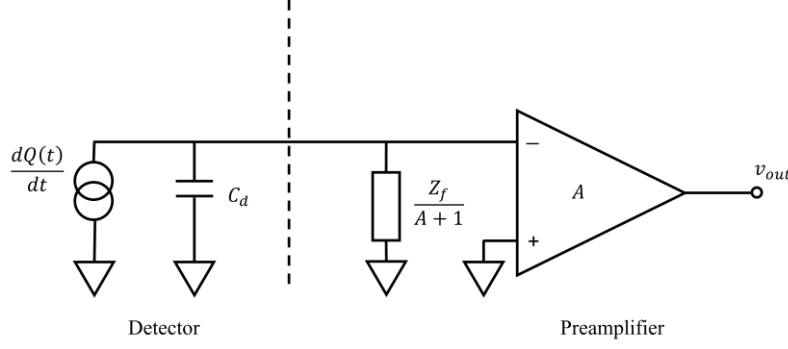


**Figure 3.4:** (a) Simplified schematics of charge-sensitive amplifier. (b) Miller equivalent circuit of a charge-sensitive amplifier from (a).

Very high input impedance of the operating amplifier causes most of the signal current from the detector, represented in figure 3.4 by an ideal current source and a capacitor  $C_d$ , to flow into the feedback capacitor. The detector current, integrated on the feedback capacitor would produce a voltage signal  $v_{out}$  at the output of the preamplifier. The detector signal can be written as:

$$\frac{dQ(t)}{dt} = i = \frac{v_{in} - v_{out}}{Z_f} = \frac{(A+1)}{Z_f} v_{in} = \frac{v_{in}}{Z_{eff}} \quad (3.11)$$

Where  $v_{in}$  is voltage at the inverting input of the operational amplifier and  $Z_f$  represents  $R_f$  and  $C_f$  in parallel. For large values of  $R_f$ ,  $Z_f \approx 1/C_f$ . The term  $Z_{eff}$  is effective impedance and as shown in figure 3.4 b), it is the impedance operational amplifier sees at the inverting port. At the same time  $v_{in}$  can be written as:

$$v_{in} = \frac{Q}{C_{tot}} = \frac{Q}{C_d + (1+A)C_f} \quad (3.12)$$

Here we used  $Z_{eff} \approx 1/C_{eff} = 1/((1+A)C_f)$ . Using the equation 3.12 and  $v_{out} = -Av_{in}$ , which relates the input and the output of the operational amplifier, we get:

$$v_{out} = -\frac{AQ}{C_d + (1+A)C_f} = -\frac{Q}{\frac{C_d}{A} + \frac{A+1}{A}C_f} \quad (3.13)$$

If the open loop gain of the operational amplifier is large (common values are  $>10^5$ ), the equation 3.13 becomes:

$$v_{out} \approx -\frac{Q}{C_f} \quad (3.14)$$

Therefore, the gain of the charge sensitive preamplifier depends only on the value of feedback resistor. From 3.13 we can see that it is very important for the operational amplifier to have a very large open loop gain to make the preamplifier output insensitive to the capacitance of the detector. In equation 3.12 we neglected the input capacitance of the operational amplifier and stray capacitances, which both increase the total capacitance present at the inverting input of the operational amplifier ( $C_{tot}$ ). The preamplifier output voltage depends, as we have seen, on the feedback capacitance, but also on the sensitivity of the detector material, since the total detector charge can be written as:

$$Q = \frac{E}{E_i} e \quad (3.15)$$

Where  $E$  is the energy of the impinging particle,  $E_i$  is energy needed to create one electron hole pair in the detector material and  $e$  is a unit charge, and hence 3.14 becomes:

$$v_{out} = -\frac{E}{E_i C_f} e \quad (3.16)$$

For example, a preamplifier with  $C_f = 0.1 \text{ pF}$  will give a 44 mV pulse per each 100 keV proton detected by a silicon detector, while the same preamplifier would only give a 12 mV pulse per a 100 keV proton, detected in diamond. That is because the energy needed to create one electron hole pair in diamond is higher than in silicon. In equation 3.16 we assume that all charge created in the detector will be converted to the output voltage pulse. However, that assumption is not true. We've already shown that some of the created free charge carriers will be trapped on the impurities that exist in the crystal. The remaining detector charge is never fully transferred to the feedback capacitor but shared between the feedback capacitance and all the other capacitances at the input of the preamplifier, including the detector capacitance, and stray capacitance. Detector capacitance here is defined as capacitance of the sensing electrode since that electrode is connected to the preamplifier therefore, that is the capacitance seen at the input of the preamplifier. The ratio of the charge transferred to the  $C_f$  and the total detector charge can be written as:

$$\frac{Q_f}{Q} = \frac{(A+1)C_f}{C_r + (A+1)C_f} = \frac{1}{\frac{C_r}{(A+1)C_f} + 1} \quad (3.17)$$

Where  $Q$  is the total detector charge,  $Q_f$  is the charge transferred to the feedback capacitance  $C_f$ , and  $C_r$  is the sum of all the other capacitances at the input of the operational amplifier. In

3.17 we used the Miller equivalent circuit of the charge sensitive preamplifier, fig. 3.3 b), hence the term  $(A + 1)C_f$ . From equation 3.17 we can see that in order to achieve high charge transfer efficiency between the detector and feedback capacitance, the detector capacitance needs to be small. Therefore, semiconductor detectors designed for low noise applications usually have a small sensing electrode. Also, stray capacitances should be as low as possible. In practice that is achieved by mounting the preamplifier as close as possible to the detector.

Without a proper reset mechanism, whose role is to discharge the feedback capacitor, successive input pulses would increase the output voltage of the preamplifier until it reaches saturation. At that point the output voltage of the preamplifier is at maximum value and the device can't process new events. The most common way to implement output resetting is to connect a large resistor (represented in figure 3.4 a) by  $R_f$ ) in parallel with the feedback capacitor. In that way  $C_f$  would continuously discharge on the  $R_f$ . The value of  $R_f$  should be chosen carefully depending on the specific application of the preamplifier. Very high resistivity in parallel with the  $C_f$  would result in lower thermal noise at the output but would also increase the  $RC$  constant of the preamplifier. In other words,  $C_f$  would discharge slowly which means that the rate of pulses the preamplifier can process would be lower. In that case there is a risk of pileup at the output of the preamplifier if the rate of particles impinging the detector is too high. Pileup happens when a pulse arrives at  $C_f$  before the capacitor has discharged sufficiently from the previous pulse. Therefore, the following processing stage will see the pileup event as a single pulse with amplitude higher than the original pulse. Figure 3.5 a) and b) show a signal profile at the output of the preamplifier for a single event and a pileup event, respectively. Too low value of  $R_f$ , while enabling detection of high rates of particles, will cause a higher thermal noise at the output of the preamplifier. Usually,  $R_f$  is in  $M\Omega$  to  $G\Omega$  ranges.

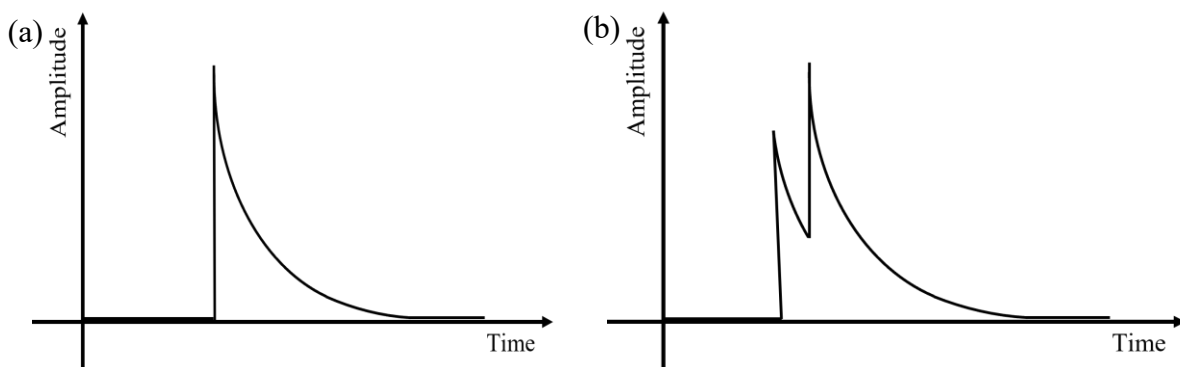


**Figure 3.5:** Signal profile at the output of the preamplifier (a) without and (b) with pileup.

Even though the use of a resistor as a feedback capacitor discharge mechanism is an effective and widely used method, in some cases it is not desirable to use a large resistance. The obvious one is when the preamplifier is realized as an integrated circuit [80] or fully integrated with the detector [81]. A resistor in the  $M\Omega$  range would occupy the largest portion of the chip space. Also, such a large resistor would necessarily add significant amount of stray capacitance at the input of the preamplifier resulting, as we will explain later, in larger overall noise. Therefore, in low noise applications as well as in fully integrated preamplifiers feedback capacitor is discharged by a reset transistor. A transistor placed in parallel to the feedback capacitor provides a fast discharge whenever the preamplifier output reaches a high enough value. When the reset transistor is operated in the cut off region it behaves as an open switch and the charge is integrated on the feedback capacitor. Once the output of the preamplifier reaches high enough value the reset circuit would put the reset transistor in the saturation region, and it will discharge the feedback capacitor. The shape of the output signal of a transistor-reset preamplifier (shown in figure 3.6) consists of series of small voltage increments (steps) followed by a sudden voltage drop caused by the reset transistor. The height of each step represents a detected event, and the amplitude of the step is proportional to the energy of the detected particle. Transistor reset mechanism is a very good solution for high-rate applications and can be easily realized either as a discrete or integrated component with small footprint. The drawback of the transistor reset is that the sudden drop in the output voltage of the preamplifier can saturate the following amplification stage. That is why transistor reset preamplifiers usually have an inhibit output signal which prevents the following stage from processing the output voltage drop but with the side effect of causing a certain dead time of the system.

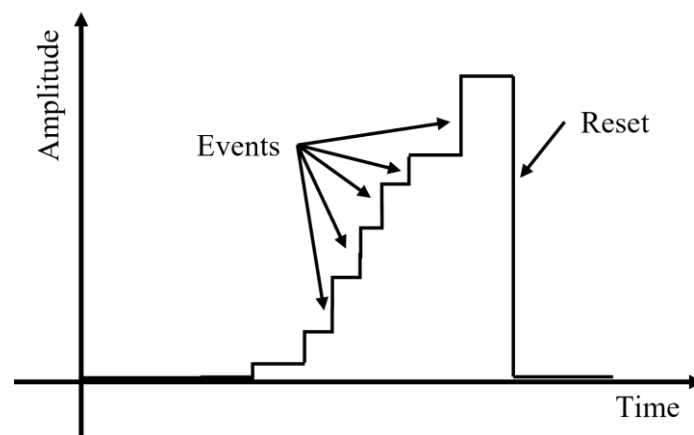


**Figure 3.6:** Output signal profile of a transistor-reset preamplifier.

So far, we have discussed the signal generation in the detector and the amplification of the signal by the preamplifier. In the models of detector and preamplifier we used, the leakage current through the detector was neglected. However, leakage current is always present, and depending on its magnitude sometimes it needs to be separated from the signal current. Otherwise, high leakage current can saturate or even damage the preamplifier. To separate the leakage current from the signal current we can put a capacitor, called coupling capacitor, between the detector and the preamplifier and apply high voltage across the detector through a load resistor. This approach, shown in figure 3.7 a), is referred to as AC coupling. The coupling capacitor prevents the detector leakage current from flowing into the preamplifier. To minimize the noise, load resistor should be very large. On the other hand, too high  $R_L$  would lower the voltage applied to the detector since the leakage current would cause significant voltage drop across the load resistor itself. Common values of  $R_L$  are from several hundreds of megaohms to few gigaohms. Addition of a capacitance between the detector and the preamplifier increases the total input capacitance seen by the operational amplifier, which also increases the noise. Therefore, AC coupling is rarely used for low noise applications.

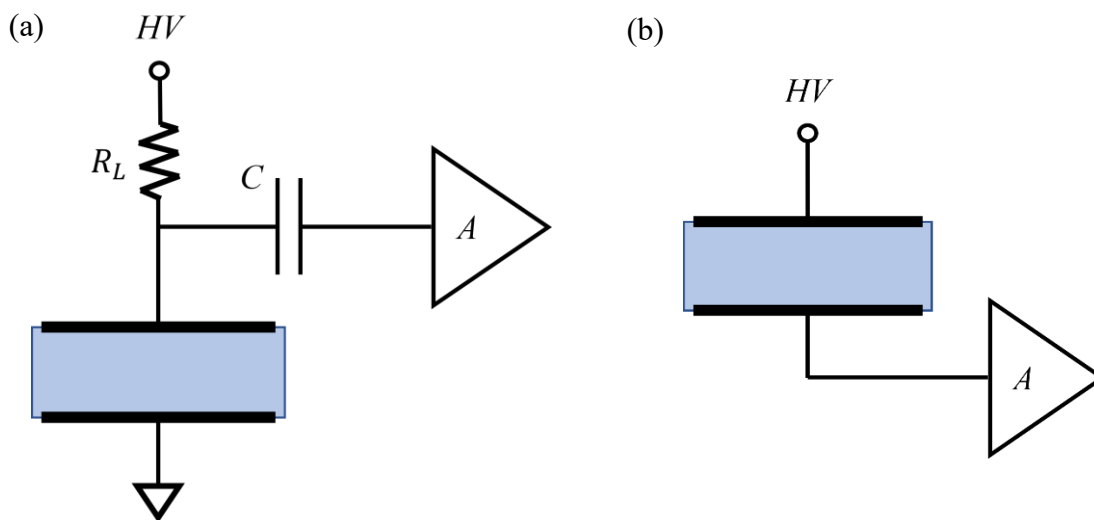


**Figure 3.7:** Simplified schematic of (a) AC and (b) DC detector/preamplifier coupling.

If the noise of the detector – preamplifier system should be as low as possible, and the leakage current of the detector is low then the detector can be connected directly to the input of the preamplifier. That configuration, shown in figure 3.7 b), is called DC coupling. For DC coupled detectors we can distinguish a sensing electrode, the electrode connected to the preamplifier, and at least one biasing electrode, the electrode connected to the biasing power supply. In this configuration there is no load resistor nor a coupling capacitor, which lowers the noise at the

most critical point of the system – input of the preamplifier. The stray capacitance is also lower for DC coupled detector since there are fewer connections between components. However, since neither electrode of a DC coupled detector is grounded, special care should be given to the carrier board design. In both AC and DC coupling configuration a low pass filter is added between the biasing power supply and the detector or load resistor to separate the biasing circuit noise from the detector/preamplifier system.

We have described the working principles of a charge sensitive preamplifier, which is the first element of a pulse processing system - several devices used to process the detector signal. The output of the preamplifier is usually fed into the shaping amplifier, also called linear amplifier, linear shaper, or spectroscopic amplifier. The main role of the shaping amplifier is to further amplify the signal so that the resulting signal's amplitude matches the input range of the following processing device, usually an ADC (analog to digital converter). For example, it is very inefficient to connect a signal whose amplitude is between 0 V and 1 V to the ADC whose input range is 0-10 V. The second role of the shaping amplifier is to perform optimization of signal to noise (S/N) ratio and reshape the signal to enable easier processing i.e., event detection. The shaping amplifier takes a preamplifier signal with a long decay time and reshapes it into a Gaussian (or semi-Gaussian) shape of significantly shorter decay time. The amplitude of a Gaussian shaped signal is digitized much more accurately compared to the signal from the preamplifier with exponential decay. A shaping amplifier typically consists of a differentiator followed by an integrator, with both having the same time constant. A simplified schematic of a shaping amplifier is shown in figure 3.8.

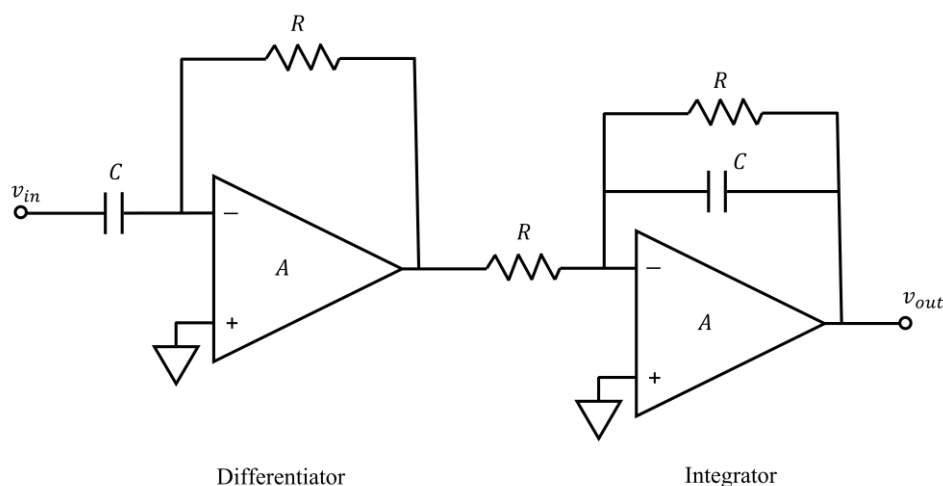


**Figure 3.8:** Simplified schematics of a shaping amplifier (CR-RC shaper).

The differentiator acts as a high-pass filter, while the integrator is a low-pass filter, making a shaping amplifier essentially a band-pass filter. By allowing only an interval of frequencies to

pass through, while filtering the rest, the shaping amplifier reduces the total noise in the output signal. Differentiation of the long-tailed signal from the resistor-reset charge sensitive preamplifiers produces an undershoot in the output signal of the shaping amplifier. For higher counting rates the subsequent pulse would be shifted by the undershoot of the previous pulse. That shift would cause inaccurate amplitude digitization causing degradation of the energy resolution of the system. To compensate the long tail of the preamplifier signal (a “pole”) defined by the preamplifier’s time constant  $\tau_1 = R_f C_f$ , a compensation circuit (called pole-zero compensation or pole-zero cancellation circuit), consisting of a resistor and a capacitor in parallel, is placed at the input of the shaping amplifier introducing a “zero” of time constant  $\tau_2 = \tau_1$ . Figure 3.9 shows two consequent pulses without and with pole-zero compensation, respectively. It is noticeable that without pole-zero compensation amplitude digitization of the second pulse would result in smaller value compared to the amplitude digitization of the first pulse, even though both pulses have the same amplitude. Since different preamplifiers have different time constants, a pole-zero compensation circuit is usually realized with a variable resistance so its time constant can be adjusted to match the time constant of the preamplifier.

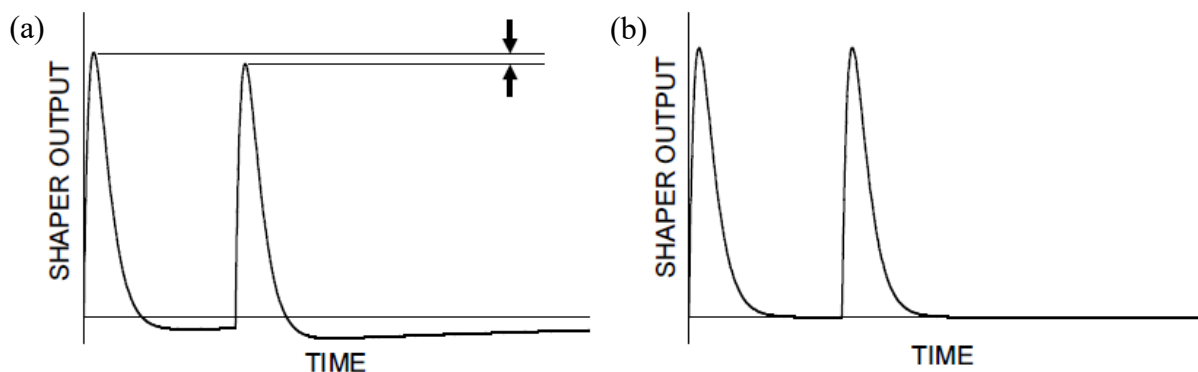


**Figure 3.9:** Profile of two subsequent pulses (a) without and (b) with pole-zero compensation circuit. [82, p. 178]

Besides pole-zero compensation circuit, other auxiliary circuits can be part of the shaping amplifier such as base line restorer, pileup rejector, and others, all aimed to mitigate the undesired effects of the signal processing. The main parameters of a shaping amplifier are gain and shaping time. The shaping time (also called peaking time), equal to the time constants of the differentiator and the integrator, defines the duration of the pulse at the output of the shaping amplifier. Increase of the shaping time increases the contribution from noise currents, whereas the decrease in shaping time results in an increase of voltage noise [82, p. 34]. Figure 3.10



shows the equivalent noise charge as a function of shaping time. There is a minimum of the total noise at the intersection point of current and voltage noise. Detector capacitance has a major influence on the noise figure in the way that higher detector capacitance would shift the voltage noise contribution and therefore the noise minimum to longer shaping times. Therefore, an optimal shaping time for a given detector depends on the detector capacitance. In most of the commercially available shaping amplifiers both the gain and the shaping time are variable so the same device can be used with detectors of different capacitances, and the amplitude of the output signal would match the input range of different pulse processing systems.

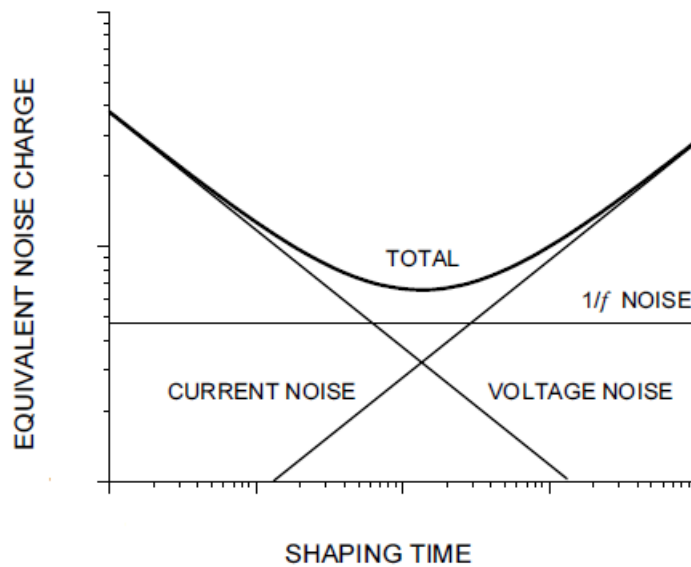


**Figure 3.10:** Noise as a function of the shaping time. [82, p. 34]

The final step of analog pulse processing is digitization of the output signal of the shaping amplifier. The digitization is done by an ADC. Digitized signal would then be processed by an MCA (multichannel analyzer), a system that extracts the height (amplitude) of the pulses digitized by an ADC. The height of each detected pulse is saved in the memory of an MCA and can be subsequently displayed on the computer screen in form of a histogram – a plot showing number of pulses (counts) versus the pulse heights (amplitudes). As was already mentioned the amplitude of each pulse is proportional to the energy of the impinging ion. Therefore, the histogram represents distribution of the energy deposited in the detector by the ionizing radiation. The shape of the signal at different processing stages, from its creation in the detector to the final histogram is shown in figure 3.11 [83].

## Signal generation and processing

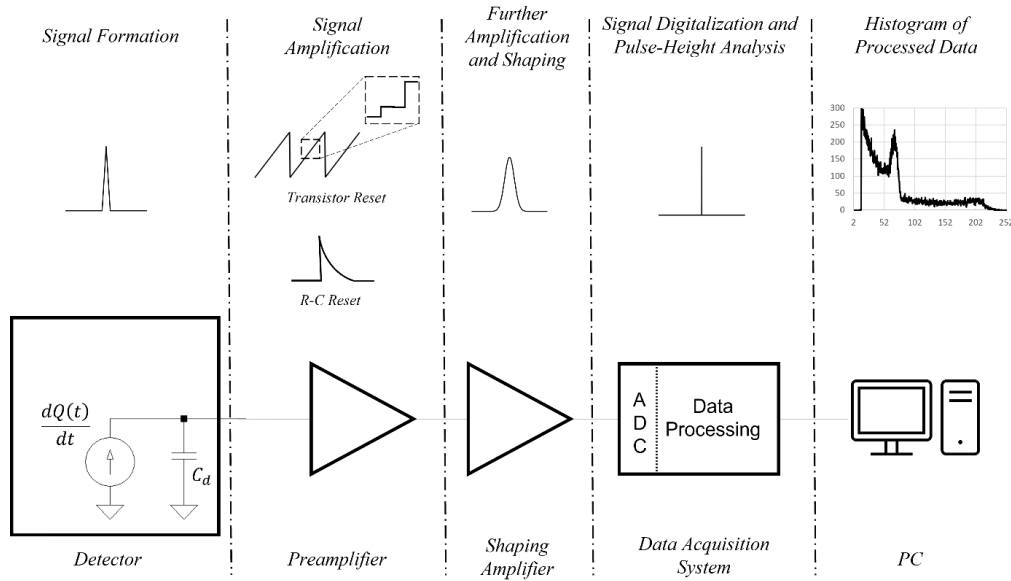


**Figure 3.11:** Shape profile of the signal at different processing stages, from the detector to digitized histogram. [83] IEEE 2022. ©

### 3.5 Noise in pulse processing systems

Every readout system consists of several devices (amplifiers, comparators, ADCs...) and each device is made up of components (resistors, capacitors, transistors...) all of which exhibit noise. The detector itself contributes to the total noise, as well, due to leakage current. In all modern readout systems transistors are the most important elements since they provide the necessary gain for signal amplification. The noise of a transistor depends on many factors: semiconductor material used for the transistor production, type of the transistor, its design and size. In this work we will discuss only silicon field-effect transistors (FETs), since they are the prevailing type of transistors used in particle detector readout electronics, and electronic circuits overall. They are easily integrated with the detector due to their radiation tolerance [84] and the capability to successfully operate at low temperatures, needed for some detectors (Ge detectors, for example). FET transistors are divided into two groups, based on their construction: junction-gate FET (or JFET) and metal-oxide-semiconductor FET (or MOSFET). Both JFETs and MOSFETs can be n-channelled and p-channelled.

The dominant source of noise in FETs, and therefore preamplifiers, is thermal fluctuation of the channel current, called parallel white noise. The second source of series noise is the  $1/f$  noise of the input transistor. The  $1/f$  noise contribution to total noise depends on transistor type. It is more significant in MOSFETs than in JFETs. In JFETs  $1/f$  noise is mainly due to the trapping of the carriers by defects in the channel and their release after a trapping time [85],

[86]. Modern JFETs have very low number of defects in the channel which is why their flicker noise is so low. The cause of flicker noise in MOSFETs is the interaction of the charge carriers with traps in the gate oxide. This results in larger flicker noise (compared to JFETs) which is why MOSFETs were not commonly used for low noise applications. However, modern MOSFETs (especially pMOSFETs) have sufficiently low flicker noise and are used for low noise measurements [83], [87]–[90]. In the charge sensitive preamplifier based on discrete components, JFETs are more common than MOSFETs, especially if the measurement rates are not very high. For preamplifiers realized as ASICs (application-specific integrated circuit) or as a part of fully integrated detector/preamplifier systems [81], [91], MOSFETs are used, because of the CMOS (complementary metal-oxide-semiconductor) technology which enables small feature size and high device density. For general purpose n-channel devices are preferred since they have lower thermal noise, due to higher electron mobility in silicon. For measurements of low rates of particles, where flicker noise is dominant, p-channel devices are used since they have lower flicker noise.

Low noise on its own is not enough if the signal is very low, as well. Therefore, instead of comparing the raw noise value between different devices signal to noise ratio (SNR or S/N) defined as the ratio of signal power to noise power is used. Other important parameters of the detector system are the lowest detectable energy as well as the energy resolution, both determined by the noise of the system. Therefore, development of low-energy detectors relies on noise optimization and low-noise devices.

The dominant source of electronic noise can be the detector itself but also other elements of the system, such as biasing power supply or even the amplification stage of the preamplifier, depending on the detector material and preamplifier design. Therefore, the output signal of the system can be considered as the superposition of the “noiseless” signal from the detector and the noise coming from different sources. Consequently, some information carried by the detector signal is lost or “buried” under noise.

Generally, the detector itself, as well as any element of the amplification circuit are a source of noise. Each element of the detector/preamplifier system would contribute differently to the overall noise, depending on the type of the detector and the design of the preamplifier. Depending on their performance, either detector or preamplifier noise would dominate the total noise. The leakage current is the main contribution to detector noise. The leakage current depends on the type of the detector, its size, the magnitude of the applied electric field and temperature. The higher the leakage current the higher the noise figure. For diamond detectors the leakage current is small even at room temperatures, due to the high resistivity of diamond,

and therefore, its contribution to the overall noise of the system is small. The load resistor of the detector biasing circuit as well as the feedback resistor of the preamplifier are sources of thermal noise. For easier analysis, preamplifier noise can be considered to originate dominantly from the first amplification stage i.e., the input transistor. This assumption is justified because if the input transistor has high gain, contribution of other preamplifier components to the overall noise is negligible. In that case SNR after the input transistor is significantly higher compared to SNR before it. For detector/preamplifier systems it is useful to quantify the noise in terms of equivalent noise charge (ENC). ENC is defined as the amount of charge needed at the input of the noiseless system to produce the output signal of equivalent power as the noise in the real system. In other words, ENC is the amount of charge that would result SNR of the system to be equal to one. We have already stated the importance of high open loop gain of the operational amplifier for insensitivity of the preamplifier gain to detector capacitance. Besides the high open loop gain, the operational amplifier should have low noise, as well. Since the dominant noise contribution in the operational amplifier comes from the input stage, the input stage design is very important. To have SNR as high as possible we should increase the signal and lower the noise. As we shown in the previous part, for high energy transfer between the detector and the preamplifier i.e., high signal, the detector capacitance needs to be small. We will now see how to make the noise of the system as low as possible. For a set operating current of a transistor both transconductance  $g_m$  and the input capacitance  $C_i$  are proportional to the width of the device, that is:

$$\frac{g_m}{C_i} = \text{const.} \quad (3.18)$$

In that case we can express SNR as:

$$\left(\frac{S}{N}\right)^2 = \frac{(Q_s C_{tot}^{-1})^2}{e_n^2} = \frac{g_m Q_s^2}{4kT\gamma\Delta f (C_d + C_i)^2} \quad (3.19)$$

Where  $Q_s$  is the signal charge, equal to the total charge  $Q$  in equation 3.17,  $C_{tot} = C_d + C_i$  is a total capacitance seen at the input of the preamplifier (equal to the sum of the detector capacitance  $C_d$  and capacitance of the preamplifier input stage). Here we used the following equation for the thermal noise of FET:

$$e_n^2 = \frac{4kT\gamma\Delta f}{g_m} \quad (3.20)$$

Where  $k$  is the Boltzmann constant,  $T$  is temperature in Kelvin,  $\gamma$  is an empirical parameter which depends on the operation region of the transistor (usually equal to 2/3) and  $\Delta f$  is the frequency bandwidth. Equation 3.19 can be written as:

$$\left(\frac{S}{N}\right)^2 = \frac{Q_s^2}{4kT\Delta f} \left(\frac{g_m}{C_i}\right) \frac{1}{C_i\left(1+\frac{C_d}{C_i}\right)^2} = K \frac{1}{C_i\left(1+\frac{C_d}{C_i}\right)^2} \quad (3.21)$$

Where  $K = \frac{Q_s^2}{4kT\Delta f} \left(\frac{g_m}{C_i}\right)$  is constant for a set operating point of the transistor. To determine optimal input capacitance of the preamplifier in relation to the detector capacitance we will find a maximum of the SNR by setting the derivative of 3.21 to zero:

$$\frac{d}{dC_i} \left( \left(\frac{S}{N}\right)^2 \right) = \frac{d}{dC_i} \left( K \frac{1}{C_i\left(1+\frac{C_d}{C_i}\right)^2} \right) = 0 \quad (3.22)$$

From equation 3.22, SNR is maximal for  $C_i = C_d$ . The fact that the SNR is maximal when the input capacitance of the preamplifier is equal to the detector capacitance is called capacitive matching. For a fixed detector capacitance, capacitive matching limits the increase in SNR by increasing gain of the amplification stage (by increasing the width of the transistor and thus increasing transconductance). The increase in signal amplitude in that case wouldn't increase SNR because higher input capacitance of the preamplifier would cause higher noise. It is clear from 3.17 and 3.22 that for high SNR both detector capacitance and preamplifier input capacitance should be as small as possible. For high capacitance detectors a possible solution for the capacitive mismatch could be having multiple transistors at preamplifier input or placing a transformer between the detector and the preamplifier to match the detector capacitance. However, having multi transistor input or a transformer is not always practical, and the parasitic effects often reduce the transformer performance. It should be noted that in equation 3.22, same as in 3.17 parasitic capacitance at the input stage of the preamplifier influences the SNR and thus should be as low as possible.

### 3.6 Methods for noise mitigation

Besides the noise coming from the detector and the preamplifier, there is also electromagnetic interference originating from the surroundings of the detector/preamplifier system, that can interfere with the signal. Fortunately, this can be mitigated in a well-designed system.

Electromagnetic interference can originate from any circuit or system that has a coupling method to the detector/preamplifier system. Examples include any radiative circuit that can be “noisy”; experimental chamber auxiliary systems, such as vacuum pumps, valves, vacuum meters; wireless internet signal present in the experimental hall and many others. Even though other parts of the processing system are also sensitive to noise, the detector itself and coupling between the detector and the preamplifier is most noise prone since the signal at that point is very low. After the amplification in the preamplifier the signal level is higher and therefore, much more noise resilient. Noise mitigation techniques mainly consist of decreasing the coupling between the detector/preamplifier system and the source of noise or providing a preferred path for noise signals, so they go “around” the detector/preamplifier system. Isolating the detector/preamplifier system from the surroundings means creating a Faraday cage around the detector and the preamplifier, which in our case is the experimental chamber itself, and using shielded cables, since the cables are especially prone to electromagnetic interference. The second method of noise mitigation consists in creating a low impedance path to ground plane for the noise signal. Grounding is the fundamental way of providing low impedance return path both for signal and biasing currents. Grounding should have low impedance and be as short as possible, to minimize the voltage drop across the grounding line. If the system is grounded at more than one point the ground loops are formed. That opens the possibility of current flowing between the two or more grounding points at different potentials, which also can add unwanted components to the main signal. Apart from minimizing contribution of the surroundings to the overall noise and minimizing noise in the detector/preamplifier system itself, special care should be given to minimizing the influence of auxiliary systems, such as biasing circuit and power circuits. The most effective way of achieving that is placing low pass filters between the biasing circuit and the detector and the powering circuit and the preamplifier. Since both biasing and powering of the system are DC signals, low pass filter would significantly reduce the noise spectral power that can reach the detector or preamplifier. Another way to reduce the thermal noise in the first amplification stage of the preamplifier is cooling. Cooling would not only reduce the thermal noise but also increase the mobility of charge carriers in the channel of the input FET, increasing  $g_m$ . Cooling the detector would also reduce noise for most semiconductor materials, however, due to its wide bandgap, lowering the temperature has no significant effect on noise (leakage current) of the diamond detectors.

# 4 Detector development and experimental methods

## 4.1 Ion microprobe end station and IBIC technique

All measurements presented in this work were performed at the Laboratory for Ion Beam Interactions at Ruđer Bošković Institute. The laboratory operates two electrostatic particle accelerators: 6 MV EN Tandem Van de Graaff and 1 MV HVEE Tandetron. The ions are created in one of four ion sources: NEC Multi cathode SNICS and NEC Alphasross, used with 6 MV EN Tandem Van de Graaff; NEC Single cathode SNICS and HVEE Duoplasmatron, used with 1 MV HVEE Tandetron. Four ion sources and two accelerators enable a multitude of ion species (from protons to Au ions) with a wide range of energies (from 100 keV H to 36 MeV I ions) to be created. There are 9 different end-stations at the laboratory, equipped for different experimental techniques. Some of the techniques used for ion beam analysis and/or material modification are RBS (Rutherford backscattering spectrometry), PIXE and PIGE (particle-induced x-ray and gamma emission), ToF-ERDA (time of flight elastic recoil detection analysis) and IBIC (ion beam induced charge). More about the accelerator system and techniques used at Laboratory for Ion Beam Interactions can be found at [92].

The ion microprobe ( $\mu$ Probe) end-station and IBIC technique was used for the measurements reported in this work. This is a low current technique, meaning that the ion beam current is very low (usually in the picoampere range). Ion microprobe focuses the ion beam on the sample so it can be analyzed with high spatial resolution (down to 200 nm [93]). The ion beam goes first through a magnetic scanner module, made of four magnetic coils placed in pairs - two vertically and two horizontally, so the ion beam passes through the middle, where magnetic field is strongest. Magnetic scanner, also called magnetic deflector module, is used for controlling the position of the beam in the vacuum chamber. The current through the coils (therefore, the

position of the ion beam) is controlled by the data acquisition system [94]. The focusing of the ion beam is done by the focusing magnets, placed after the scanner module. There are total of three quadrupole magnets that focus the ion beam: the first and the third are focusing in the horizontal plane, while defocusing in vertical, the second magnet focuses in the vertical plane, while defocusing in horizontal. This is called triplet quadrupole lens focusing. The focal point of the system is set to the position of the sample inside the vacuum chamber. The current through the focusing magnets is a function of ion species, energy, and charge state (magnetic rigidity) and is set at the beginning of each measurement. Power supplies used for scanning and focusing system of the ion microprobe need to be very precise and very stable over time and operating temperature range to ensure the properties of the ion beam don't change throughout the measurements, which can last several hours. The sample is mounted inside the vacuum chamber at operating pressure of around  $1 \times 10^{-6}$  mbar. The sample holder allows for three axis translation and one axis rotation movement of the sample. For measurements which require sample movement with high precision a piezo stage with nanometer precision can be used. There are several feedthroughs mounted on the chamber so the signals from the sample or other detectors and temperature probes, as well as biasing and powering voltages, can be processed. The layout of the ion microprobe end-station is shown in fig 4.1 [95, p. 37].

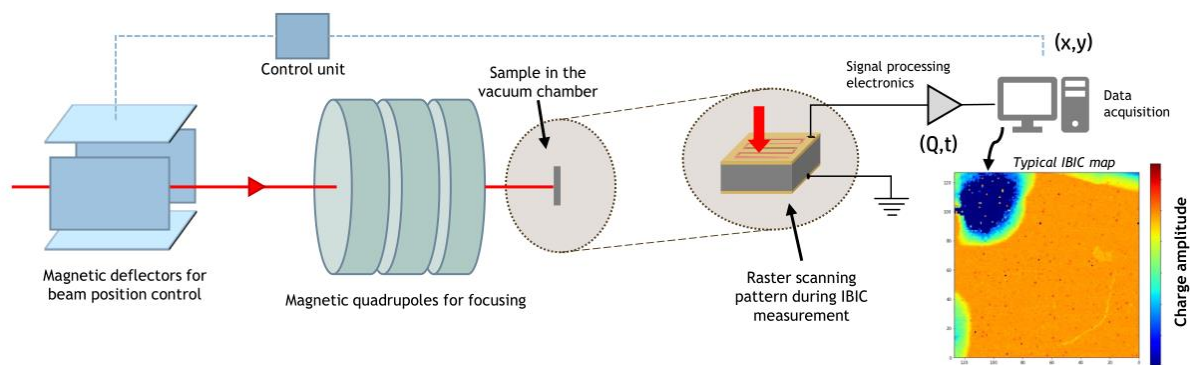


**Figure 4.1:** Layout of the ion microprobe for IBIC. [95, p. 37]

There are several different techniques available at the ion microprobe end-station: PIXE, MeV SIMS (secondary ion mass spectroscopy), IBIC. The ion beam induced charge technique is based on the interaction of ions with the semiconductor material (processes described in chapters 3.1 and 3.2). The signal is generated in the sample itself and collected on the electrodes due to the electric field present in the sample. The signal is then processed and recorded by the data acquisition system with real time data being shown on the computer screen as histograms



and IBIC maps. The illustration of the IBIC technique at ion microprobe end-station is shown in figure 4.1. Each IBIC map presented in this work consists of 128 by 128 pixels. To obtain the size of a pixel for each map an IBIC image of the calibration grid, recorded by a surface barrier detector was scaled by the scan size value.

Since the sample in IBIC measurements is essentially detecting each impinging particle, the sample itself is often referred to as detector and IBIC is considered to be a single ion technique. This is different from the other techniques where the signal originating from the sample is detected by an external detector. The amplitude of the induced signal is proportional to the energy of the impinging ion; however, the signal's amplitude is also influenced by impurities, traps, and electric field distribution within the sample. This is why IBIC is often used, in conjunction with ion microprobe for detector characterization.

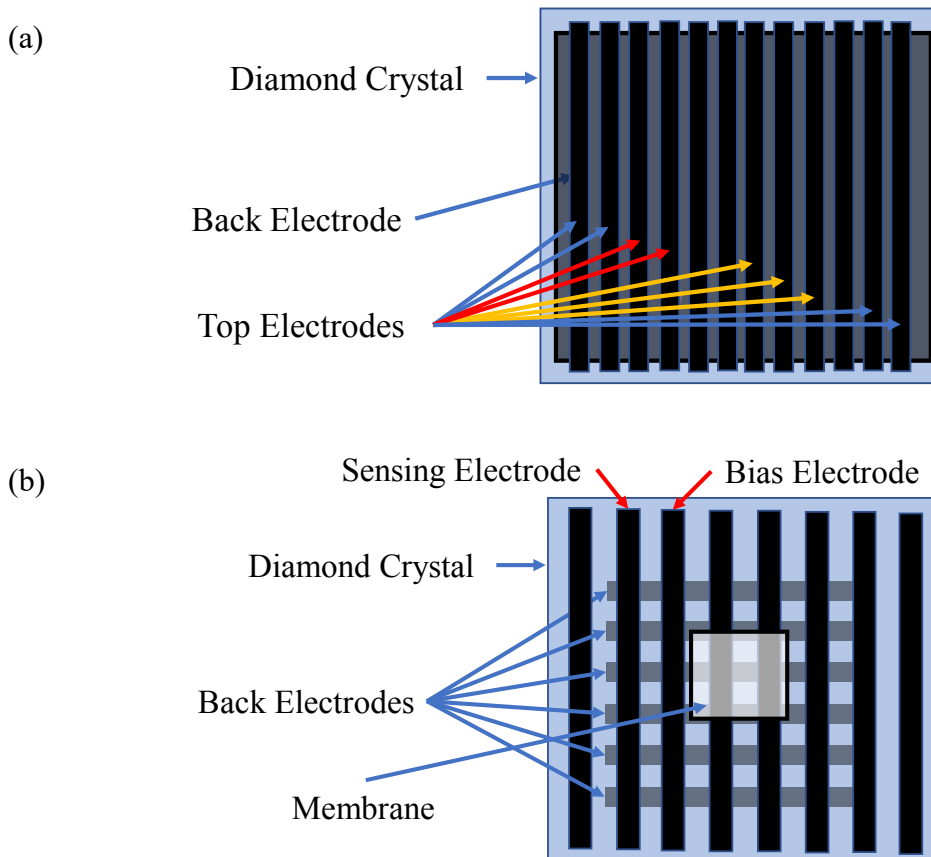
### 4.2 Diamond samples

A total of four diamond samples, with different electrode geometries, were used in this study. All samples were single crystal, electronic grade, CVD diamonds produced by Element Six Ltd. and were the highest quality commercially available diamonds at the time, with resistivity higher than  $10^{11} \Omega \text{ m}$ . All the samples had aluminum electrodes with nominal thickness between 100 nm and 200 nm, fabricated by sputtering technique in the Diamond Sensors Laboratory, CEA-LIST Institute, Paris.

Sample N1 is a  $2 \text{ mm} \times 2 \text{ mm} \times 0.5 \text{ mm}$  diamond with planar electrode configuration. A rectangular,  $1 \text{ mm} \times 1 \text{ mm}$ , electrode was sputtered on the top surface, and a  $2 \text{ mm} \times 2 \text{ mm}$  electrode was sputtered across the whole bottom surface. Both electrodes were 200 nm thick. The electric field distribution within N1 diamond is mostly uniform (except around the edges of the top electrode), which makes N1 ideal for referent and calibration measurements. Moreover, low capacitance of this sample (0.2 pF), resulting in low noise of the output signal, makes it a good candidate for energy calibration.

Sample D11 (fig. 4.2 a)) is a  $4.5 \text{ mm} \times 4.5 \text{ mm} \times 0.3 \text{ mm}$  diamond with 12 strip electrodes at the top surface and a one-piece electrode covering the bottom surface, all 200 nm thick. The top strip electrodes are 0.2 mm wide and 0.2 mm apart, except for the electrodes at the edge of the sample that are a bit narrower. Unfortunately, some of the strips are not perfect rectangles but get wider towards the middle, decreasing the interstrip gap. Therefore, only the strips with sufficient interstrip distance to keep the surface leakage current low were used.

Sample D12 (fig. 4.2 b)) is a  $3\text{ mm} \times 3\text{ mm} \times 0.1\text{ mm}$  diamond with 8 strip electrodes at the top surface and 6 strip electrodes at the bottom surface rotated by  $90^\circ$  with respect to the top electrodes. All electrodes are nominally  $100\text{ nm}$  thick. D12 also has a  $1\text{ mm} \times 1\text{ mm}$  rectangular area in the middle of the sample etched to the thickness of only  $6\text{ }\mu\text{m}$ . This part of the sample was designed for measurements with very high electric fields and was not used in this study. Only two top electrodes, together with all 6 bottom electrodes, were used, as indicated in figure 4.2 b).



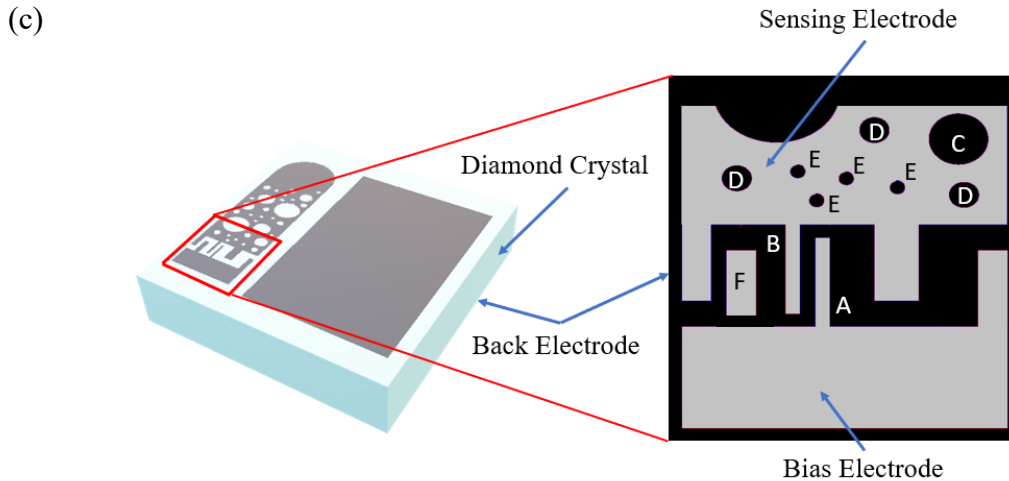


**Figure 4.2:** Layout of (a) D11, (b) D12, and (c) D13 diamond sample [96]. Yellow arrows in (a) mark electrodes used in planar configuration while red arrows in (a) and (b) mark electrodes used in interstrip configuration

Sample D13 (fig. 4.2 c)) is a  $4 \text{ mm} \times 4 \text{ mm} \times 0.04 \text{ mm}$  diamond with four electrodes on the top surface and a one-piece electrode covering the whole bottom side. The large area of the sample allowed for the top electrodes to be designed for two different purposes. A  $3.8 \text{ mm} \times 1.3 \text{ mm}$  electrode is dedicated for measurements in planar mode together with the back electrode, while the other electrodes were designed for detection of low energy ions. In this study two top electrodes (indicated by a red rectangle in fig 4.2 c)) and the bottom electrode were used. We can distinguish a sensing electrode (the electrode connected to a preamplifier) and a bias electrode (the electrode connected to biasing voltage power supply). Sensing electrode has a total of 8 circular openings (or holes) of different diameters: one  $50 \mu\text{m}$  hole (marked with C), three  $30 \mu\text{m}$  holes (marked with D) and four  $10 \mu\text{m}$  holes (marked with E). It also has a  $10 \mu\text{m} \times 100 \mu\text{m}$  strip (marked with B). Biasing electrode together with the sensing electrode creates several interstrip regions with different distance between the sensing and biasing electrodes. Only one such region was used a  $10 \mu\text{m} \times 80 \mu\text{m}$  interstrip region created by a  $10 \mu\text{m} \times 100 \mu\text{m}$  strip of the bias electrode (marked with A), and the strip B of the sensing electrode. In the first version of D13 the sensing electrode was larger and consisted of more holes. Unfortunately, the capacitance of such a large electrode was too high and we had to split it into two separate electrodes. Figure 4.3 a) and b) show the original sensing electrode layout and the layout after the splitting, respectively. Only one of the two electrodes created by splitting was used, while the other one, together with a rectangular electrode F, was not used in this study but left floating.

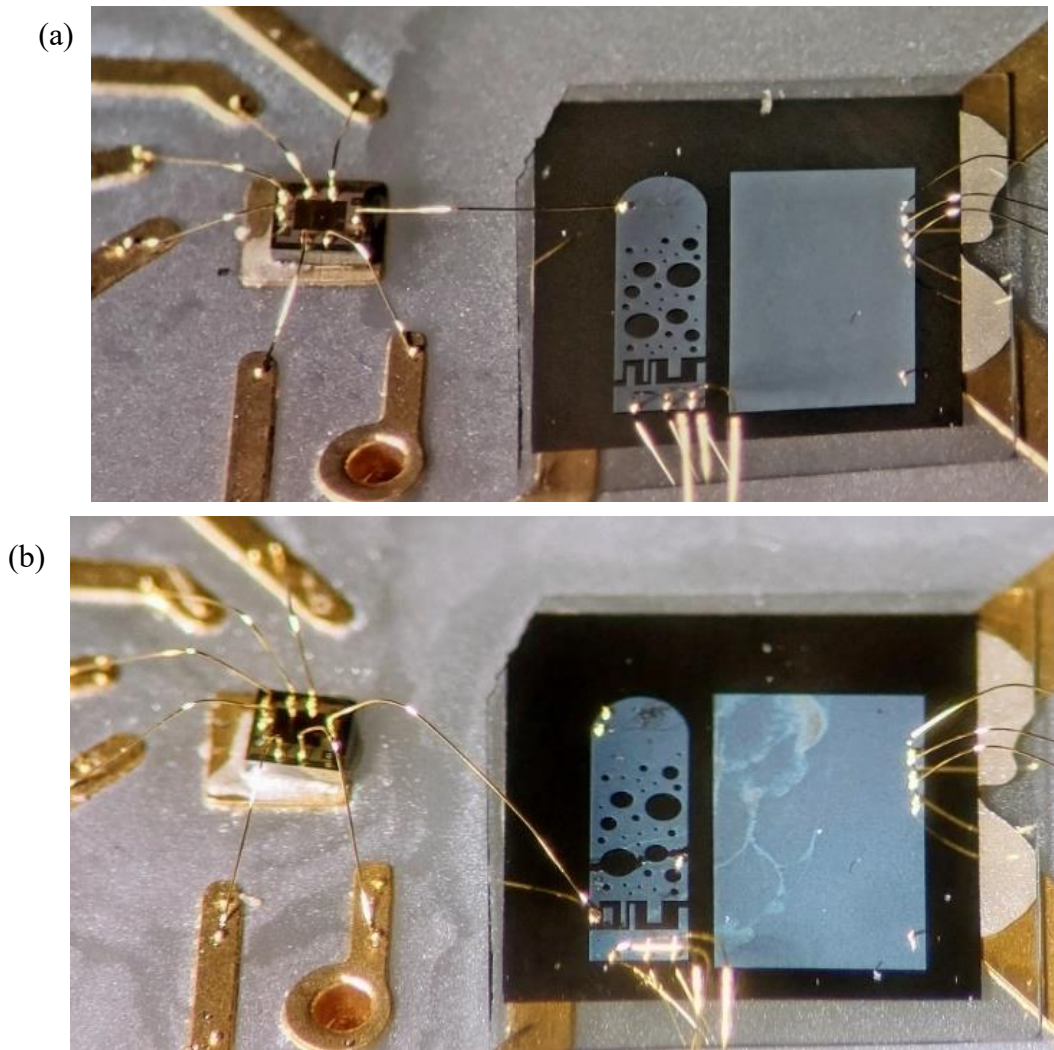


**Figure 4.3:** Layout of D13 diamond (a) before, and (b) after the splitting of the sensing electrode.

### 4.3 Readout electronics

In chapter 3 we've outlined the importance of readout electronics in providing amplification of the signal from the detector while filtering the noise thus enabling easier processing and extraction of detector and impinging particle parameters from the signal. We singled out the preamplifier as the most important device in the signal processing system. Therefore, for all the measurements reported in this work we used low-noise, high gain preamplifiers, connected to a shaping amplifier and an ADC designed for particle detector applications. Two different preamplifiers were used: Amptek A250 and XGLab CUBE PRE\_031. Both are charge sensitive preamplifiers and both were used in DC coupling mode, i.e., the output of the detector (sensing electrode) was directly connected to the input of the preamplifier. Both preamplifiers can be

used in vacuum which means they can be located very close to the detector lowering parasitic capacitance and consequently noise.

### 4.3.1 Amptek A250

Amptek A250 is widely used for low-noise detection applications due to its versatility and ability to function in vacuum. The device itself comes in dual in-line package, with the chip enclosed in metal, to reduce interference. It is commonly used together with the PC250 PCB, designed for testing, and using A250 with particle detectors. The schematic of PC250 with A250 is shown in figure 4.4.

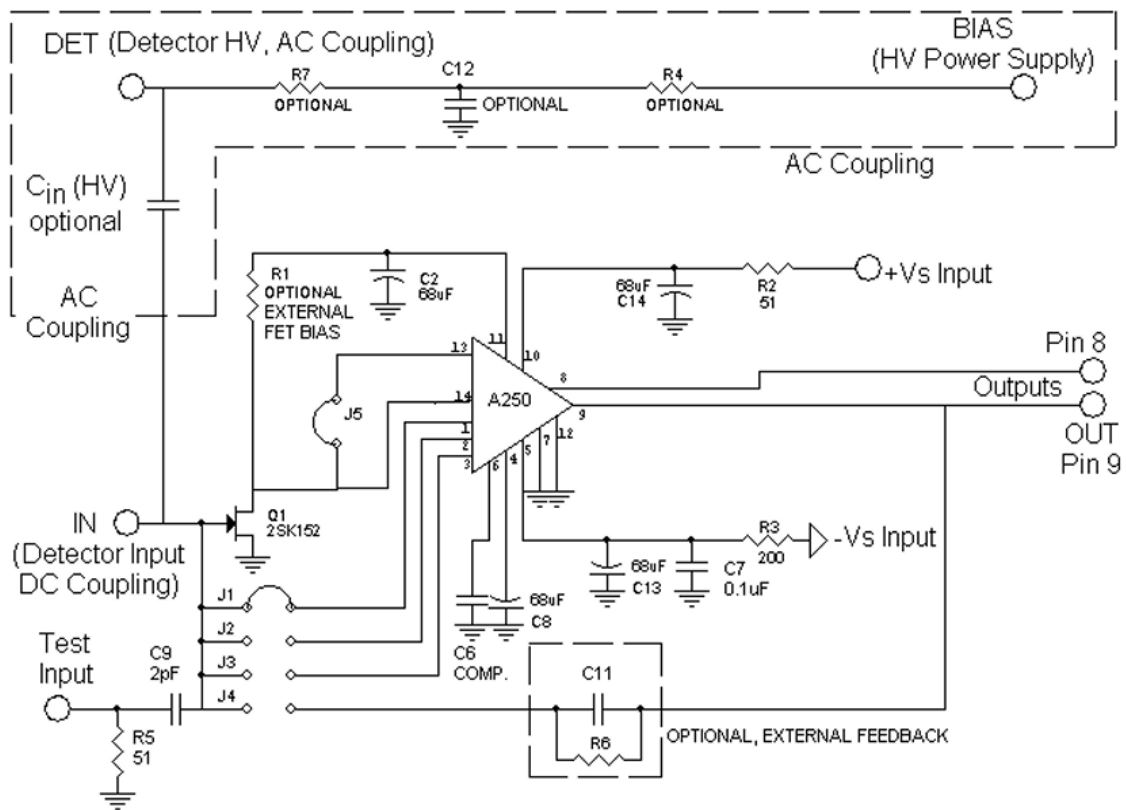


**Figure 4.4:** Schematic of PC250 PCB with A250. [97]

It's noticeable from the schematic that DC coupling is the default configuration of the PCB, with space provided for AC coupling components. However, the main feature of A250 (and PC250 board) is that the setup is fully configurable regarding detector capacitance and gain of the preamplifier. The input FET is not integrated within A250 chip but separated as a discrete component (transistor Q1 in fig 4.4). Feedback capacitance is also adjustable, with 1 pF, 2 pF

and 3 pF capacitors integrated in the A250 package and available at J1, J2 and J3 jumpers, respectively. Jumper J4 enables the user to add a feedback resistor and capacitor best suitable for a specific application. Having a discrete (and changeable) input FET and adjustable feedback means that the preamplifier can be configured to best match the capacitance of the detector and the gain needed for subsequent signal processing, respectively.

For the measurements reported in this work with A250 we used Sony 2SK152 n-channel JFET, provided by Amptek, with 8 pF input capacitance. For the feedback we decided to use 0.1 pF capacitor in combination with 1 G $\Omega$  resistor. In that way we increased the nominal sensitivity of the preamplifier from the standard 0.16  $\mu$ V/electron to 1.6  $\mu$ V/electron (185 mV/MeV for diamond). It should be emphasized that the declared sensitivity is only nominal sensitivity since the parasitic capacitance originating from the soldering of the feedback capacitance increases the total capacitance in the feedback loop, decreasing the effective sensitivity. The preamplifier is also available as a general-purpose device (A250CF), already configured and enclosed in metal housing, with feedback capacitance of 0.5 pF and cooled input FET. However, in that version it is not suitable for vacuum.

### 4.3.2 XGLab CUBE PRE\_031

XGLab CUBE PRE\_031 is the other preamplifier used in measurements. The schematic of CUBE preamplifier is given in figure 4.5. Even though CUBE is a charge sensitive preamplifier suitable for vacuum applications, same as Amptek A250, the two devices differ significantly. Whereas A250 is meant to be used with discrete input transistor and fully configurable, CUBE comes as a bare silicon die and cannot be altered in any way. Therefore, there are different versions of CUBE preamplifier with different gain and input capacitance.

Being a fully integrated device, CUBE preamplifiers have a MOSFET input transistor, whereas A250 has a JFET at the input. As we mentioned in chapter 3, JFETs have lower flicker noise compared to MOSFETs, but MOSFETs are more suitable for higher counting rates. Therefore, it is no surprise that CUBE preamplifiers have a transistor reset mechanism, suitable for high rates of particles, compared to a resistor reset of A250. However, the most important difference (for measurements described in this work) between the two is that A250 is a bipolar device, that is, it can amplify signals coming both from electrons and from holes, whereas CUBE PRE\_031 is a unipolar device, amplifying only signals induced by electron drift. There are other versions of CUBE preamplifiers suitable for detection of signals induced only by holes or signals induced by both electrons and holes (same as A250). However, the best performance (in terms

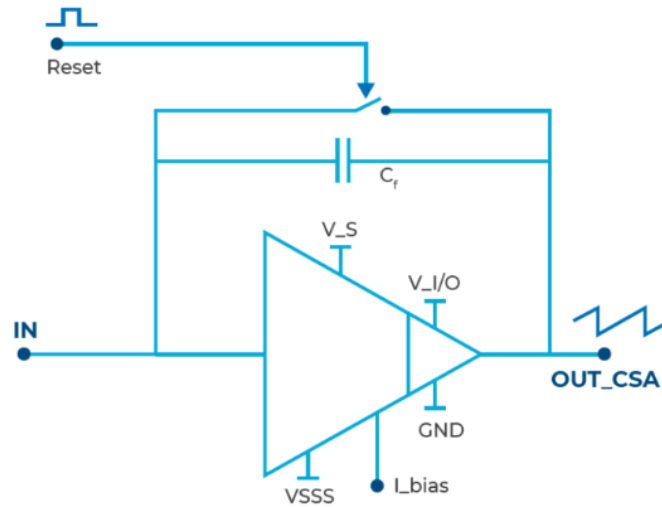


**Figure 4.5:** Schematic of XGLab CUBE PRE 031 preamplifier. [80]

of low noise and high gain) is achieved by CUBE versions designed for detecting only electron signals. The version of CUBE we used (PRE\_031), is suitable for detector capacitance lower than 0.5 pF. It has 25 fF feedback capacitance which makes nominal sensitivity of 757 mV/MeV for diamond detector. More than four times the sensitivity of A250. Moreover, the minimum declared noise of CUBE is only 3 electrons, an order of magnitude less than A250. However, coming as a bare die, CUBE preamplifiers need to be mounted on the same PCB as the detector itself and wire bonded to the detector. Placing the preamplifier close to the detector minimizes parasitic capacitance at the input of the preamplifier, resulting in low noise. However, the fact that preamplifier needs to be glued to the PCB and bonded to the detector limits the usage of a single preamplifier only to one detector, whereas a single A250 could be used with unlimited number of different detectors. This increases the cost of research since every new detector prototype requires a new preamplifier.

### 4.3.3 Signal processing system

After the preamplifier the SNR is high enough for signal processing. We used ORTEC 570 shaping amplifier to reshape the exponentially decaying signal from the preamplifier to a gaussian shaped one. Gaussian pulse is more noise resilient and much narrower compared to the signal from the preamplifier. ORTEC 570 has variable gain and variable shaping time so it

can be used with a wide variety of detectors and preamplifiers. It also has pole-zero compensation and base line restorer, which results in accurate output signal amplitude even when the rate of pulses is high. The gain of the preamplifier was adjusted according to the energy of the ion beam used in a particular experiment. The shaping time that resulted in the lowest noise of the system was 6  $\mu\text{s}$  for both A250 and CUBE PRE\_031. The output range of the shaping amplifier is 0-10 V, the same as the input range of the Canberra 8075 ADC, used for data digitization. The digitized data was sent to custom data acquisition system [94] based on a Xilinx Virtex 6 FPGA. By controlling the beam scanner, the data acquisition system controls the beam position. That means that all relevant data: signal amplitude, x and y coordinate of the beam and timestamp of each detected event is recorded and displayed on the screen in real time in form of histograms and IBIC maps (cumulative signal amplitude distribution across the area of the sample scanned by the ion beam), as shown in fig. 4.1. Due to the multiple passing of the ion beam over the region of interest each pixel contains the value of cumulative amplitude. Spector [93], [94] is the software, developed in our lab during the last two decades, used for data visualization and processing. Detailed information of each detected event, recorded by the data acquisition system, enables spatial and temporal correlations between different events to be established in the postprocessing. In that way important characteristic of the detector (such as electric field distribution, polarization, damage, and trapping effects...) can be investigated with high spatial and temporal resolution.

### **4.4 PCB and detector development**

To fully exploit the low noise performance of the preamplifier it is important to keep the parasitic capacitance at the input as low as possible. However, it is equally (if not more) important to keep the noise from the surroundings away from the preamplifier itself. One of the easiest ways for noise coupling from the environment to the preamplifier is via power lines and grounding. Therefore, special care is given to PCB design for preamplifier/detector systems. As already mentioned, A250 preamplifier comes with the dedicated PCB (PC250) which provides power filtering and grounding. PC250 has a relatively small footprint (4.5 cm x 4.5 cm) however, since it doesn't accommodate the detector itself, it can barely fit on the  $\mu\text{Probe}$  vacuum chamber's sample holder. The output of the majority of detectors used in our laboratory is terminated by an SMA connector. Therefore, we decided to use an SMA connector as the input port of the PC250 for easier handling. Connectors on both detector and preamplifier side significantly increase capacitance seen by the input of the preamplifier however, using SMA



connectors for coupling the detector and the preamplifier is much more elegant solution than having to solder and subsequently desolder each new detector to the preamplifier PCB, which could cause heat damage. Moreover, having a stiff connection between the detector and the preamplifier's PCB enables easier manipulation in the tight space inside the vacuum chamber. Power and grounding of the PC250 board was connected to the rest of the system by a flat cable, while a single 27 cm long coaxial cable, terminated by an SMA connector, was used to connect the output of the preamplifier to a feedthrough of the vacuum chamber. Sample D11, used exclusively with A250 preamplifier, was mounted on a simple PCB with two SMA connectors. The first one was connected to the two top electrodes marked by red arrows in fig 4.2 a): center pin to the sensing electrode and shield to biasing one. The center pin of the second SMA connector was connected to the three top electrodes marked by yellow arrows in fig. 4.2 a), while the shield was connected to the back electrode. In that way D11 could be used both in interstrip and planar configuration, depending on which connector is used.

For CUBE preamplifiers a carrier PCB, providing power, reset signal, input, and output line, had to be designed. The same PCB had to accommodate a diamond sample, a connector for all the signals and voltage filters. Table 4.1 shows different voltages needed to power CUBE PRE\_031. Even though power supplies used for powering the preamplifier were stabilized, with very low ripple, and XGL-CBB-1CH biasing board further stabilizes the powering voltages, CUBE carrier board, called RBI Implantation Board had additional filters for power voltages of the preamplifier. Special care was given to separate the reset signal from the DC powering voltages and output signal, to prevent interference. Also, a grounding plane was added at the bottom surface of the PBC to provide a low impedance current return path for all the signals. The PCB accommodates two connectors: a DB9 connector for all signals to and from the preamplifier; and an SMA connector, designed to be connected directly to the detector and used only for testing purposes. A flat cable was used to connect the DB9 connector on the RBI Implantation Board and the XGL-CBB-1CH biasing board, with a vacuum chamber feedthrough between them. Figure 4.6 shows the schematic of the RBI Implantation Board v2.2 with red dashed rectangle marking the preamplifier.

**Table 4.1:** Power voltages for CUBE PRE\_031.

Signal	Voltage [V]	Function
$V_{SSS}$	-3 or -6	Core supply voltage for the ASIC.
$V_{I/O}$	5	Voltage supply for the I/O section of the ASIC.
$V_S$	2	Voltage supply for the input current source.

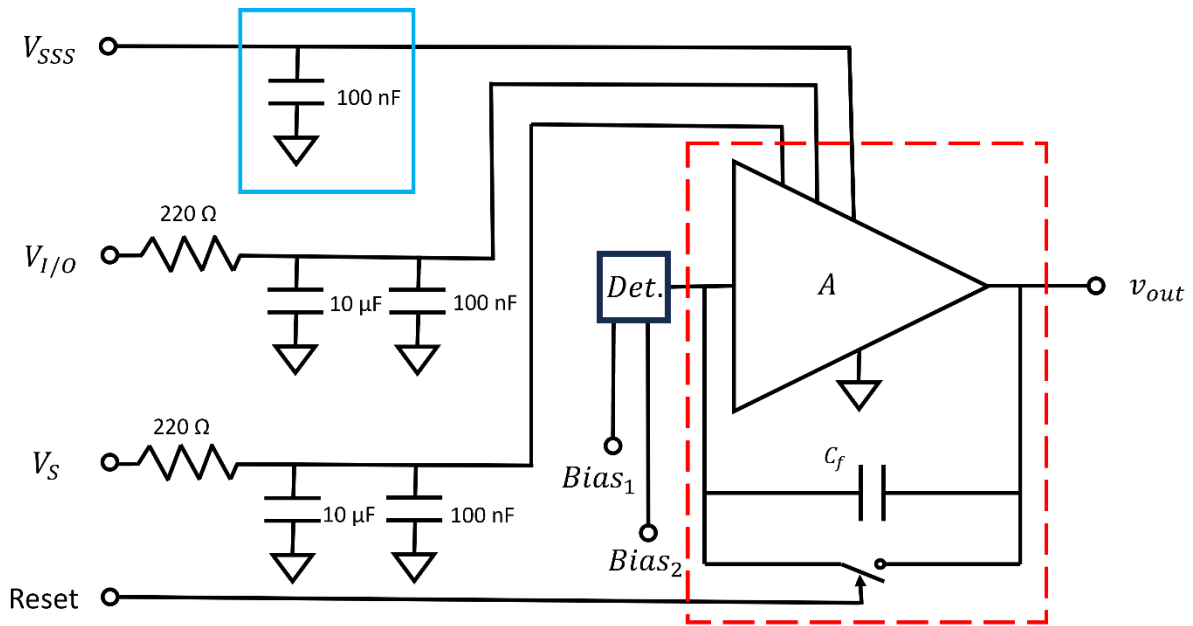


**Figure 4.6:** Schematic of the RBI Implantation Board v2.2 with XGLab CUBE PRE 031 preamplifier marked by the red dashed rectangle. Blue rectangle marks a capacitor that does not exist in RBI Implantation Board v2.0.

Two different versions of RBI Implantation Board were developed: v2.0, made of FR4 and used with D12 diamond; and v2.2 made of AlN and used with N1 and D13 diamonds. The process of design and fabrication of both boards is shown in figure 4.7. The main difference between v2.0 and v2.2 of the RBI Implantation Board (besides the difference in the material of the PCB itself) is the  $V_{SSS}$  voltage filter capacitor present only in v2.2. Whereas v2.0 was intended to be a demonstrator of the low noise detection at room temperature, v2.2 was made of AlN, a material with around two times higher dielectric constant than FR4 and high thermal conductivity – 321W/(m K). High thermal conductivity means that v2.2 is suitable for cooling, which should result in lower thermal noise of the preamplifier, however, high thermal conductivity caused a lot of problems in soldering the components since the PCB itself removed the applied heat from a specific pad and distributed it over the whole board, acting as a heat sink. The layout of v2.2 was also changed compared to v2.0 to eliminate ground loops. The improved layout together with higher dielectric constant of the PCB should result in lower overall noise of RBI Implantation Board v2.2 compared to v2.0.

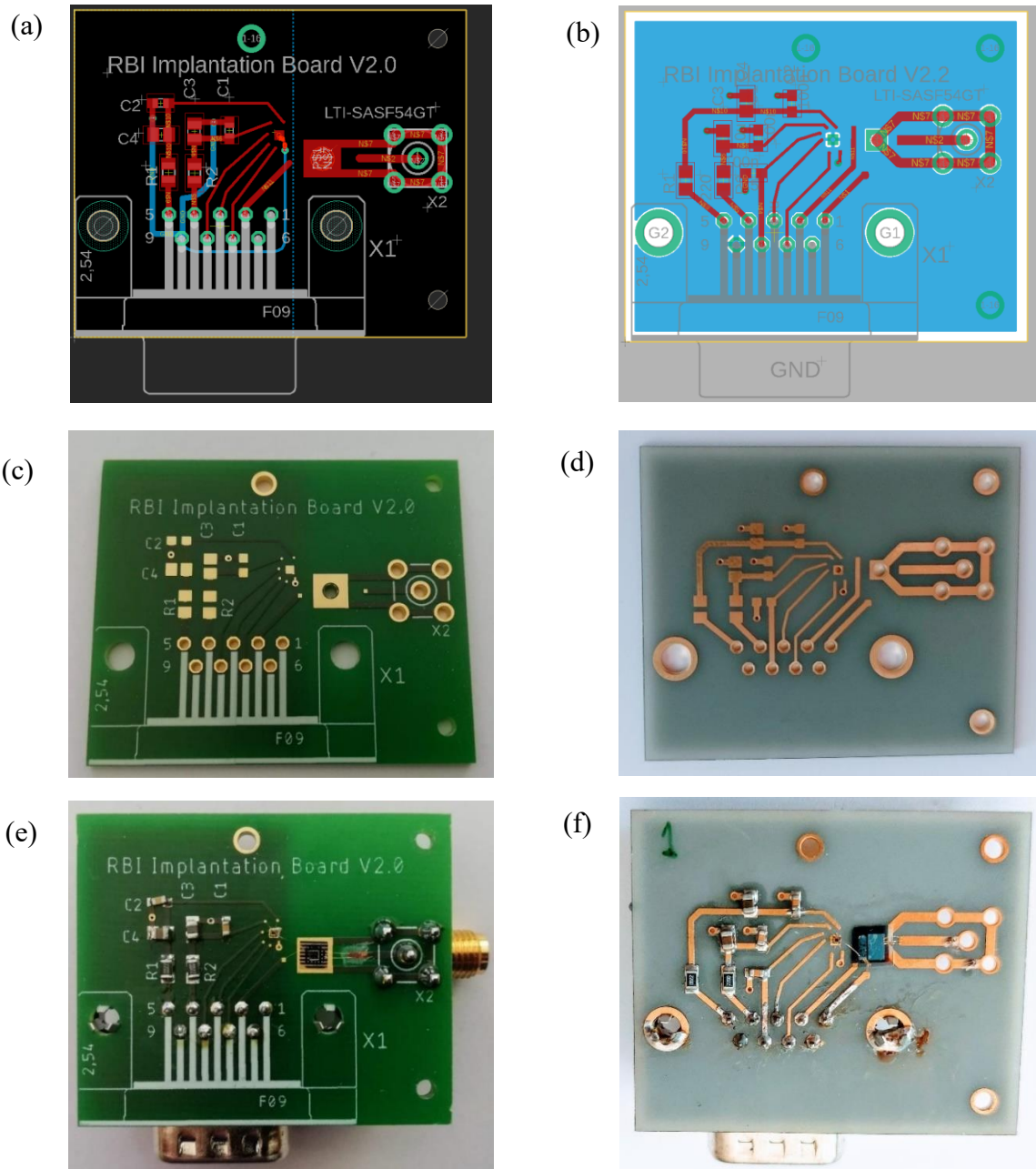


**Figure 4.7:** Design of the RBI Implantation Board (a) v2.0 and (b) v2.2. PCB as received from the manufacturer: (c) v2.0, (d) v2.2. PCB after the components, preamplifier and diamond has been installed: (e) v2.0 with D12 diamond, (f) v2.2 with D13 diamond.

To attach the preamplifier to the PCB we tested different adhesives: silver paste, soldering paste, superglue, and conductive epoxy. Silver paste has very good conductivity, but the adhesion over the small surface area of the CUBE pad was very poor, so the preamplifier was detached in the bonding process. With superglue the adhesion was excellent however, the glue isolated the bottom side of the preamplifier from the pad. The grounding of the preamplifier is available both at the bottom metalized surface of the silicon die and at one pad electrode at the

top surface. When superglue is used as adhesive the return currents must pass through a 50  $\mu\text{m}$  wire that connects the grounding pad to the PCB ground. The inductivity of a single 50  $\mu\text{m}$  wire is very high therefore there is a possibility that the preamplifier can't function properly (especially at high particle rates). Soldering paste seemed to solve both adhesion and grounding problems. However, soldering paste needs high temperature for a good mechanical and electrical connection to be created. Since the AlN PCB has high thermal conductivity, applying high temperature locally is very difficult. Therefore, using soldering paste for attaching CUBE preamplifier to a AlN PCB was seldom successful. Eventually, conductive epoxy proved to be the best solution. It requires no heat for activation, and it shows great adhesion and good conductivity. Figure 4.8 shows the process of attaching CUBE preamplifier to the PCB using soldering paste, although the process is the same with conductive epoxy, except there is no need for applying heat after c).

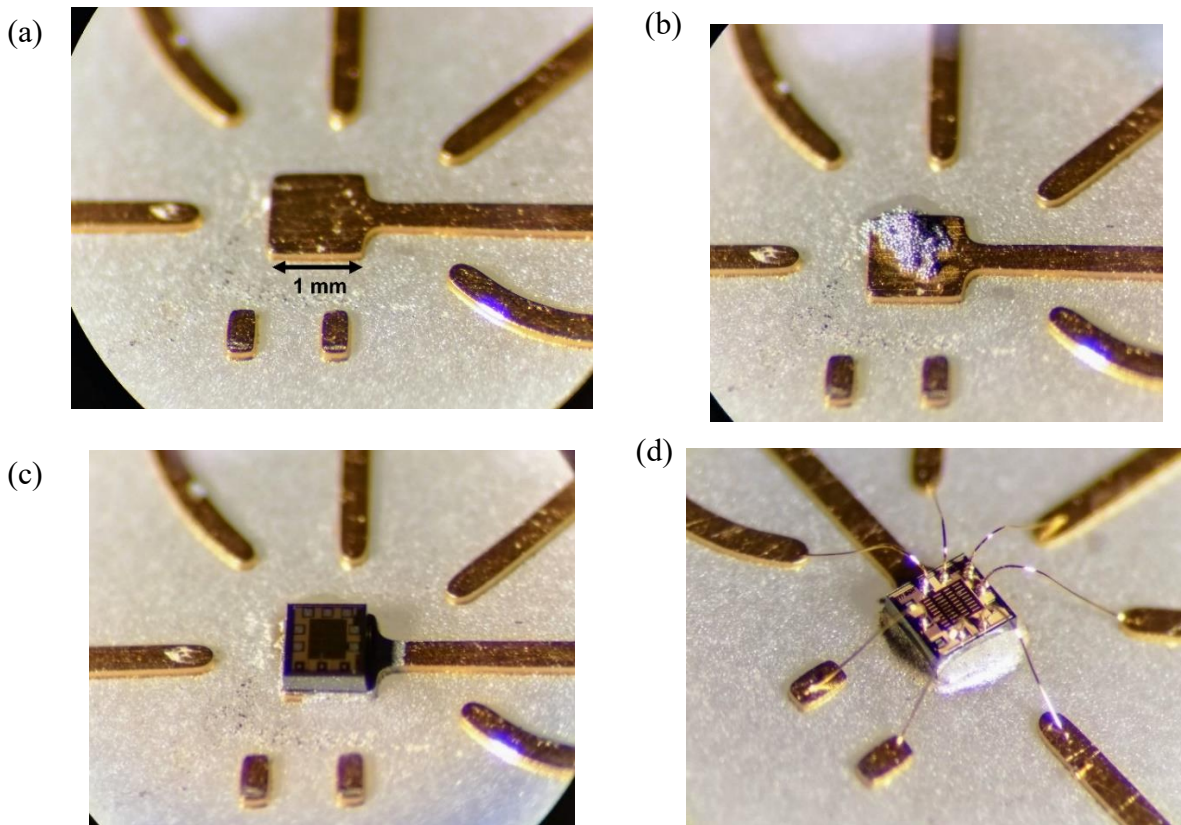


**Figure 4.8:** Process of mounting CUBE preamplifier to a AlN PCB. (a) 1 mm<sup>2</sup> gold pad is clean with isopropyl. (b) Soldering paste is applied to the pad. (c) CUBE preamplifier is carefully placed on the pad and heat is applied until the paste melts. (d) Contacts are wire bonded to the PCB.

## 4.5 Detector/preamplifier cooling system

The intrinsic concentration of free charge carriers (electrons and holes) in diamond is very low at room temperature. It can be shown that even at elevated temperatures the intrinsic concentration of charge carriers would be low (compared to the intrinsic concentration of charge carriers in silicon) [95, p. 10]. This is a direct consequence of diamond's wide bandgap. Low intrinsic concentration of electrons and holes means low thermal noise and leakage current. In fact, thermal noise of diamond detectors is negligible compared to noise in readout electronic and pick-up noise. Therefore, it is not necessary to cool diamond detectors even for low noise application. However, thermal noise in the preamplifier is far from negligible. In the attempt to achieve the best SNR, we designed a simple cooling system for the preamplifier. The system was developed to be used with RBI Implantation Board v2.2 and CUBE PRE\_031 preamplifier, since it is the most suitable PCB for cooling, due to high thermal conductivity of AlN, and CUBE PRE\_031 is the best performing preamplifier used in the presented research. A simplified illustration of the cooling system is shown in figure 4.9. Nitrogen gas was used as coolant. The gas was fed from the pressurized cylinder via 1/4 inch plastic tube to a heat exchanger. The heat exchanger was made of coiled 1/4 inch steel tube submerged in liquid nitrogen. Cooled nitrogen gas was then fed to the  $\mu$ Probe vacuum chamber, via one of the two gas/water feedthroughs. Inside the vacuum chamber an RBI Implantation Board v2.2 PCB was mounted, using a double-sided thermal tape, to a copper heat sink. The heat sink had a channel drilled through it so the coolant can flow inside, removing the heat. A 1/8 inch steel tube was used to connect the heat sink to the chamber feedthroughs. One feedthrough (connected to the heat exchanger) served as the coolant inlet, while the other released the gas, that had passed through the copper heat sink, into the atmosphere.

The liquid nitrogen dewar and the nitrogen cylinder had enough capacity to sustain the flow and cooling of the gas for several hours. Therefore, the cooling system could be used for longer irradiation experiments. A thermal couple was mounted on the RBI Implantation Board v2.2 PCB, close to the preamplifier, to measure the temperature. Even though we noticed a mixture of gaseous and liquid nitrogen being released from the gas outlet, which means that the coolant temperature was very low (nitrogen boiling point is  $-195.8\text{ }^{\circ}\text{C}$ ) the minimum recorded temperature at the PCB (after three hours) was  $-50\text{ }^{\circ}\text{C}$ . The temperature difference of that magnitude meant that there are significant heat gains to the PCB either from the vacuum chamber itself, or via the connection cable. Nevertheless, the achieved temperature was low enough to guarantee a significant decrease in thermal noise.

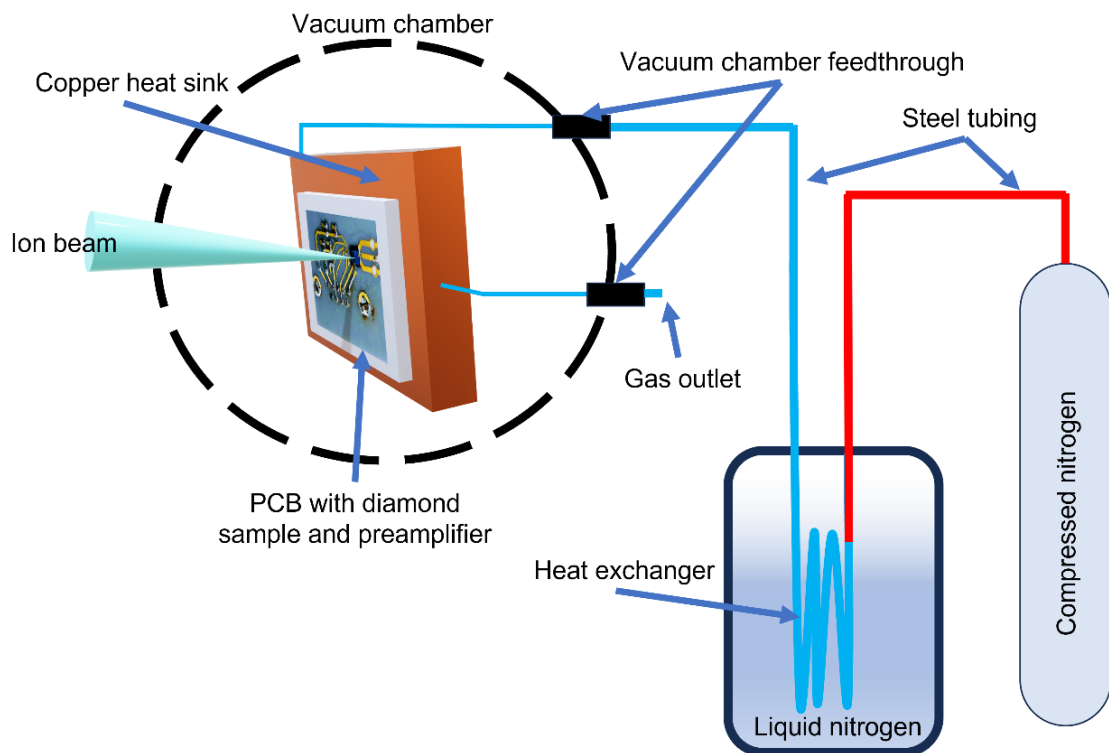


**Figure 4.9:** Illustration of the cooling system at ion  $\mu$ Probe vacuum chamber. Compressed nitrogen gas flows from the pressurized cylinder to a heat exchanger submerged in liquid nitrogen. Cooled gas then flows in the vacuum chamber and through the copper heat sink, via steel tubes, before being released into the atmosphere. The PCB with the detector and the preamplifier is attached to the copper heatsink with a thermal tape.

## 4.6 Ion beam selection and measurement process

All experiments reported in this work were conducted using  $\mu$ Probe end station, regardless of whether they were done using ion beams or referent gamma radiation source. To ensure that any difference in obtained results can't be attributed to the experimental conditions or a faulty piece of equipment all measurements were done in vacuum (pressure  $< 5 \times 10^{-5}$  mbar) and with the same shaping amplifier and ADC modules. The difference between the experiments was in the diamond sample, preamplifier and/or ion beam used.

### 4.6.1 Ion beams

To investigate detector performance and electric field distribution close to the surface and compare it to the bulk performance we used ions of different energies and species. Protons of energies ranging from 100 keV to 4 MeV were used for probing the detector. Protons are the

lightest ions and therefore induce the least amount of damage, compared to any other ion species of the same energy. However, they also have the highest penetration depth which makes them unsuitable for investigating detector properties at small depths. For that purpose, we used heavy copper ions. The least penetrating beam we can accelerate and focus in the  $\mu$ Probe is 140 keV  $\text{Cu}^{2+}$ . Its penetration range in diamond is on average 59 nm, calculated by SRIM. For comparison, the average penetration depth of 100 keV protons is 438 nm, more than 7 times higher. Moreover, 140 keV  $\text{Cu}^{2+}$  ions have nearly identical penetration depth in diamond as 50 keV  $\text{N}^{2+}$ , the ion beam that can be used for creation of NV centers with high spatial precision. Nitrogen ions are usually created by splitting the molecular ion beam ( $\text{CN}^-$  for example) from the ion source in collisions with the stripping gas inside the particle accelerator terminal. Even though that process can be achieved by the two particle accelerators we used, 50 keV is lower than the minimum obtainable energy of the two machines. Table 4.2 shows the ion species used in the presented research, together with their energy and average penetration depth in diamond. The same table also shows the penetration depth of 50 keV  $\text{N}^{2+}$  ions. Figure 4.10 a) shows SRIM simulation of 500 ions in diamond for each of the ion beams used, except for 4 MeV protons. 4 MeV protons penetrate on average 78.8  $\mu\text{m}$ , an order of magnitude more than the next deepest penetrating ion (1 MeV protons). On that scale there wouldn't be a clear distinction in range between other ion species used in the measurements, therefore we decided not to show 4 MeV protons in figure 4.10 a). It is noticeable that besides the difference in the longitudinal range of ions, depending on their energy and mass, there is considerable difference in the lateral straggling, as well. Compared to the 1 MeV protons, distribution of 140 keV  $\text{Cu}^{2+}$  ions is nearly point like. Figure 4.10 b) and c) show distribution of 500 of 140 keV  $\text{Cu}^{2+}$  and 50 keV  $\text{N}^{2+}$  ions, respectively. The difference in range between the two is only 3 nm, with 140 keV  $\text{Cu}^{2+}$  ions being shallower. Lateral straggling is very similar, as well, although it is more pronounced for

**Table 4.2:** Ion beams used in the measurements, their energies and penetration depth in diamond (calculated using SRIM). 50 keV  $\text{N}^{2+}$  beam was added for comparison.

Ion	Energy [keV]	Average penetration depth [ $\mu\text{m}$ ]
$\text{H}^+$	4000	78.80
$\text{H}^+$	1000	8.090
$\text{H}^+$	400	2.100
$\text{H}^+$	100	0.438
$\text{Cu}^{2+}$	140	0.059
$\text{N}^{2+}$	50	0.062

50 keV  $N^{2+}$  ions since they are considerably lighter. This means 140 keV  $Cu^{2+}$  ions can be used to accurately estimate detection efficiency and CCE of 50 keV  $N^{2+}$  ions. Even though the difference in penetration depth between the highest penetrating and the lowest penetrating ion from table 4.2 is three orders of magnitude, it is important to state that in each of the measurements reported in this work the ions fully stop in the diamond samples, i.e., the penetration depth is always smaller than the thickness of the sample. In that way each implanted ion transfers 100 % of its kinetic energy to the detector material.

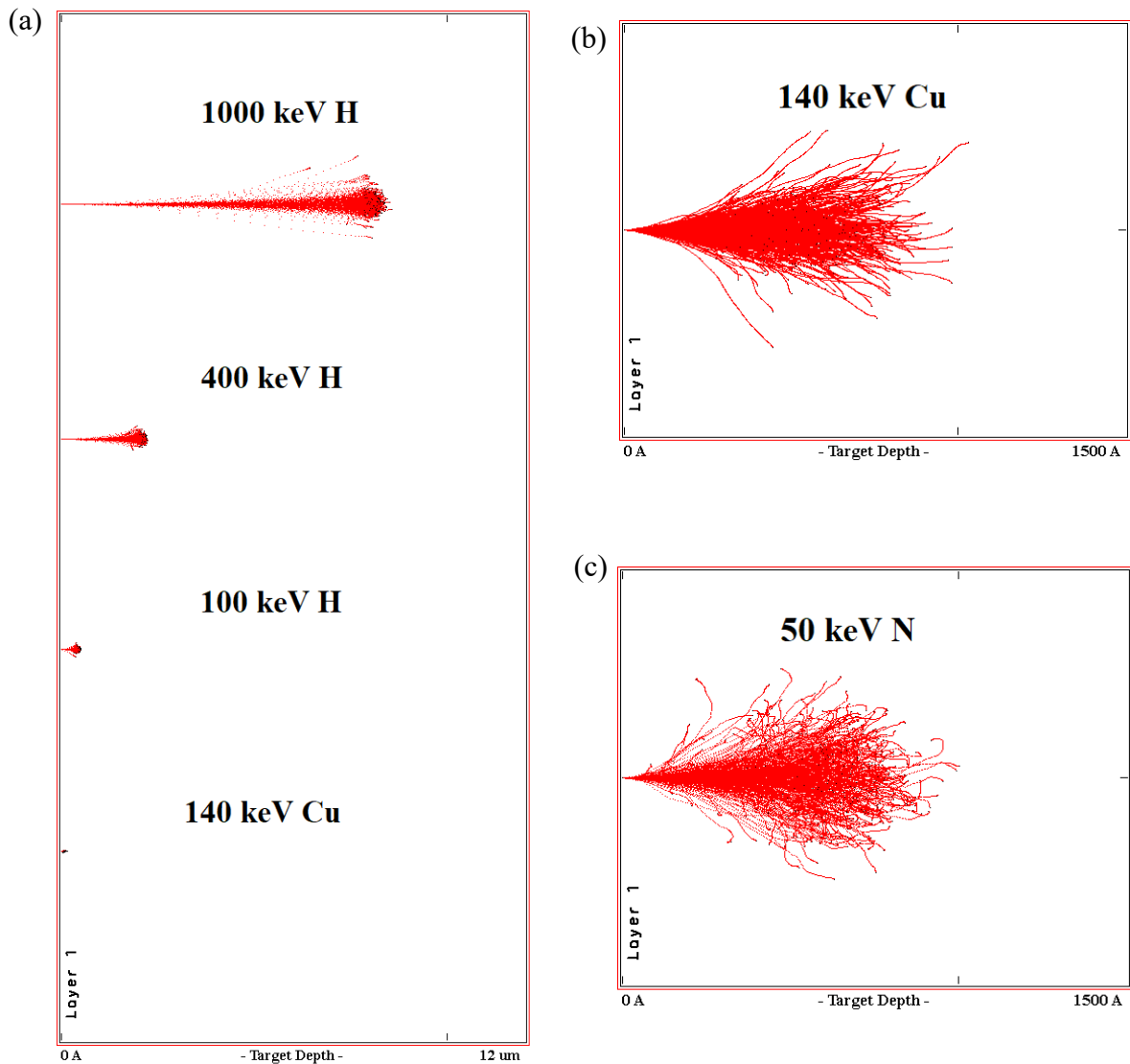


**Figure 4.10:** Simulated distribution of 500 ion in diamond for (a) 1 MeV, 400 keV and 100 keV protons and 140 keV copper ions. Enlarged ion distribution for 500 (b) 140 keV copper and (c) 50 keV nitrogen ions. The simulation was done using SRIM.



### 4.6.2 Measurement process

The main goals of the measurements were: to determine the optimal electrode configuration of the diamond detector for improved CCE in case of shallow ion implantation; to evaluate the minimum detectable energy of a detector/preamplifier system designed using state-of-the-art commercially available diamond crystals and low noise electronics. The minimum detectable energy can be evaluated from the energy resolution, i.e., noise figure of the measured signals. To achieve the set goals, the measurements were divided into three stages, with each stage using a different detector whose design was based on the results from the previous measurement stage.

In the first stage of measurements, we used Amptek A250 preamplifier and D11 diamond. D11 was used both in interstrip (with strips marked by red arrows in fig. 4.2 a) acting as the sensing and biasing electrodes) and planar (three top strips marked by yellow arrows in fig. 4.2 a) used as a sensing electrode while the bottom electrode used for biasing the detector) configuration. The goal was to determine whether interstrip configuration can be used for efficient ion detection and to investigate the difference in detector performance with deep and shallow penetrating ions. In this case deep penetrating beam was 4 MeV protons with penetration depth in diamond of 78.8  $\mu\text{m}$ , and shallow beam was 400 keV protons, with penetration depth of 2.1  $\mu\text{m}$ . Even though 400 keV protons are not strictly considered to be a shallow beam compared to some other beams of lower energy ions used in the subsequent experiments, in this case the difference in range of 400 keV protons compared to 4 MeV protons is so significant that 400 keV proton beam can indeed be considered as shallow. For calibration of the results, we used  $^{241}\text{Am}$  referent gamma source and N1 diamond connected to A250 preamplifier.

The second stage of experiments was done using CUBE PRE 031 preamplifier and D12 sample. D12 has strips both at the top and at the bottom surface, with top strips being perpendicular to the bottom ones. Therefore, the influence of the bottom electrode can be investigated. We used D12 in the interstrip mode, with two top strips marked by red arrows in figure 4.2 b) acting as the sensing and biasing electrode. The ion beams used were 1 MeV, 400 keV and 100 keV protons as well as 140 keV  $\text{Cu}^{2+}$  ions. The goal was to investigate detection efficiency and CCE at different depths, down to very shallow 140 keV  $\text{Cu}^{2+}$  ions. For these measurements the calibration was done using the nominal gain of CUBE PRE\_031 preamplifier. Results obtained by D12 helped us design the electrode layout of D13 sample.

The last stage of measurements was done using D13 sample, which has the most complicated electrode geometry of all the diamond detectors used in this research. The goal was to determine

the best sensing electrode layout for efficient detection of shallow ions over large areas. We used 100 keV and 400 keV protons as well as 140 keV  $\text{Cu}^{2+}$  ions to map detection efficiency and CCE of the detector. For calibration we used N1 sample mounted on the RBI Implantation Board v2.2 and connected to CUBE PRE\_031 preamplifier, same as D13.

For all the samples we performed I-V and C-V characterization prior to the measurements with ions. The I-V measurements were done with Keithley 6487 picoamperemeter with built-in voltage source while the C-V characterization was done using Keithley 4200 SCS. The purpose of I-V characterization was to determine the maximum biasing voltage that is safe to apply to the detector. This was done by determining the point when the leakage current starts to increase exponentially (for diamonds with diode-like characteristics) or when the leakage current exceeds the limit for safe operation of the preamplifier (for diamonds with ohmic characteristics). If neither of the two happened within the applied voltage range, the sample could be used without any restrictions.

To represent the measured data in terms of CCE we used equation 3.16 and definition of CCE in chapter 3.2. Therefore, we get:

$$CCE = \frac{v_{meas}}{v_{100\%}} \cdot 100\% = \frac{v_{meas}}{-\frac{E}{E_i C_f} e} \cdot 100\% \quad (4.1)$$

Where  $v_{meas}$  is the amplitude of the measured voltage signal at the output of the preamplifier and  $v_{100\%} = -\frac{E}{E_i C_f} e$  is the amplitude of the voltage signal at the preamplifier's output in case of 100 % charge collection efficiency (and is equal to  $v_{out}$  in equation 3.16). Here, we assumed that total kinetic energy of an impinging ion is used for EHP creation, neglecting nonionizing processes. This way of calculating CCE is appropriate for light ions (such as protons or nitrogen ions) whose interaction with semiconductor material results in energy loss mainly through ionizing processes (interaction with atomic electrons) whereas it underestimates the CCE for heavy ions (such as copper) that lose significant amount of energy through nonionizing processes (such as collision with atomic nuclei), as well.

# 5 Results and discussion

## 5.1 Diamond sample with top strip electrodes

In the first stage of measurements, we used D11 diamond and proton beam. Protons are good as probing beam since they are light and induce little damage to the crystal, compared to other ion species of the same energy. D11 was used in both planar and interstrip configuration, fig. 4.2 a). The main probing beam was 400 keV protons, used both in planar and interstrip mode, with 4 MeV protons additionally used only in interstrip mode for comparison between a deep and a shallow beam.

Before the measurements with ions, we performed I-V measurements to determine the leakage current as a function of biasing voltage and in turn the maximum biasing voltage that can be applied to the detector. Figure 5.1 a) and b) show I-V curves for planar and interstrip configuration of D11 sample, respectively. It is noticeable that D11 exhibits diode-like behavior: at voltages between -100 V and 100 V the leakage current is very low ( $<10^{-10}$  A),

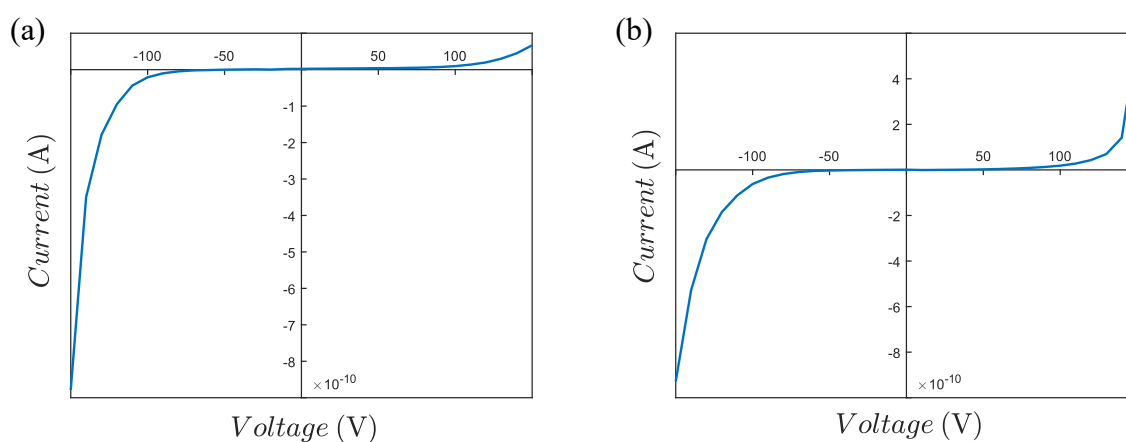


**Figure 5.1:** I-V characteristics of D11 diamond for (a) planar and (b) interstrip configuration.

while it increases exponentially outside that range. It is also evident that the I-V curve is asymmetrical in both planar and interstrip configuration, with the asymmetry more pronounced for planar configuration. Since the diamond is not doped and nominal impurity concentration is very low, the diode-like behavior is probably a consequence of a Schottky barrier at the metal-diamond interface. Although the leakage current was low enough for normal operation of the preamplifier in voltage range between  $-150$  V and  $150$  V, for safe operation of the detector the biasing voltage shouldn't be much higher than  $100$  V or much lower than  $-100$  V. Capacitance of the sample was also measured. In planar mode the capacitance measured between the top three and the bottom electrode, with other electrodes floating, was  $3.6$  pF. In the interstrip mode, the capacitance measured between the sensing and the biasing electrode, with all other electrodes floating, was  $1.4$  pF. In the interstrip mode the capacitance is more than two times lower than in planar mode, which was expected.

### 5.1.1 Calibration of Amptek A250

The preamplifier used with D11 was Amptek A250. Even though the nominal gain of the preamplifier is determined by the feedback capacitance, for more accurate measurements, in case when the capacitor is a discrete component, calibration is needed. For that purpose,  $^{241}\text{Am}$  referent gamma source and N1 sample were used. N1 provides nearly uniform electric field in the whole volume of the detector and is the thickest diamond that was available, both very important when detecting gamma photons. The I-V characteristic of N1 (fig. 5.2) was measured in the same way as with D11. The thickness of N1 sample ( $500$   $\mu\text{m}$ ) compared to D11 ( $300$   $\mu\text{m}$ )

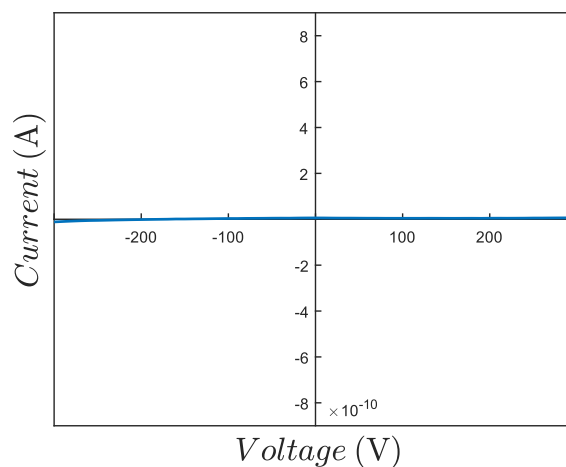


**Figure 5.2:** The I-V characteristics of N1 diamond.

means that the leakage current would be lower, as can be seen in the graph. In the whole voltage range (-300 V to 300 V) the leakage current was well under 0.1 nA, the current that would cause 0.1 V voltage drop at the output of the preamplifier (since the feedback resistor was 1 GΩ). Besides the low leakage current, N1 sample has low capacitance (only 0.2 pF), as well. Low capacitance of the detector is very important (as discussed in chapter 3.5) for decreasing the noise, i.e., achieving high energy resolution, crucial for calibration measurements.

The referent  $^{241}\text{Am}$  gamma source radiates at 13.9 keV, 17.8 keV, 20.7 keV, 26.3 keV and 59.5 keV, with the last one being dominant [98]. The energy resolution that can be obtained by a diamond detector connected to A250 preamplifier is too low for resolving all the discrete peaks from the radioactive source. Therefore, we used a 0.29 mm thick copper shield around the radioactive source to reduce the number of discrete photon energies that can reach the detector. In that way only 26.3 keV and 59.5 keV gamma photons could pass through, while the lower energy X-ray photons were filtered out (the copper shield attenuates those energies more than 95%). The spectrum of shielded  $^{241}\text{Am}$  source was captured by both N1 diamond and a large NaI (Sodium Iodide) detector, with high detection efficiency for gammas. NaI is a large scintillating detector, which converts gamma photons to visible light. It was connected to ORTEC 276 photomultiplier and preamplifier module. Resulting spectrums are shown in figure 5.3 a) for NaI and b) for N1 detector.

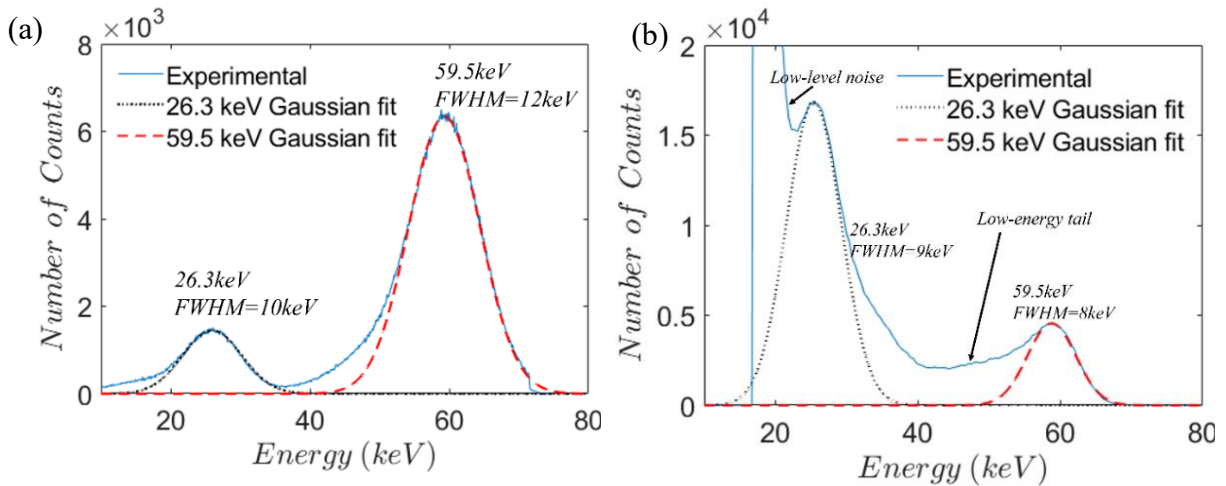


**Figure 5.3:** Spectrum of  $^{241}\text{Am}$  gamma source obtained by (a) NaI and (b) N1 diamond detector. [83] IEEE 2022. ©

Even though the radioactive source is the same, the two spectrums differ significantly. This is because different materials have different efficiencies in detecting gamma rays since the

probability of interaction of x-ray and gamma photons with the material is dependent on the number of atomic electrons, i.e. the atomic number. As mentioned, NaI has nearly 100% detection efficiency, while carbon, having low atomic number, is very inefficient at gamma detection. This is best seen from the fact that it took less than 30 seconds to obtain spectrum in fig 5.3 a) with two times more events than the spectrum in fig. 5.3 b), that took more than 23 hours to obtain. The efficiency of diamond is also a function of the energy of gamma photons, it decreases exponentially as the energy of the impinging photons increases. This is noticeable in the obtained spectrum with nearly three times more 26.3 keV photons detected compared to 59.5 keV ones, even though the emission probability of a 59.5 keV photon from  $^{241}\text{Am}$  is 35.9%, whereas it is only 2.4% for 26.3 keV one. However, NaI spectrum also has more events at 26.3 keV than it should. The reason for that is the contribution to the 26.3 keV peak by the iodine  $K\alpha$  escape line in NaI, which also has the energy of 26.3 keV, therefore it is indistinguishable from the  $^{241}\text{Am}$  26.3 keV photon. The energy resolution of N1 with A250 was  $8\pm 0.4$  keV, calculated as full width at half maximum (FWHM) of 59.5 keV peak. The energy resolution is quite good, even though the 26.3 keV peak is barely distinguishable from the low-level noise, because of the long measurement.

### 5.1.2 Characterization in planar mode

Measurements in planar mode should give us insight into overall characteristics of D11 diamond. The area probed with 400 keV protons was across the three top electrodes connected to the preamplifier input. Obtained IBIC map and histogram are shown in figure 5.4 a) and b), respectively. Since there is no nominal difference between the electrodes, we expected the IBIC map to have high CCE areas, representing the electrodes and low CCE areas, representing the gap between the electrodes, with all three electrodes having the same characteristics. However, this is not the case. As can be seen in fig. 5.4 a), the electrodes are distinguishable from the interstrip gaps by higher CCE, but there is significant difference between the electrodes themselves. The electrode in the top part of the map (close to the origin) has the highest CCE, while the electrode close to the bottom part of the map has the lowest, as if a triangular high CCE area was superimposed on the IBIC map. To try to better understand the data, we analyzed the histogram, fig. 5.4 b). In the histogram, three parts can be distinguished: a low energy, mid and high energy part, marked by a red, green, and black rectangle, respectively. We plotted the data corresponding to each peak in the separate IBIC maps, shown in fig. 5.4 c)-e), respectively. As can be seen from fig. 5.4 c), the lowest energy part of the histogram corresponds to the gaps

## Results and discussion

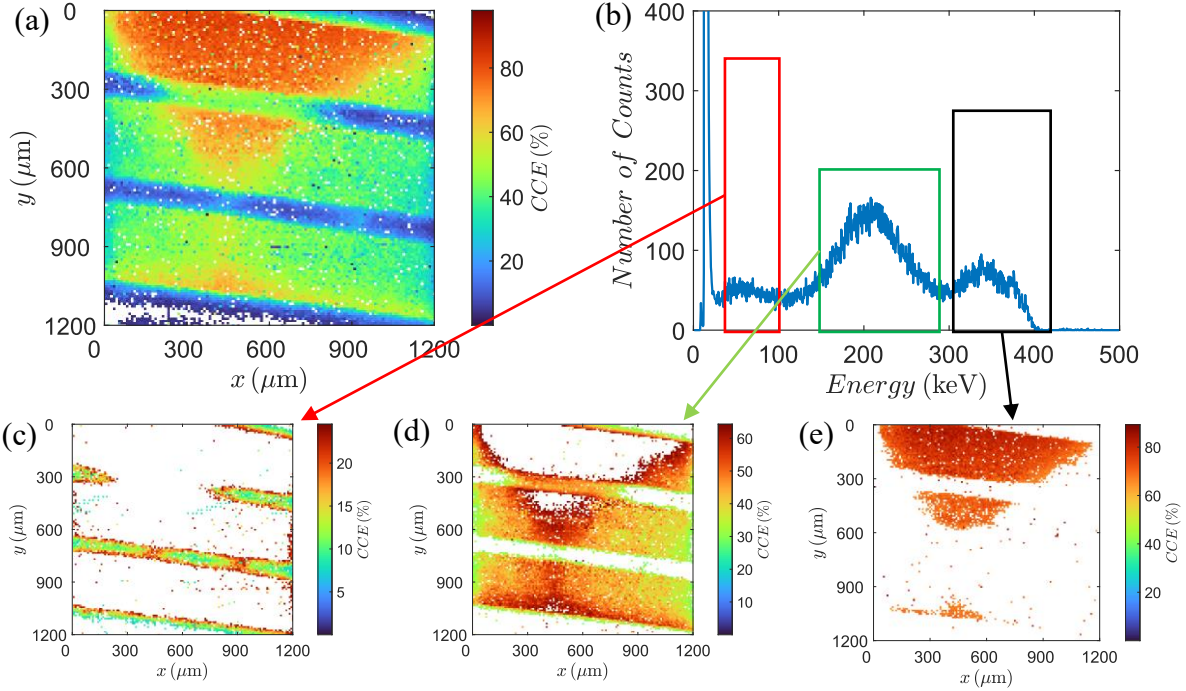


**Figure 5.4:** (a) IBIC map and (b) histogram obtained by D11 diamond and 400 keV proton beam in planar mode with biasing voltage of 100 V. (c) IBIC map of the events marked by a red rectangle in (b). (d) IBIC map of the events marked by a green rectangle in (b). (e) IBIC map of the events marked by a black rectangle in (b). In all IBIC maps the color white represents CCE=0%.

between the electrodes. The gaps have CCE of around 10%, but it increases to around 20% close to the edges of the electrodes. There is also an area with CCE of around 40% that can be seen in fig. 5.4 d) also represented as discontinuity in the interstrip gap, fig. 5.3 c), and it is a part of the high CCE triangular area. Figure 5.4 d) shows the events corresponding to the middle peak. Those events originate from areas under the electrodes. Since the electric field is created between the bottom electrode and the top three electrodes it is expected that part of the active volume of the detector located under the top electrodes is experiencing higher electric field (and in turn higher CCE) compared to the part of the detector volume located under the gaps, which implies only two distinct areas in IBIC maps. The fact that there are three distinct areas (marked in the histogram) implies that, due to the rectifying metal-diamond contact (as shown by the fig. 5.1), the electric field distribution within D11 diamond is much more complex than expected from the electrode layout. From the IBIC map it is clear that the CCE under the electrodes is not uniform. It varies between 80 %, fig. 5.4 e), in the high efficiency part to 30 %, at the outer borders of the IBIC map, fig. 5.4 d).

### 5.1.3 Characterization in interstrip mode

In the interstrip mode, D11 was connected so two top strips were used as a sensing and biasing electrode, fig. 4.2 a), while all other electrodes (including the bottom one) were floating. In that way the leakage current would be limited to the interstrip current only. The main advantage of this geometry is that the ions, implanted in the interstrip region, can be detected by drift of the induced EHP in the lateral electric field. The assumption was that for shallow ions the lateral electric field would be higher at the point of implantation compared to the electric field between the bottom and the top electrodes (longitudinal electric field).

The first ion beam used for detector characterization in the interstrip mode was 400 keV protons, the same ion beam used for the planar mode measurements. The IBIC map and histogram obtained by 400 keV protons in interstrip mode are shown in figure 5.5 a) and b),

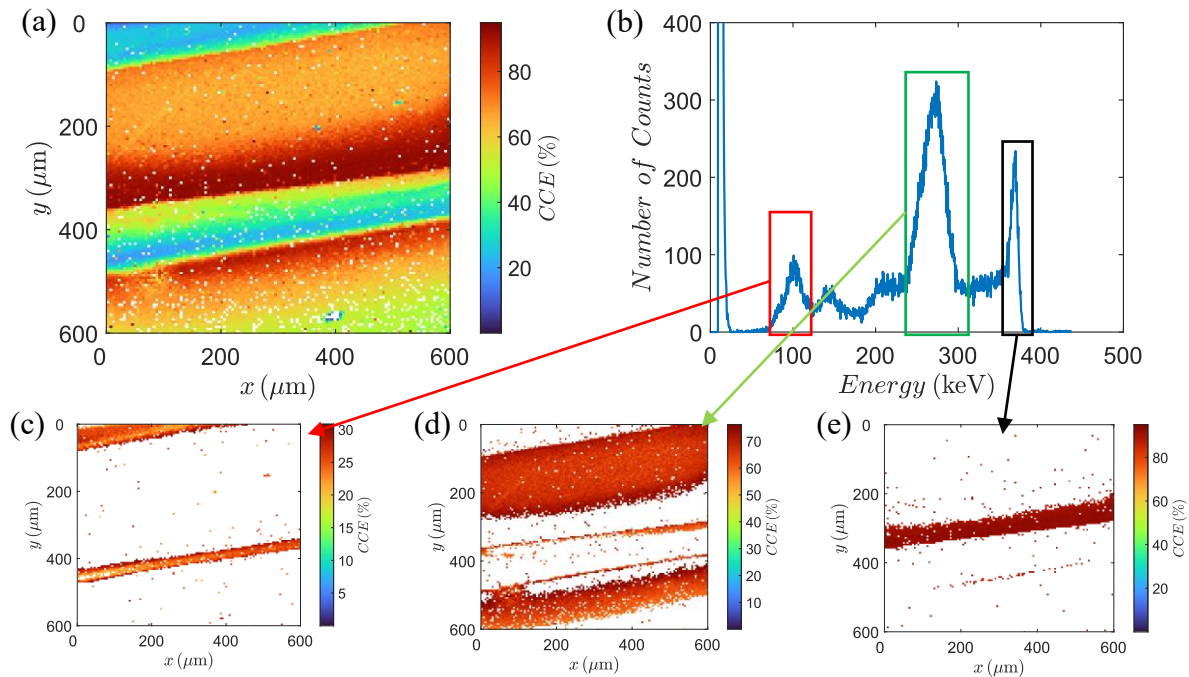


**Figure 5.5:** (a) IBIC map and (b) histogram obtained by D11 diamond and 400 keV proton beam in interstrip mode with biasing voltage of 97 V. (c) IBIC map of the events marked by a red rectangle in (b). (d) IBIC map of the events marked by a green rectangle in (b). (e) IBIC map of the events marked by a black rectangle in (b). In all IBIC maps the color white represents CCE=0%.

respectively. Compared to the previous measurements, the area of interest is four times smaller. The reason for reducing the area of interest was to obtain a more detailed IBIC map of the gap between the electrodes. In interstrip mode, the electrodes are clearly distinguishable from the gaps, same as in planar mode. The CCE isn't uniform, as well, but this was expected since the



## Results and discussion

electric field would be stronger at the edges of the electrodes, facing each other. Also, unlike in planar mode, the electrodes are not equivalent since one is connected to the biasing voltage and the other to the input of the preamplifier. In figure 5.5 a) the upper electrode (closer to the origin) is biasing electrode while to bottom one is sensing electrode. The sensing electrode has on average lower CCE than the biasing one, since the drift path of the free charge carriers created under the sensing electrode is shorter compared to the drift path of the free charge carriers created under biasing one. Therefore, charge created under the sensing electrode would induce lower signal, resulting in smaller CCE. Figure 5.5 b) shows the obtained histogram. Similar to 400 keV data, the histogram can be divided into low, mid and high energy areas (marked by red, green and black rectangles, respectively), with peaks more pronounced this time. Figure 5.5 c) shows events corresponding to the low energy peak and represent the gap between the electrodes. Figure 5.5 d) shows the areas under the electrodes themselves except for the parts close to the interstrip gap, areas of the highest CCE, shown in figure 5.5 e). All IBIC maps generated from the specific peaks of the histogram are more uniform in terms of the CCE range, compared to data obtained in planar mode. Fig. 5.5 d) clearly shows the edges of the electrodes. It can be noticed that the distance between the electrodes is not constant, that is, the edges are not perfectly straight and parallel. This might be the cause of the CCE fluctuation in the interstrip area. Comparing the CCE value between planar and interstrip mode, CCE is only slightly higher in the interstrip mode. However, the number of events with CCE larger than 80 % is more than an order of magnitude higher in interstrip than the planar mode. This is a direct consequence of the higher electric field seen by the free charge carriers created by the impinging ions.

The second ion beam used for detector characterization in interstrip mode was a 4 MeV proton beam. The IBIC map and histogram are shown in figure 5.6 a) and b), respectively. The 4 MeV protons penetrate deep in the crystal; therefore, we expect large areas of uniform CCE (consequence of uniform electric field). The IBIC map, fig. 5.6 a), shows two electrodes, with the sensing electrode being the upper one (closer to the origin). Biasing electrode has higher CCE than the sensing electrode, same as in case of 400 keV protons, however, CCE is more uniform in the maps obtained by 4 MeV protons. The gap between the electrodes also shows higher uniformity and CCE. Circular areas of low CCE at the left side of the IBIC map are due to the golden spheres created in the wire bonding process, which ions have to go through and lose a portion of their energy. Data histogram, shown in figure 5.6 b), shows three very sharp peaks, marked by red, green, and black rectangles. The events corresponding to the peaks are plotted as IBIC map in figures 5.6 c), d) and e), respectively. The low efficiency peak

## Results and discussion

corresponds to the events of low CCE outside the area of interest. The mid efficiency peak corresponds to the events under the sensing electrode that are not very close to the interstrip gap, and also to the area under the edge of the biasing electrode, far from the interstrip gap, as well. The high efficiency peak corresponds to most of the events under the biasing electrode and events under the part of the sensing electrode close to the interstrip gap, but not to the events in the gap itself. The events detected in the gap correspond to area between the peaks marked

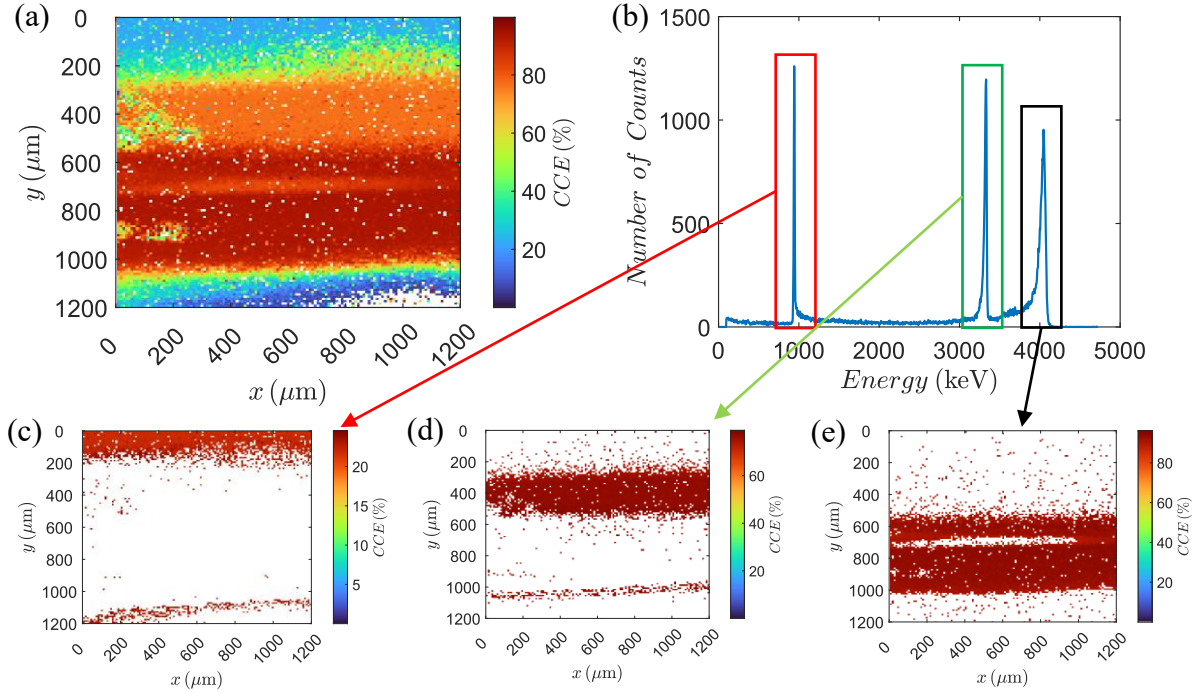


**Figure 5.6:** (a) IBIC map and (b) histogram obtained by D11 diamond and 4 MeV proton beam in interstrip mode with biasing voltage of 110 V. (c) IBIC map of the events marked by a red rectangle in (b). (d) IBIC map of the events marked by a green rectangle in (b). (e) IBIC map of the events marked by a black rectangle in (b). In all IBIC maps the color white represents CCE=0%.

by green and black rectangle in the data histogram. As expected, the CCE in the interstrip area is higher for 4 MeV than for 400 keV protons since the influence of the interstrip gap diminishes as the penetration depth increases. However, the highest recorded CCE differs by only a few percent between the two beams.

Measurements in planar mode revealed that, unfortunately, D11 sample has problems (varying distance between the top electrodes, unexpected triangular area of high CCE) that prevent effective deterministic single ion implantation. However, the measurements in interstrip mode led to several important conclusions. Introducing lateral electric field can result in higher CCE which is very important for detecting low energy ions. Comparing shallow and deep penetrating

## Results and discussion

beams showed that at low penetrating depths there will be areas with poor CCE uniformity, especially in the interstrip gap, the main implantation region. Besides the problems visible on the IBIC maps D11 sample suffered from one other issue. The normal detector response could be obtained only after several passes of the beam over the sample (several seconds of irradiation). This was noticeable both in planar and interstrip mode and both with 400 keV and 4 MeV proton beam. This effect is called priming [99] and in case of D11 originates from the Schottky barrier at the metal-semiconductor interface. Space charge at the interface can alter the electric field distribution locally, lowering the CCE. After the priming irradiation is done, the space charge is compensated by trapped charge carriers, resulting in stable electric field in the active volume of the detector. Priming can be considered as the opposite to polarization effect. In the case of deterministic ion implantation, the need to prime the sample is undesirable. Detection of a single shallow ion requires a uniform detector response across the whole implantation site and during the whole implantation process, which is very difficult to achieve if there is uncompensated space charge.

### 5.2 Diamond sample with top and bottom strip electrodes

In the second stage of measurements D12 sample was used together with several ion beams of different penetration depth. D12 was used in the interstrip mode, with two top strips acting as sensing and biasing electrode, as shown in figure 4.2 b), while all other electrodes were floating. The I-V characteristic, measured in the same configuration, is shown in figure 5.7. The I-V relation is mostly linear, with a slight change in slope above 100 V. The linearity implies ohmic characteristics of the detector, therefore, no priming effect is to be expected. Capacitance of the

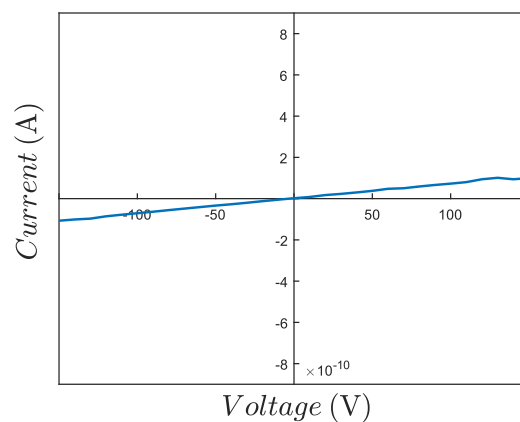


**Figure 5.7:** The I-V characteristics of D12 diamond in interstrip configuration.

sample was 0.4 pF, measured in the same configuration as I-V curves. Low capacitance enables the D12 diamond to be used together with XGLab CUBE PRE\_031 preamplifier so high energy resolution can be achieved. Both the diamond and the preamplifier were mounted on RBI Implantation Board v2.0. Since CUBE PRE\_031 preamplifier is of negative polarity (designed for collection of electrons in the detector) only negative biasing voltages were used.

### 5.2.1 Floating bottom electrodes

A total of four different ion beams were used: 1 MeV, 400 keV and 100 keV protons as well as 140 keV  $\text{Cu}^{2+}$  beam, each having different penetration depths. Using ion beams of different penetration depths enables us to investigate the influence of the diamond surface on the CCE by comparing the distribution of the electric field inside the active volume of the detector close to the surface and deeper in the bulk. Unlike with D11, we couldn't use N1 for calibration since the preamplifier is wire bonded to D12 diamond and once disconnected it can't be rebonded to another detector. Moreover, using  $^{241}\text{Am}$  referent gamma source with D12 would not result in distinct peaks which can be used for calibration, since the electric field distribution in D12 is not uniform. Therefore, the nominal gain of the preamplifier was used for calibration. Even though using nominal gain can result in some inaccuracy in the calibrated data, the gain of the CUBE PRE\_031, being a fully integrated device, is very well defined, compared to the gain of A250, a device made of discrete components.

Before the ion beam measurements, distribution of the electric field and potential within the active volume of the sample was simulated, in COMSOL Multiphysics [100]. During the measurements the sensing and bottom electrodes' potential was undefined: bottom electrodes were floating, and the sensing electrode was connected to the input of the preamplifier. However, for simulation purposes all electric potentials need to be defined. Therefore, the potential of the sensing electrode was set to 0 V and potential of the bottom electrodes was varied. Figure 5.8 a)-c) shows simulation of the electric field and potential distribution for bottom electrodes at -5 V, 0 V and 5 V, respectively. Figure 5.8 d) shows the simulation without bottom electrodes. The biasing voltage in all cases was set to -100 V. In reality the potential of the sensing electrode is different than zero, since the input transistor needs to be biased for the preamplifier to work properly, however, the influence of that potential is negligible to the electric field distribution within the crystal (given that the supply voltage for CUBE PRE\_031 is 5 V).

## Results and discussion

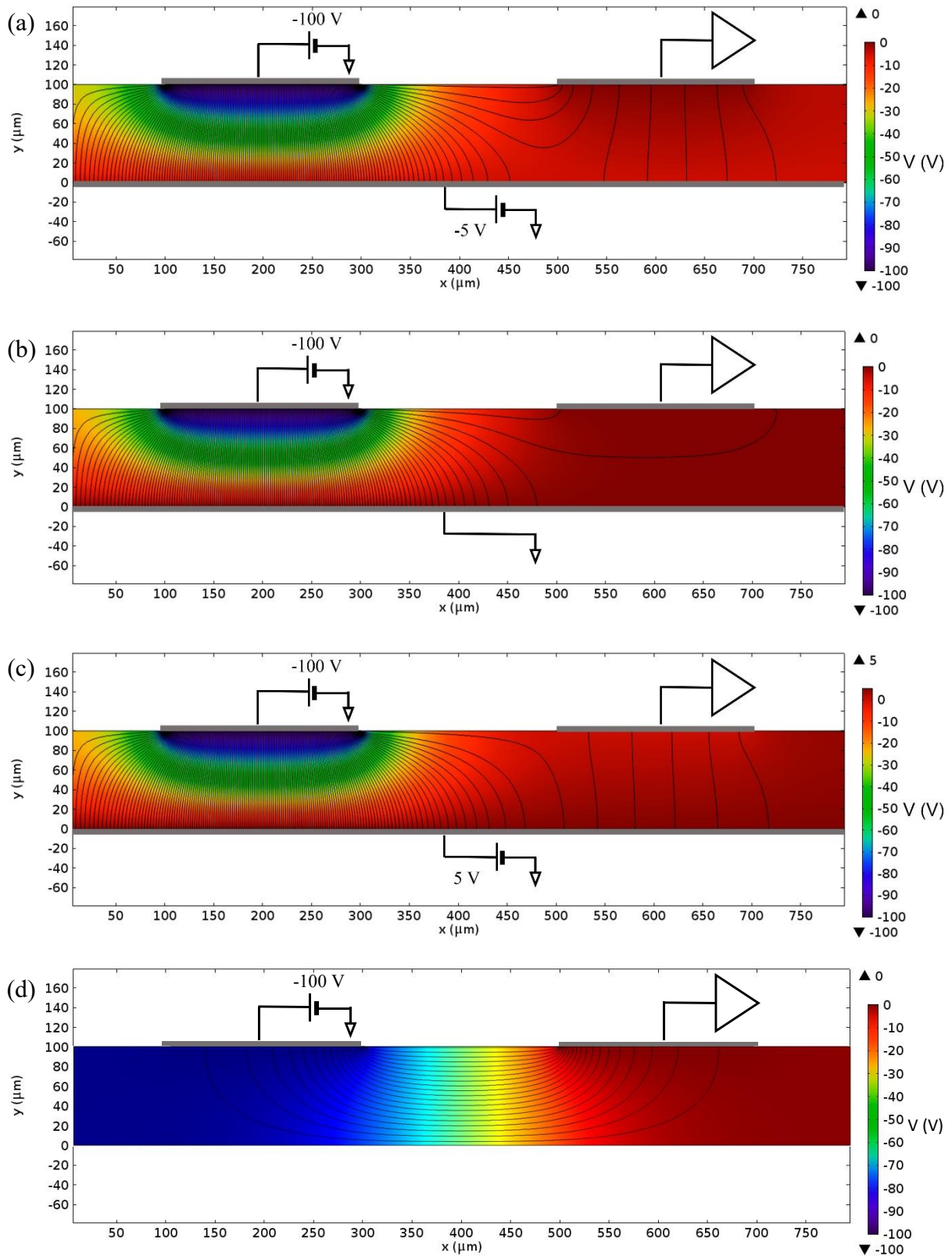


**Figure 5.8:** Simulation of electric field (magnitude proportional to line density) and potential (magnitude indicated by color) for an 800  $\mu\text{m}$  x 100  $\mu\text{m}$  D12 diamond cross section, containing bias, sensing and bottom electrodes, for bias electrode at -100 V and bottom electrode at (a) -5 V, (b) 0 V and (c) 5 V. (d) Simulation without bottom electrode. Electrodes (in gray) are not to scale. [83] IEEE 2022. ©

## Results and discussion

In all simulations the highest electric field is around the edges of the biasing electrode, except for the simulation without the bottom electrode where the highest field is around the edges of both biasing and sensing electrode and is symmetrical. We will focus on the electric field around the sensing electrode, since the charge induced on that electrode represents detector signal. In cases when there is a bottom electrode, electric field has local maxima around the edges of the sensing electrode (with higher field at the edge closer to the biasing electrode, except when the bottom electrode is positively biased). This is more prominent when the bottom electrode is negatively biased. Moreover, both vertical and horizontal components of the electric field under the sensing electrode are strongest in that case. Whereas grounded bottom electrode causes the weakest vertical component of the electric field under the sensing electrode and positive bottom electrode causes the weakest horizontal component. For high electric field directed towards the sensing electrode (similar to charge delivery detectors) high negative voltage is needed both at the bottom and at the biasing electrodes.

Figure 5.9 a) shows IBIC map obtained by D12 sample and 1 MeV proton beam. The edges of the top electrodes (indicated in the IBIC map by high CCE lines) are marked by the black lines,

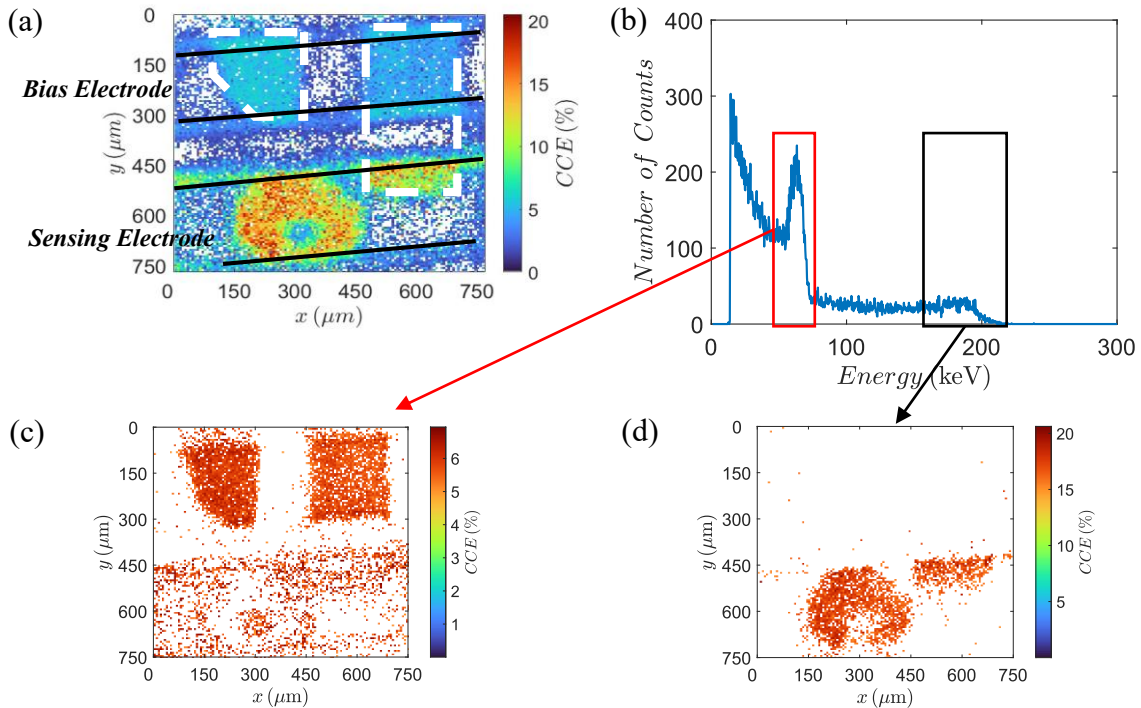


**Figure 5.9:** (a) IBIC map with top electrodes marked by black lines and bottom electrodes marked by white dashed lines. [83] (b) Histogram obtained by D12 diamond and 1 MeV proton beam in interstrip mode. (c) IBIC map of the events marked by a red rectangle in (b). (d) IBIC map of the events marked by a black rectangle in (b). In all IBIC maps the color white represents CCE=0%.

## Results and discussion

while the bottom electrodes are marked by white dashed lines. The CCE is high along the edges of both biasing and sensing electrodes, as the simulation predicted. Also, it is higher in the areas over the bottom electrodes compared to other areas with no bottom electrodes underneath, which, according to simulation, implies that the potential of the bottom electrodes is negative. However, sensing electrode exhibits higher CCE compared to the biasing one. From the data histogram, fig. 5.9 b), only two distinct peaks are visible: a low CCE and a high CCE peak, marked by red and black rectangles, respectively, with the low efficiency one being more prominent, and the high efficiency one having a long tail. Here the term high efficiency was used very loosely and doesn't imply that  $CCE = 20\%$  is considered high. It indicates that CCE of the peak marked by a black rectangle is higher (around three times) than the CCE of the peak marked by a red rectangle. The data corresponding to the two peaks is plotted in fig. 5.9 c) and d). From fig. 5.9 c) it is noticeable that the main contribution to the low CCE peak is from two areas located under the parts of the biasing electrode directly above the bottom electrode strips, with only small contribution from events located under the sensing electrode. High CCE peak corresponds to the events from the areas of highest CCE, under the sensing electrode and the long tail indicates wide amplitude distribution in the measured CCE. There are two distinct areas in fig. 5.9 d): a small, rectangular area, located above the bottom electrode strip; and a larger, donut shaped, area which seems to have no correlation to the bottom electrodes. While the higher CCE of the areas directly above bottom electrode strips have been explained by the possible negative potential of the bottom electrodes using the result from the simulation, the origin of the high CCE donut shaped area under the sensing electrode could be attributed to the variation in uniformity of the adhesive used to attach the diamond to the PCB [83], causing an ununiform electrical contact, since the existence of CCE enhancing localized impurities is highly unlikely. After the measurements the sample was removed from the PCB and subsequently reattached and rebonded and the high CCE donut shaped area disappeared, which confirms the statement that it originates from the adhesive non-uniformity. Having higher CCE under the sensing than under biasing electrode is in contradiction with the simulation results. The overall CCE is quite low – up to 20 %, which indicates incomplete collection and possible charge trapping. CCE is especially low in the interelectrode gap, down to 0 %. Charge trapping on impurities and imperfection in the diamond crystal, which shortens drift length, could explain higher CCE under the sensing electrode than under the biasing one. The larger the distance from the sensing electrode the larger is the chance of charge trapping, and if the charge is trapped before it reaches the sensing electrode then the signal it induces is smaller.

## Results and discussion

To obtain the energy resolution of the detector we used one of the two areas corresponding to the low efficiency peak, marked in figure 5.10 a) by a red dashed rectangle. Although low, the CCE of that area is very uniform, which is very important for accurate calculation of the energy resolution. A histogram representing data marked by a red rectangle in fig. 5.10 a) is shown in fig. 5.10 b). It shows a monoenergetic peak (blue) with a Gaussian fit (indicated by a red dashed line). The Gaussian curve has a mean at 72.5 keV and  $\text{FWHM} = 6 \pm 0.01 \text{ keV}$ , which represents the energy resolution of the detector.

In fig. 5.9 a) the position of black lines, representing the edges of the electrodes, was determined using simulation results. To test whether the measured data is in fact supporting this assumption the IBIC map was processed to obtain the average value of the CCE, projected on the axis perpendicular to the high CCE lines. In the first step the IBIC map is rotated so high CCE lines become parallel to the x-axis. Padding, in form of pixels with  $\text{CCE} = 0\%$  is added so the resulting map has the same number of pixels in each line (the resulting map is rectangular). The rotated IBIC map is sliced along the x-axis into 1D arrays of pixels, as shown in fig. 5.10 c), with each pixel within a single array having the same y coordinate. In the third step the average CCE is calculated for each line (array of pixels) using the formula:

$$\overline{\text{CCE}}(y) = \frac{\sum_{x=0}^n \text{CCE}(x,y)}{n} \quad (5.1)$$

Where n is the number of pixels in each pixel array. It is important to state that only pixels with nonzero value of CCE were used for averaging, to exclude the influence of the padding. By plotting the average CCE value for each of the 1D array of pixels of the rotated IBIC map, we get a projection of the average CCE on the axis perpendicular to the high CCE lines in the original IBIC map. [83] Projection of the average CCE in case of IBIC map obtained by 1 MeV proton beam is shown in figure 5.10 d). The shaded areas, representing position of electrodes, are added. Their position with respect to the average CCE peak was determined from the optical image of the electrodes and their dimensions. It is noticeable that the local maxima of the CCE are close to the edges of the electrodes, as predicted by simulation. The highest average CCE is at the edge of the sensing electrode that is facing the biasing electrode. Under the biasing electrode the average CCE is very uniform, whereas it shows a negative gradient under the sensing electrode.

The same procedure was applied to the IBIC maps obtained by 400 keV and 100 keV protons as well as 140 keV copper ions, shown in fig. 5.10 e), g) and i), respectively, while the resulting projections are shown in fig. 5.10 f), h) and j), respectively. Biasing voltage for all measurements was between  $-100 \text{ V}$  and  $-200 \text{ V}$ . Most of the free charge carriers are created



## Results and discussion

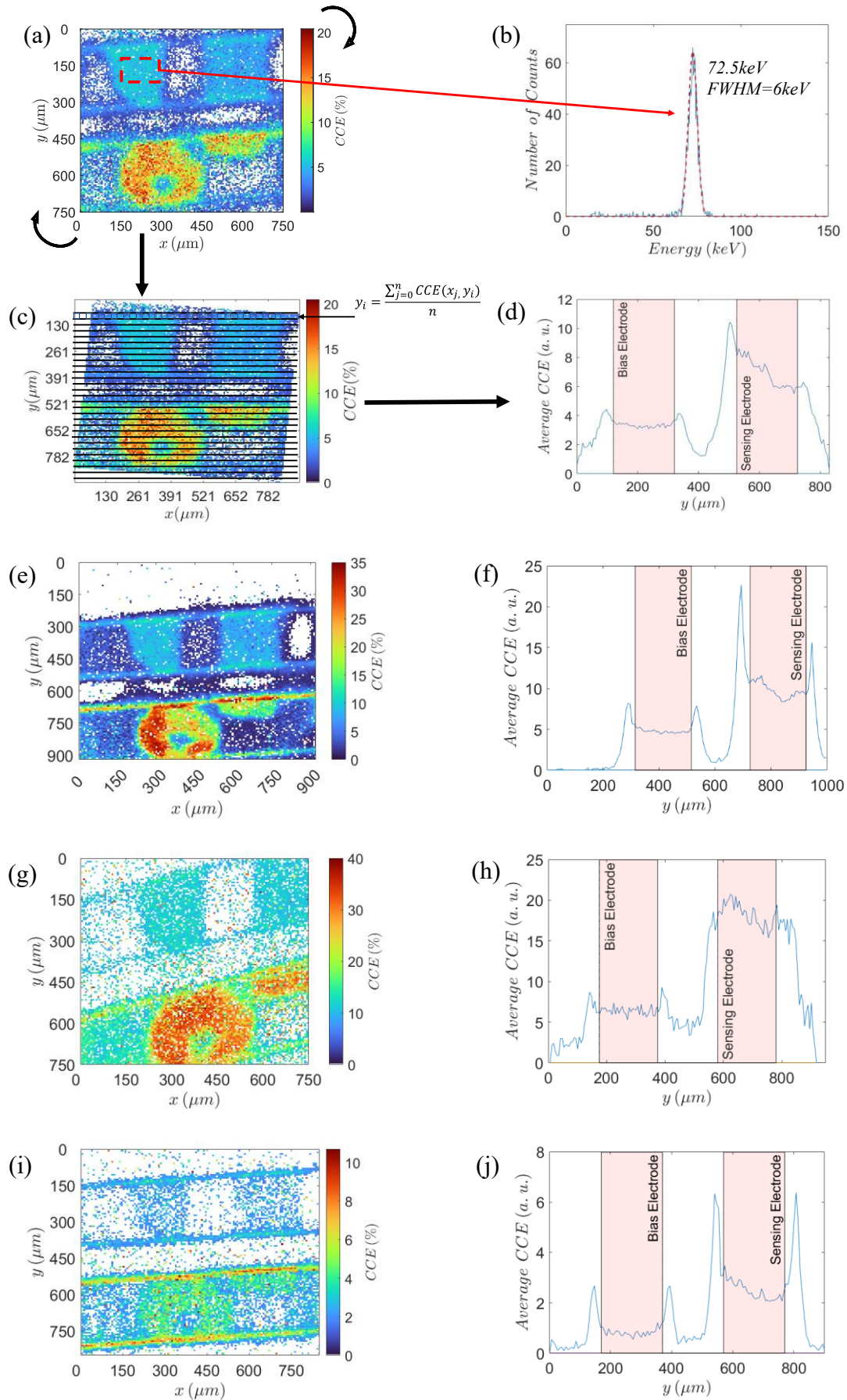


**Figure 5.10:** IBIC map obtained by irradiation of D12 diamond by (a) 1 MeV, (e) 400 keV, (g) 100 keV protons and (i) 140 keV copper ions. Solid black (dashed white) lines in (a) indicate top (bottom) electrodes' boundaries. (b) Monoenergetic peak (blue line) extracted from the area marked by red dashed square in (a), and Gaussian fit (red dashed line). (c) Rotated IBIC map, sliced into 1D pixel arrays (for each y value). The displayed equation is used for calculating the average CCE from the 1D pixel arrays. Average CCE, as a function of y coordinate with electrodes' position highlighted, calculated for (d) 1 MeV, (f) 400 keV, (h) 100 keV protons, and (j) 140 keV copper ions. [83] In all IBIC maps color white represents CCE=0%. IEEE 2022. ©

at the end of the range of the impinging ions [101]. Therefore, obtained IBIC maps represent electric field distribution at the depth defined by the penetration range of the ion beam. The range of the used ion beams differs significantly, which could have resulted in very different IBIC maps for each of the ion beams, even though they were scanned over the same part of the detector (similar to the results obtained by D11 sample). However, it is evident that all IBIC maps in fig. 5.10 show the same geometric features. The highest CCE areas are a donut shaped and rectangular area under the sensing electrode as well as high CCE lines along the edges of the sensing electrode are visible in all four maps. That indicates that D12 sample can successfully detect ions of different energies and down to 59 nm range (the penetration depth of 140 keV  $\text{Cu}^{2+}$  ions) without significant degradation of detection efficiency. However, the situation is quite different regarding the CCE between the IBIC maps. The highest value of CCE, overall, was recorded by using 100 keV protons, up to 40%. 100 keV protons aren't the deepest, nor the shallowest penetrating ion used therefore it is surprising that they result in the highest CCE. However, when comparing the CCE recorded for 1 MeV and 400 keV protons, it is noticeable that CCE increases as the penetration dept of the ions decreases. Since 100 keV protons have the smallest range of all the proton ion beams used, they would create free charge carriers closest to the electrodes. As seen from the simulation, free charge carriers experience stronger electric field closer to the electrode, which results in higher CCE. 140 keV copper ions have an even lower penetration range than 100 keV protons, therefore, free charge carriers created by 140 keV copper ions, should experience even higher electric field, resulting in higher CCE. However, this is not the case. CCE is much lower (nearly four times) for irradiation with 140 keV copper ions compared to CCE for 100 keV proton irradiation. Possible reasons can be effects of the diamond surface. Defects, acting as charge traps or recombination centers, close to the diamond surface can lower the CCE at low penetration depths. Negative electron affinity can result in diamond surface acting as electron sink [102], [103] causing free charge carriers created by a shallow beam (such as 140 keV copper) to decrease in number. We've already

## Results and discussion

mentioned polarization effect (chapter 3.2), which is more prominent for heavy ions. Another effect characteristic for heavy ions is pulse height defect. Pulse height defect refers to lower signal from the heavy ions due to nuclear energy loss, which is more significant for ions of lower energy and higher mass. Nuclear energy loss (energy loss due to collision with atomic nuclei, chapter 3.1) doesn't result in free charge carriers and is therefore considered to be non-ionizing process. Also, in semiconductor material heavy ions create dense cloud of free charge carriers (compared to lighter ions) resulting in recombination of some electrons and holes, shortly after their creation. Both described effects, characteristic for heavy ions, result in lower CCE [104]. However, given that CCE is not very high for protons, polarization and pulse height defect are probably not the main cause for low CCE obtained by irradiation with 140 keV copper ions. It is more realistic that, since most of the recorded signal originates from the events under the top electrodes, the energy loss in the electrode itself is the main cause for low CCE. Having penetration depth comparable to the thickness of the electrode (nominally electrode should be 100 nm thick, however, based on the recorded IBIC maps, the real thickness is probably closer to 50 nm) 140 keV copper ions lose significant portion of their energy during the passage through the electrode, resulting in on average lower CCE [83].

If we analyze the average CCE projections, figure 5.10 d), f), h) and j), we'll see that all except h), have global or local CCE maxima close to the edges of the electrodes. The exception being 100 keV protons with only local maxima at the edges of the biasing electrode. In their case the maximum CCE is under the sensing electrode, because of their penetration depth which, as mentioned, causes EHP created under the sensing electrode to be swept by a strong electric field. The most prominent average CCE peaks are obtained for 140 keV copper ions, fig. 5.10 j). The same figure best illustrates the influence of the electrode on the CCE, as the average CCE under the sensing electrode is around half of the CCE at the edge of the sensing electrode. This indicates that only half of the energy dissipated by 140 keV copper ions is deposited in the area directly under the electrodes, while the rest is lost in the interaction with electrode material. 140 keV copper ion represents the extreme case of the electrode influence (because of the very small penetration depth) indicating that deterministic single ion implantation shouldn't rely on implantation through the electrode metallization. The optimal implantation area, in this specific case, should be along the electrode edges, coinciding with the high CCE lines, where signal resulting from each impinging ion would be highest.

## 5.2.2 Biased bottom electrodes

The optimal implantation area of D12 sample is quite small for fabrication of large quantum devices and CCE is very low limiting the energy of the impinging ions. Therefore, another experiment was conducted, with biasing voltage both at the biasing and at the bottom electrodes. Moreover, the preamplifier was cooled, to decrease the noise, thus increasing the energy resolution. It should be stated that in this experiment the cooling system described in chapter 4.5 wasn't used (at this stage of measurements it hadn't been constructed yet). A simpler system based on a cold finger cooled by liquid nitrogen and a ceramic heatsink was used instead. The temperature of the heatsink was  $-15^{\circ}\text{C}$  and the PCB was at  $-5^{\circ}\text{C}$ . The poor cooling performance was due to poor thermal conductivity of FR4 (material used for PCB fabrication), and poor efficiency of the cold finger in heat transfer. The ion beam used was 400 keV protons, and the biasing voltage was  $-200\text{ V}$  at the biasing and  $-100\text{ V}$  at the bottom electrode. The obtained IBIC map and data histogram corresponding to the events marked by a red rectangle on the IBIC map are shown in figure 5.11 a) and b), respectively.

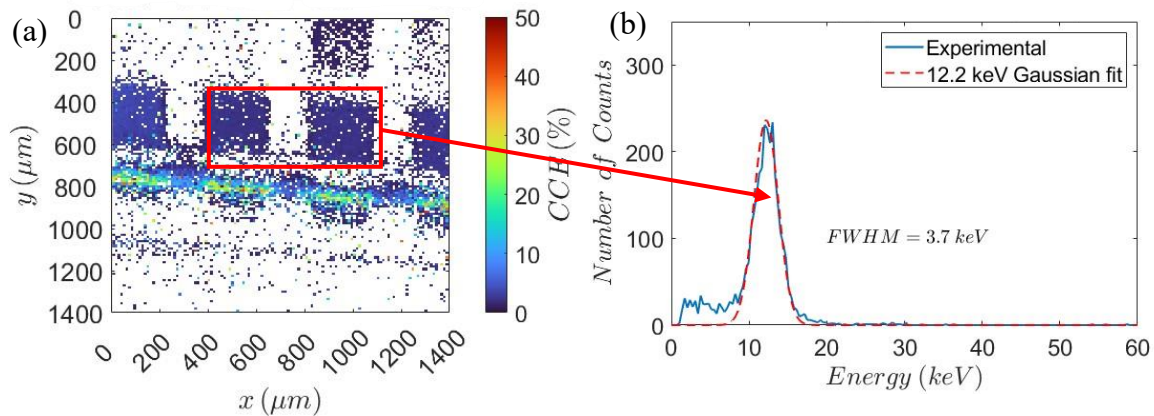


**Figure 5.11:** (a) IBIC map and (b) histogram obtained by D12 diamond and 400 keV proton at  $-5^{\circ}\text{C}$ . Biasing electrode was at  $-200\text{ V}$  while the bottom electrodes were at  $-100\text{ V}$ . In (a) color white represents  $\text{CCE}=0\%$ .

From the IBIC map we can distinguish two main areas: large, rectangular areas of low but uniform CCE, representing events directly above the bottom electrodes; and a long and narrow area of higher but not uniform CCE, representing the gap between two top electrodes. Unlike in the IBIC maps in figure 5.10, there are almost no events under the sensing electrode. Also, there are significantly more events in the interstrip gap, also the maximum CCE is 50%, compared to 35% in fig. 5.10 e). This is due to the different electric field distribution, a direct

consequence of the biasing voltage at the bottom electrode. The map at fig. 5.11 a) represents an area almost two times larger than maps in figure 5.10, another reason why some of the smaller features can't be clearly seen. Two large areas of uniform low CCE were used to obtain a monoenergetic peak, fig. 5.11 b), which was used for calculating the energy resolution. By fitting a Gaussian curve to the peak with mean at 12.2 keV, the energy resolution was calculated to be  $3.7 \pm 0.01$  keV, nearly two times better result compared to the energy resolution at room temperature and without biasing voltage at the bottom electrodes. The cooling could cause improvement in achieved energy resolution, but it can't result in increased CCE. Therefore, the main contribution to the increase in performance of the detector is contributed by the negative bias of the bottom electrodes. The extraction of a 12.2 keV peak with SNR=3.3 (fully separated from the low-level noise), in combination with successful detection of 140 keV copper ions, penetrating on average only 59 nm, confirms that D12 sample is a good starting point for design of a diamond detector with capability to detect low energy single ions with high detection efficiency and CCE. Moreover, applying the biasing voltage to the bottom electrodes increased the area of higher CCE that acts as an implantation suite, an important step towards a detector designed for fabrication of large quantum devices. However, the implantation suite in case of D12 is still small and more importantly its CCE is far from uniform. Therefore, an improved electrode layout, which would provide large areas of uniform (and preferably high) CCE acting as implantation sites, is needed.

### **5.3 Diamond sample with circular implantation sites**

In the third stage of measurements, D13 sample was used together with protons and copper ions. As shown in figure 4.2 c), D13 has several implantation sites of different sizes and geometry, which can be divided into two groups: circular and rectangular implantation sites. The circular sites are realized as holes in the sensing electrode with biasing voltage connected to the bottom electrode, creating quasi longitudinal electric field. The rectangular sites are parts of a meandering gap between the sensing and the top surface biasing electrode. There are several rectangular sites of different surface areas. In common for all of them is that beside the longitudinal electric field (created by the biasing voltage of the bottom electrode) a lateral electric field component (created by the biasing voltage of top surface biasing electrode) can be introduced. In the initial characterization of the detector 100 keV and 400 keV protons were used. The main advantages in using protons as a probing beam are: 1. Low energy protons cause negligible damage to diamond crystal so they can be used for probing the CCE without

## Results and discussion

performance degradation; 2. 100 keV and 400 keV protons pass through the electrode but stop in the diamond substrate so full energy peak can be recorded with high CCE. [96] 140 keV  $\text{Cu}^{2+}$  ions were used with D13 as shallow probing beam, so the results can be compared to the results obtained by D12 sample.

As with the previous samples, I-V measurements were performed before experiments with ion beams, to determine the leakage current of the diamond sample. Figure 5.12 a) and b) show I-V curves for planar configuration of D13 sample (leakage current between the sensing and the bottom electrode). The characteristic is linear, which indicated ohmic behavior of the sample, although it is not symmetrical. The slope of the leakage current is higher for negative biasing voltages, compared to the positive ones, however, the difference is small. At  $-250$  V, the maximum voltage used with D13, the leakage current is below  $0.1$  nA, as can be expected for the high purity diamond crystal. D13 sample was mounted on RBI Implantation Board v2.2 and connected to CUBE PRE\_031 preamplifier. The initial capacitance of the sensing electrode was  $2.5$  pF, which is too high for CUBE PRE\_031, designed for sub  $0.5$  pF detectors. The resulting SNR was very poor so D13 had to be modified. After splitting the sensing electrode, fig. 4.3, the capacitance of the resulting sensing electrode was  $0.6$  pF, low enough for a functioning detector.

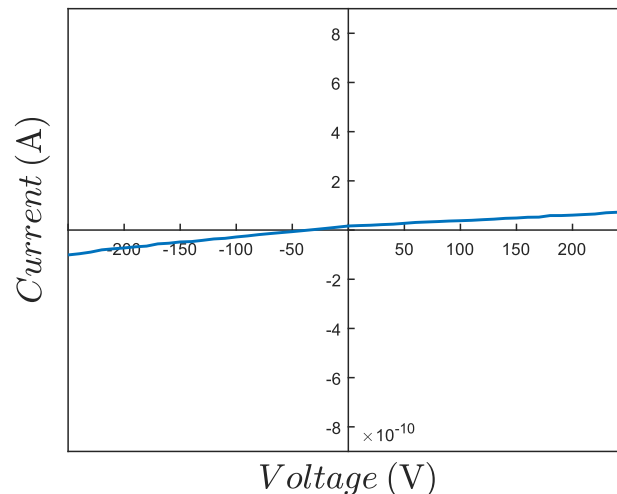


**Figure 5.12:** The I-V characteristics of D13 diamond.

### 5.3.1 Calibration of CUBE PRE\_031

Since D13 was the most advanced detector used in this research, the results needed to be calibrated for a more accurate calculation of CCE and estimation of the minimum detectable

energy. Direct calibration of D13 with a referent gamma source couldn't be performed, for the same reasons outlined in case of D11 sample. Due to the electrode geometry and small thickness of D13, irradiation wouldn't result in distinct peaks in data histogram. Therefore, same as with D11, we used N1 and  $^{241}\text{Am}$  gamma source for energy calibration. However, CUBE PRE\_031 can't be detached from one detector and attached to another, as was the case with A250. Therefore, we mounted N1 on another RBI Implantation board v2.2 and connected it to another CUBE PRE\_031. To make sure that the performance, in terms of gain of the preamplifier and influence of the PCB on the signal propagation, of the calibration setup is as close as possible to the setup with D13, both the preamplifier and the PCB used with N1 were from the same production lot as those used with D13. Figure 5.13 shows  $^{241}\text{Am}$  gamma spectrum obtained by N1 diamond. Unlike in the case of D11 calibration, there was no filter between the radioactive source and the detector, so low energy X-rays could be recorded, as well as the gammas. The

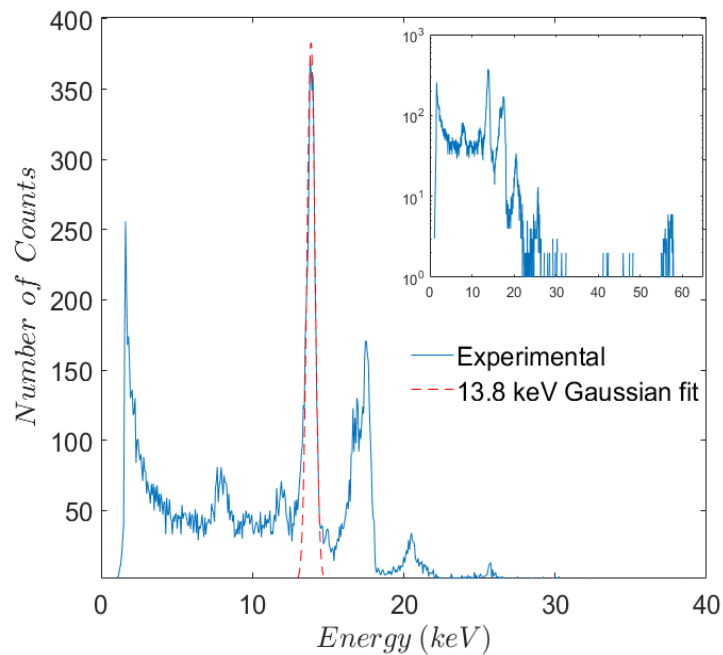


**Figure 5.13:** Histogram obtained from a referent  $^{241}\text{Am}$  gamma source by N1 diamond detector. Main figure shows histogram for energies between 0 and 40 keV, in linear scale. Full histogram in semilogarithmic scale shown as snippet. Gaussian fit for a 13.8 keV peak is shown by red, dashed curve. [96] The biasing voltage was  $-250\text{ V}$ .

histogram shows peaks at 13.8 keV, 17.7 keV, 20.7 keV, 26.3 keV and 59.5 keV, characteristic for  $^{241}\text{Am}$ . As discussed in section 5.1.1 emission at 59.5 keV (dominant emission) results in peak two orders of magnitude smaller than the 13.8 keV and 17.7 keV peaks, as a consequence of diamond's poor detection efficiency of higher energy photons. To determine the energy resolution of the detector/preamplifier system, a Gaussian fit was made to 13.8 keV peak in fig.

5.13. The energy resolution was  $0.63 \pm 0.06$  keV, or 48 electrons ENC, the best result so far. The energy calibration of CUBE preamplifier obtained by N1 sample was used to check the energy calibration for D12, done by using nominal gain of the preamplifier. The results obtained by D12 showed good agreement with the referent results obtained by N1.

The very good energy resolution of N1 diamond with CUBE PRE\_031 preamplifier implies that low-level noise, which limits the minimum detectable energy, should be low. However, this couldn't be confirmed from fig. 5.13 because of the Compton continuum, which overlaps with the low-level noise. There are ways to suppress the Compton continuum by pulse shape analysis [105]. However, we decided to use a 5.9 keV gamma from  $^{55}\text{Fe}$  as a reference for the minimum detectable energy. Figure 5.14 shows the spectrum obtained by N1 sample after being exposed to  $^{55}\text{Fe}$ . Data histogram shows a single peak fully separated from low-level noise. There is also a low energy tail that overlaps with low-level noise, but not significantly. This confirms that the minimum detectable energy is quite low, i.e., a diamond detector with low enough capacitance of the sensing electrode, connected to a CUBE PRE\_031 preamplifier should have no problem detecting 5.9 keV (or even lower energy), given that the electric field in the active volume of the detector is high enough.

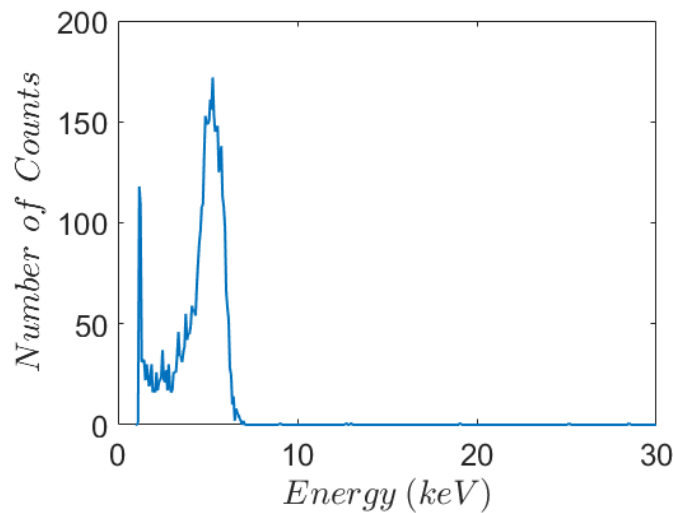


**Figure 5.14:** Histogram obtained from a referent  $^{55}\text{Fe}$  gamma source by N1 diamond detector. The biasing voltage was  $-250$  V.

### 5.3.2 Characterization without lateral electric field

The first ion beam used for characterization of D13 was 100 keV protons. That specific ion beam was chosen since it resulted in the highest CCE in the case of D12 sample. Figure 5.15



shows the results obtained by 100 keV proton irradiation of the largest (50  $\mu\text{m}$  diameter) circular implantation site of D13. The IBIC map is shown in fig. 5.15 a) together with a circle indicating the position of the implantation site itself. Even though the value of CCE goes up to 100 %, there is no clear boundary between the electrode and the hole. Also, CCE falls below 20 % towards the center of the hole. The data histogram, shown in fig. 5. 15. b), shows one well defined peak together with several broader areas. The peak represents events originating under the electrode. However, the most interesting part of the spectrum is the small high efficiency area, marked by a red rectangle in fig. 5.15 b). Those events are mainly aligned with the edge of the electrode, as shown in fig. 5.15 c).

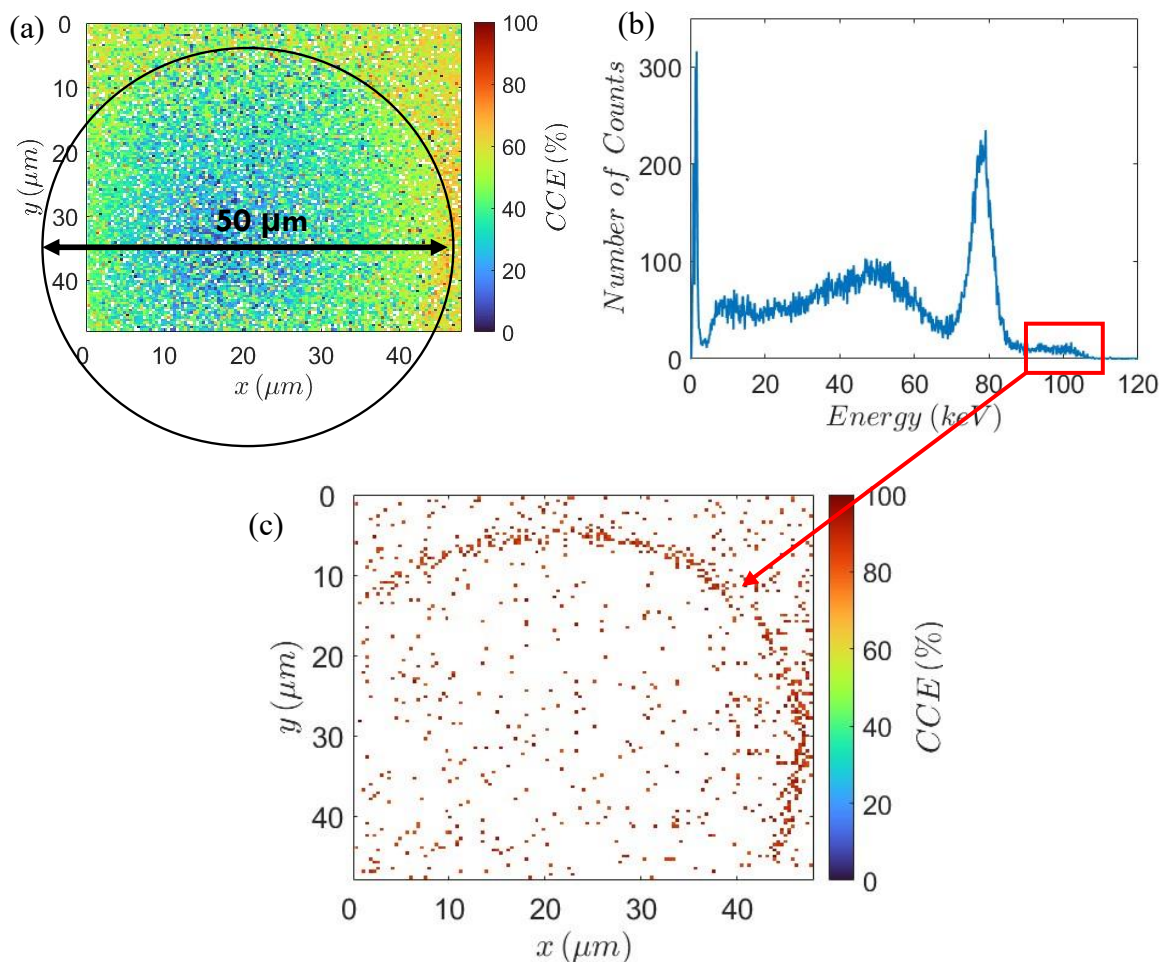


**Figure 5.15:** (a) IBIC map and (b) histogram obtained by irradiation with 100 keV protons over a part of the 50  $\mu\text{m}$  implantation site of D13 diamond. Black circle in (a) represents the edge of the implantation site. (c) IBIC map of the events marked by a red rectangle in (a). In all IBIC maps the color white represents CCE=0%. The biasing voltage was  $-200$  V, applied on the bottom electrode.

This is expected since the same high CCE lines are recorded by D12 and also predicted by the simulation. In comparison to D12, the maximum CCE obtained by D13 with 100 keV protons

## Results and discussion

is 2.5 times higher. D13 is thinner so the electric field can be very strong across the active volume, which is probably the main reason for the increase in the maximum CCE. The total of three implantation sites were characterized by 400 keV protons: one 50  $\mu\text{m}$ , one 30  $\mu\text{m}$  and one 10  $\mu\text{m}$  hole. The biasing voltage on the bottom electrode was set to  $-150\text{ V}$  in all the measurements with 400 keV protons, because that voltage was high enough for achieving 100% CCE. The irradiation area was the same for all three implantation sites:  $25 \times 25\ \mu\text{m}^2$ . This enables 100 % CCE (full efficiency) peak to be recorded alongside the signals for 30  $\mu\text{m}$  and 10  $\mu\text{m}$  implantation sites, since their area is smaller compared to the irradiation area. The difference in size between the sites is significant and we believe that having the same irradiation area for all three sites would enable a more accurate comparison of the obtained histograms. For the same reason, the biasing voltage was the same, as well, in all three cases. Figure 5.16 a) and b) show CCE maps for 50  $\mu\text{m}$  and 10  $\mu\text{m}$  implantation sites, respectively, while fig. 5.16 c)-e) show histograms for 50  $\mu\text{m}$ , 30  $\mu\text{m}$  and 10  $\mu\text{m}$  sites, respectively. [96] For both IBIC maps the CCE color bar has range over 100 %, however, the electric field is far too small for avalanche or charge multiplication to occur. Events with CCE higher than 100 % are a consequence of pileup (explained in chapter 3.4) and are also visible in corresponding histograms (fig 5.16 c) and e)) as small peaks of energies above the full efficiency peak. The full efficiency (CCE=100 %) peak is visible in all three histograms, even though the area of 50  $\mu\text{m}$  implantation site is larger than the irradiation area. After thorough analysis of the data, we determined that the existence of a full efficiency peak in fig. 5.16 c) is a consequence of the beam halo. The beam halo represents the part of the ion beam scattered from the main beam path (by collisions with neutral particles inside the vacuum tubes, by different beam focusing or steering elements...). Those ions can end up on the sample surface inducing signal in positions different from the main beam position. It is an undesirable effect that can be suppressed by several techniques, such as introducing one or more sets of slits that block scattered ions. However, in this case beam halo has a useful effect since it enables a full efficiency peak to be displayed in the data histogram for 50  $\mu\text{m}$  implantation site. It is important to state that in the case of all three implantation sites, the halo events don't alter the recorded spectrum in a significant way. The number of halo events is very small in comparison to the total number of events, in all three cases: less than 2 % of the total number of detected events in case of the 50  $\mu\text{m}$  and 30  $\mu\text{m}$  implantation sites and less than 1 % of the full efficiency peak for the 10  $\mu\text{m}$  one. When analyzing the histograms obtained for different implantation sites, we can distinguish in each of them a full efficiency peak and a broad collection of signals (very wide peak) of lower efficiency. That broader areas represent events from the implantation sites.

## Results and discussion

As can be seen, the larger the implantation site, the wider the signal collection from the site itself will be. Moreover, the centroid of the broad peak moves towards the lower efficiencies as the area of the implantation site increases. For 50  $\mu\text{m}$  implantation site the broad peak is very wide ( $>250$  keV), with centroid around 260 keV, and fully separated from the full efficiency peak. In case of 30  $\mu\text{m}$  site the broad peak is narrower ( $\sim 200$  keV), with centroid around 340 keV and it overlaps slightly with the full efficiency peak. Whereas the broad peak can be easily resolved in case of 30  $\mu\text{m}$  implantation site, for the smallest site the overlap between two peaks is so significant that the peak corresponding to signals from the implantation site cannot be resolved from the full efficiency peak. Its centroid is probably around 360 keV, 100 keV higher than for the largest implantation site. Its width can't be accurately estimated since it is only present as a 150 keV wide tail to the full efficiency peak. Due to both highest charge collection efficiency (indicated by the highest energy of the centroid of the broad peak) and

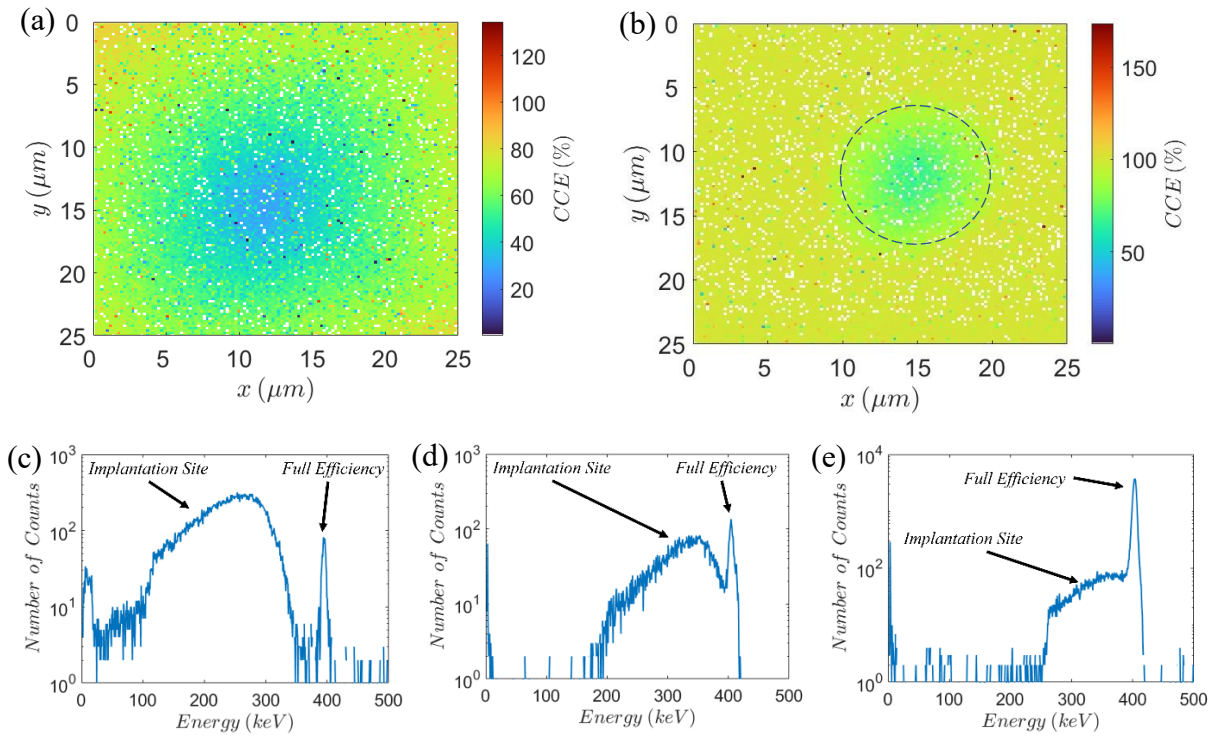


**Figure 5.16:** CCE distribution and histograms of different implantation sites. CCE map of (a) 50  $\mu\text{m}$  and (b) 10  $\mu\text{m}$  implantation site. Dashed line in (b) represents the edge of the hole in the sensing electrode. Histograms for (c) 50  $\mu\text{m}$  (corresponding to CCE map in (a)), (d) 30  $\mu\text{m}$  and (e) 10  $\mu\text{m}$  (corresponding to CCE map in (b)) implantation site. The biasing voltage on the bottom electrode was set to  $-150$  V in all cases. In (c)-(e) two distinct parts of spectrum were marked: one corresponding to signals originating from the implantation site (CCE  $< 100$  %); and the full efficiency peak, originating from area outside the implantation site (where CCE = 100 %). Signals higher than full efficiency peak, corresponding to CCE  $> 100$  % are pileup events. For (a) and (b) color white was hard coded for CCE = 0%. [96]

## Results and discussion

narrowest CCE distribution (indicated by the smallest width of the broad peak), ions implanted in the smallest implantation site would have the highest probability of detection. However, having the best detecting capabilities comes at the cost of having the smallest area, therefore the smallest number of ions that can be implanted in the 10  $\mu\text{m}$  implantation site. The energy resolution of D13 extracted from the 400 keV protons irradiation data was  $1.15 \pm 0.08$  keV, which compared to  $0.63 \pm 0.06$  keV achieved by N1, is 83 % worse result. Both diamonds are mounted on the same kind of PCB and connected to the same kind of preamplifier. Moreover, both diamonds are of the same purity, and the electric field across D13 is much higher than across N1, since D13 is an order of magnitude thinner. The main difference between the two samples and the cause for the better energy resolution of N1 is the capacitance, namely N1 has three times lower capacitance than D13. Also, the capacitance of D13 is slightly higher than optimal for CUBE PRE\_031 preamplifier. This result confirms that capacitance of the detector i.e., the sensing electrode, is crucial for low noise applications.

After the characterization with protons, 140 keV copper ions were used to record low depth CCE for all three implantation sites. Figure 5.17 a) shows a photograph with all three sites visible, while b) and c) show IBIC maps for 50  $\mu\text{m}$  and 30  $\mu\text{m}$ , and 10  $\mu\text{m}$  site, respectively. The biasing voltage on the bottom electrode was  $-250$  V, in both irradiation measurements. From both IBIC maps it is evident that 140 keV copper ions can't penetrate the electrode, therefore, only signals from the implantation sites were recorded. For that reason, the effect of beam halo is significantly smaller than in the case of 400 keV protons irradiation. Since scattered ions can't penetrate the electrode and the beam halo spans outside the irradiation area, the chance for a scattered ion to hit an implantation site is rather small. Given that for 400 keV protons irradiation halo events were under 2 % of the total number of detected events, the halo events in the case of 140 keV copper ions irradiation are negligible. Figure 5.17 b) shows that the difference in CCE uniformity between the 50  $\mu\text{m}$  and 30  $\mu\text{m}$  sites is even larger than in case of 400 keV proton detection. While CCE decreases towards the middle for both sites, there is a large area of CCE=0 % in case of the 50  $\mu\text{m}$  implantation site. Areas with CCE=0 % are called dead zones since they represent parts of the detectors' active volume in which no signal is detected from the impinging ions. In case of 50  $\mu\text{m}$  implantation site the dead zone is large, having diameter of around 10  $\mu\text{m}$ , and almost the same area as the smallest implantation site. The average CCE in the areas close to the edge of the electrode was between 10 % and 15 % for both sites. Figure 5.17 c) shows the IBIC map of the smallest implantation site. The reason to record the IBIC map of the smallest implantation site separately is a simple one: to get a more detailed map since the resolution of the IBIC map in fig. 5.17 b) wasn't high enough to

show all the details of the 10  $\mu\text{m}$  implantation site. The IBIC map of the smallest implantation site shows that most of the area of the site has CCE of around 15 % while only the middle of the site, a circular area with a diameter of around 2  $\mu\text{m}$  has CCE below 10 %. Therefore, the ions implanted close to the center of the hole induce a much lower signal than those implanted close to the edges.

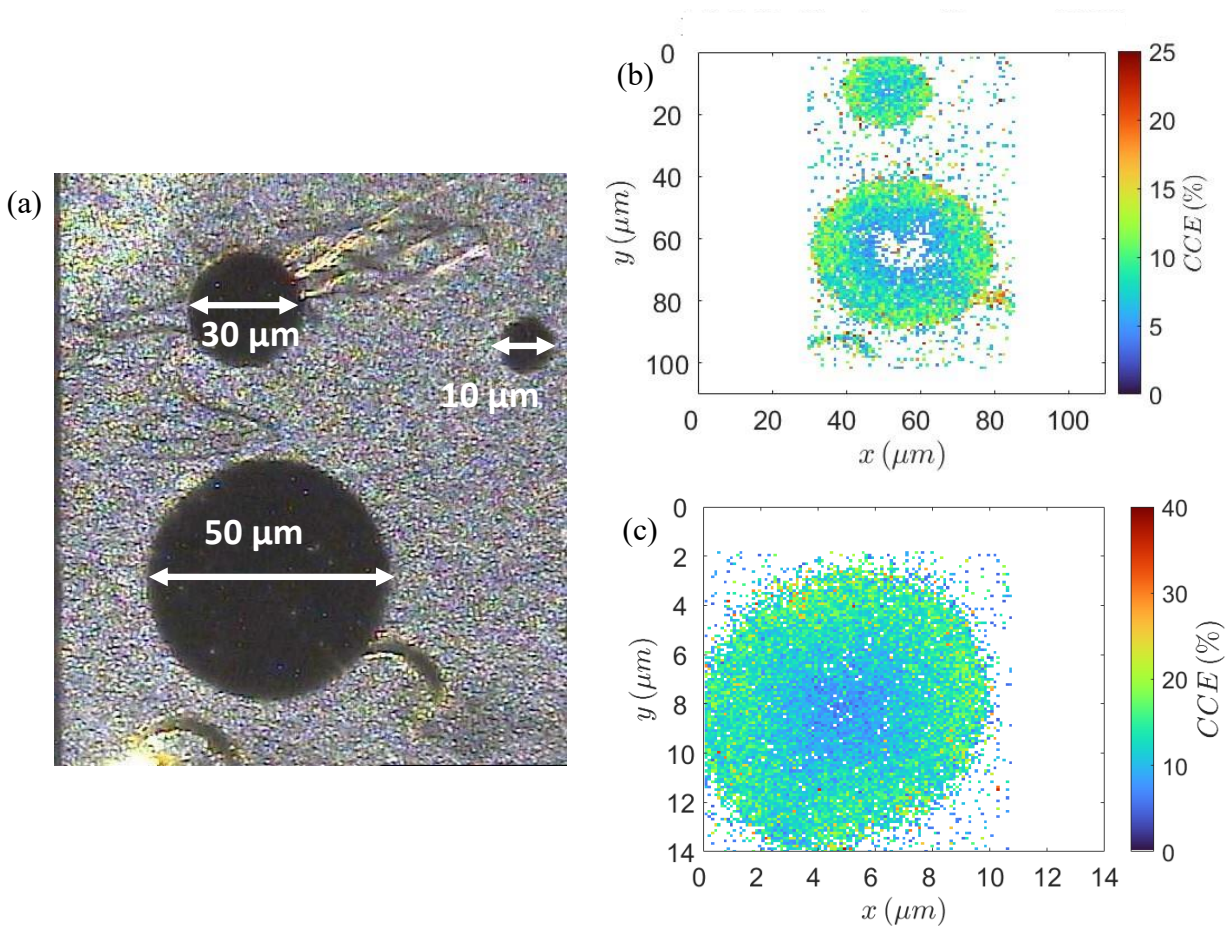


**Figure 5.17:** (a) Photograph of all three kinds of circular implantation sites. (b) IBIC map of a 50  $\mu\text{m}$  and 30  $\mu\text{m}$  implantation sites. (c) IBIC map of a 10  $\mu\text{m}$  implantation site. The biasing voltage on the bottom electrode was -250 V. For (b) and (c) color white was hard coded for CCE = 0%.

Results obtained by 140 keV copper ion are very similar to those obtained by 400 keV protons, both show that smaller area implantation sites have higher and more uniform CCE. Moreover, compared to the results obtained by D12 sample and 140 keV copper ions D13 sample shows significant progress both in uniformity and magnitude of the CCE. The peak CCE for D12 diamond was around 10 % while the average CCE for the 10  $\mu\text{m}$  implantation site is twice that value (if we exclude the low CCE area in the middle of the site). While this is a big improvement, 20 % is still quite far from the desired 100 % CCE for shallow ion detection.

### 5.3.3 Characterization with lateral electric field

To try to improve the uniformity of the CCE for shallow ions, across the whole implantation area, the region between the A strip of the top biasing electrode and B strip of the sensing electrode, fig. 4.2 c), was used. The two strips create a rectangular  $80 \times 10 \mu\text{m}^2$  implantation site, between them, also referred as the interstrip region. The existence of the bottom electrode under the interstrip region enables the electric field to have only longitudinal component (only bottom electrode is biased) or both longitudinal and lateral components (both bottom and top biasing electrodes are biased). By introducing a lateral component of the electric field, we hope to increase both magnitude and uniformity of CCE. For this irradiation measurements 140 keV copper beam was used, so the results obtained with the interstrip region can be directly compared to the results obtained by circular implantation sites. Figure 5.18 a) and b) show IBIC maps of the interstrip region obtained by 140 keV  $\text{Cu}^{2+}$  irradiation with top biasing electrode at 0 V and  $-180$  V, respectively. By comparing the IBIC maps of the same region, obtained by the same ion beam while varying only the voltage of the top biasing electrode, the influence of the lateral electric field can be studied. The obtained results were then compared to the CCE distribution of a  $10 \mu\text{m}$  circular implantation site (hole). That specific hole was chosen as a reference since it has the best CCE uniformity of all the circular implantation sites. Moreover, its diameter is the same as the distance between the strips of the interstrip region. [96]

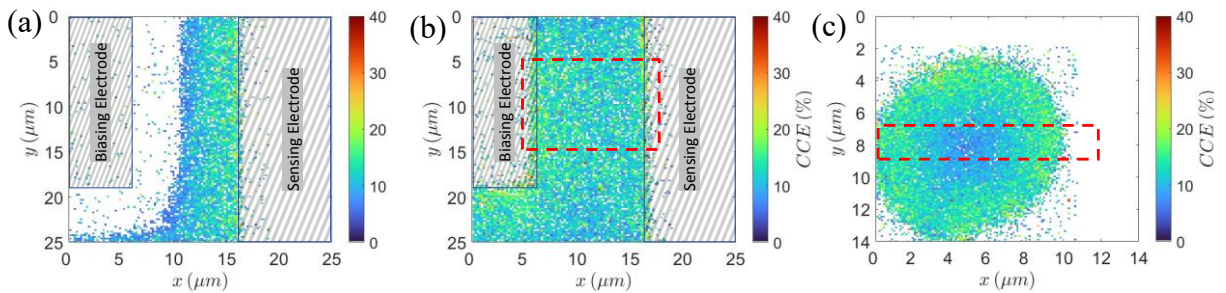


**Figure 5.18:** CCE distribution maps obtained by 140 keV copper ions. (a) Interstrip region for biasing electrode at 0 V; (b) interstrip region for biasing electrode at  $-180$  V; (c)  $10 \mu\text{m}$  implantation site. Voltage on the bottom biasing electrode was  $-250$  V in all three measurements. Color white was hard coded for CCE = 0%. [96]

There is a large dead zone in the IBIC map, when the top biasing electrode is at 0 V, fig. 5.18 a). It spans from the middle of the implantation site to the biasing electrode, occupying approximately half of the implantation site. The CCE of the other half increases from around

## Results and discussion

5 % in the middle of the site to 20 % close to the edge of the sensing electrode. With lateral electric field, fig. 5.18 b), the dead zone disappears. In that case the CCE is highest around biasing and sensing electrodes (around 20 %), with high CCE areas being wider, close to the biasing electrode. Towards the middle of the implantation site the CCE gradually drops, reaching the minimum of around 10 % past the middle point, closer to the sensing electrode. To better understand the origin of the dead zone, the simulation of the electric potential and field distribution for case of interstrip region and 10  $\mu\text{m}$  hole was made, using COMSOL Multiphysics. Figure 5.19 a)-c) show simulated distribution of the electric field and potential for interstrip region without the lateral electric field, with the lateral electric field, and for the 10  $\mu\text{m}$  hole, respectively. For this simulation, same as for simulation of D12 sample, the sensing

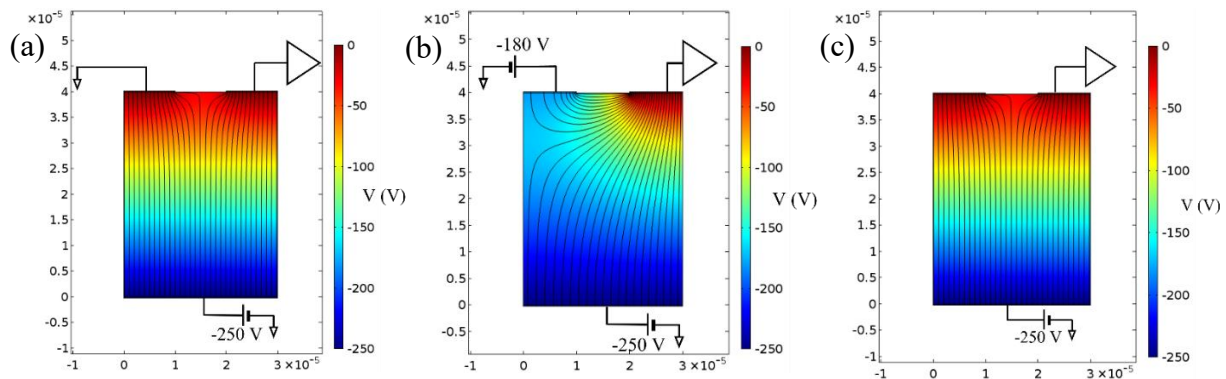


**Figure 5.19:** Electric potential (magnitude indicated by color) and field (magnitude proportional to line density) simulation. (a) Interstrip region for biasing electrode at 0 V; (b) Interstrip region for biasing electrode at  $-180$  V; (c) 10  $\mu\text{m}$  hole. x and y axis are in meters. [96]

electrode was assumed to be at ground potential. In the case of the interstrip region without the lateral field, fig. 5.19 a), the field lines diverge around the middle of the implantation site. Therefore, the free charge carriers that are created close to the sensing electrode would drift towards that electrode inducing a measurable signal, while the free charge carriers created closer to the bias electrode would drift towards it (away from the sensing electrode) inducing negligible signal in the sensing electrode. [96] If we compare the simulation results for interstrip region without the lateral electric field and for 10  $\mu\text{m}$  hole, we'll see that distribution of both electric field and potential are the same. This is because the distance between the strips is 10  $\mu\text{m}$ , the same as the diameter of the circular implantation site. However, there is no dead zone in the IBIC map of 10  $\mu\text{m}$  hole. This is because in the case of a circular implantation site, the sensing electrode is all around the hole, so the free charge carriers always drift towards it, inducing a measurable signal. For interstrip region with the lateral electric field, fig. 5.17 b),

the electric field close to the diamond surface is uniform and directed towards the sensing electrode. The simulation results describe the measurements very well and explain the existence of dead zone for interstrip region without the lateral electric field. They also indicate that CCE should be more uniform in case of interstrip region with lateral electric field than for a  $10\ \mu\text{m}$  circular implantation site, which seems to be the case according to the IBIC maps of the two sites. To check whether this really is the case the magnitude of the CCE across the interstrip implantation site, with the lateral electric field, and the  $10\ \mu\text{m}$  hole was compared. The graph in figure 5.20 shows the pointwise average CCE in the region indicated by the red dashed rectangle in fig. 5.18 b) and c), respectively. [96] The region of interest is positioned across the center of the implantation site in both cases, with dimensions  $10\ \mu\text{m} \times 12\ \mu\text{m}$  for the interstrip region, and  $2\ \mu\text{m} \times 12\ \mu\text{m}$  for the  $10\ \mu\text{m}$  hole. Due to difference in size of the IBIC maps, and therefore different number of data points, for the two implantation sites padding (in form of leading and trailing zeros) had to be added to the corresponding datasets so the overlay of the two regions of interest could be displayed correctly (one over the other). Adding leading and trailing zeros to a dataset doesn't alter the data itself, but only shifts it left or right on the graph. This shift was needed in case of  $10\ \mu\text{m}$  site since the edge of the site is aligned with the edge of the IBIC map.

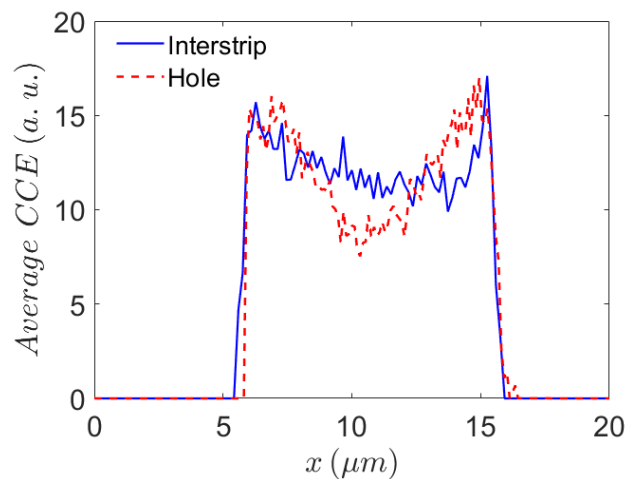


**Figure 5.20:** Pointwise average CCE for interstrip implantation site and  $10\ \mu\text{m}$  hole regions marked by a red dashed rectangle in fig. 5.18 b) and c), respectively. Padding (leading and trailing zeros) was added to the datasets so they can be overlaid correctly. [96]

Figure 5.20 shows that the biggest difference in recorded CCE is around the middle of the hole, where interstrip region has around 70 % higher charge collection efficiency than  $10\ \mu\text{m}$  hole, even though the circular site has slightly higher average CCE close to the electrode. While both



## Results and discussion

implantation sites demonstrate 100 % detection efficiency (each implanted ion is successfully detected), compared to 10  $\mu\text{m}$  circular implantation site, interstrip region has more uniform CCE overall, even though it has an order of magnitude larger area. The demonstrated detection efficiency is recorded for protons as well as for 140 keV copper ions. However, the same efficiency is expected to be achieved for detection of other ion species with penetration depth higher or equal to the penetration depth of 140 keV Cu ions. There are several such ion species that can be used for creation of quantum centers diamond: 170 keV Ge, 90 keV Si, 65 keV Mg and 50 keV N, all having penetration depth of around 60 nm. Different ion species with the same penetration depth have different energies, which means they create different number of EHP upon implantation, inducing the signal of different amplitude on detector electrodes. For that reason, it is useful to calculate the detection limit of the system i.e., the minimum detectable energy. We've already demonstrated, with N1 sample, successful detection of 5.9 keV gamma line from  $^{55}\text{Fe}$ . However, gamma photons travel much further into the material before being absorbed than ions. Therefore, the gamma measurement doesn't include the effects of decreasing CCE as the penetration depth gets smaller. Detection limit that includes this effect can be written as:

$$\frac{E_{Ion}}{E_{EHP}} \cdot CCE > 3 e_{in} \quad (5.2)$$

Where  $E_{Ion}$  is the energy of the impinging ion,  $E_{EHP}$  is the energy needed to create one EHP in diamond,  $CCE$  is charge collection efficiency and  $e_{in}$  is equivalent noise charge at the input of the preamplifier in number of electrons (noise figure of the detector/preamplifier system). [96] For high fidelity measurements the signal should be separated from the low-level noise in data histogram by  $6\sigma$  (six standard deviations). This ensures that overlap of events representing detected ions and those originating from noise happens in only 0.15 % of the total recorded events. The separation is calculated between the amplitude of the signal (mean of the Gaussian fit) and the average noise level (for low noise, this corresponds to 0 keV). Since we measure energy resolution by measuring FWHM of monoenergetic peaks in data histograms and  $\text{FWHM} \approx 2.355 \sigma$ , the six-sigma criterion translates to 2.55 FWHM. In inequality 5.2 we rounded that up to 3 FWHM i.e.,  $3 e_{in}$  to get a more conservative estimate of the lowest detectable energy. Since left side of the inequality 5.2 represents the signal measured by the detector, the whole expression can be written in terms of (SNR) as:  $\text{SNR} > 3$ . By taking into account noise contribution of the preamplifier and shaping amplifier, as well as the gain they provide, the minimum detectable energy becomes  $18.7 \pm 0.2$  keV for low capacitance detectors, such as N1, or  $34.1 \pm 0.3$  keV for detectors with higher capacitance, such as D13. In this

calculation CCE was assumed to be 10 %, even though interstrip implantation site has CCE > 10 % over the whole area. Calculated minimum detectable energy values show that D13 sample connected to CUBE PRE\_031 preamplifier should have no problem detecting 50 keV N, as well as other ion species of interest: 170 keV Ge, 90 keV Si, 65 keV Mg. Potentially, the presented detector/preamplifier system could successfully detect ions of lower energy (and penetration depth), expected to result in even lower CCE, which would in turn increase the minimum detectable energy. However, it is very difficult to predict the absolute limit, in terms of the ion species of minimum energy and penetration depth that the system could detect, because the decrease of CCE with the penetration depth is not linear but depends on the electric field distribution. Moreover, at very low penetration depths the charge loss due to the negative electron affinity of diamond surface would decrease CCE significantly, limiting the minimum detectable energy.

The size of the interstrip region ( $800 \mu\text{m}^2$ ) is sufficient to accommodate more than  $2 \times 10^5$  implanted 50 keV nitrogen ions. Each of the implanted ions can create an NV center upon activation, resulting in up to  $2 \times 10^5$  qubits or quantum centers used for sensing. Here we assumed that all possible stationary positions of each implanted ion lie within a cylinder with base centered at the point of implantation and diameter of 62 nm, equal to the longitudinal range of the ions. The lateral range of lighter ions (such as nitrogen) is smaller compared to their longitudinal range; therefore, our assumption guarantees that each ion would stop within the defined volume. When calculating the possible number of implants the distance between two implantation points on the crystal surface was set to 62 nm, to ensure no possible overlapping of the final position of implanted ions. The same number of possible quantum centers could be created by implantation of any other ion species mentioned in the previous paragraph, since all have nearly identical penetration range.

### 5.3.4 Characterization at low temperature

Though results obtained by D13 are promising, indicating that deterministic single ion implantation of low energy nitrogen ions should be possible at room temperature, we decided to try lowering the noise and increase the energy resolution even more. To do that, we used the cooling system described in chapter 4.5 to lower the thermal noise, and in turn, hopefully the overall noise of the detector/preamplifier system. As mentioned in chapter 3.3, thermal noise is present in all resistive material, meaning that both the diamond crystal and the preamplifier

contribute to this type of noise. However, their contribution is not equal. Diamond, being a wide bandgap semiconductor, has very low concentration of free charge carriers at room, and even at high temperatures. This results in high resistivity of pure diamond. On the other hand, the preamplifier is a silicon device, with the concentration of free charge carriers at room temperature many orders of magnitude higher, thus with much lower resistivity. In semiconductor devices such as detectors or amplifiers, thermal noise is manifested as parallel current noise, inversely proportional to the resistivity. Therefore, the contribution of diamond crystal to the overall thermal noise of the detector/preamplifier system is significantly smaller than the contribution of the preamplifier. Nevertheless, in the low temperature measurements both the diamond and the preamplifier were cooled since both were mounted on the same PCB. The contribution to the overall noise figure by other parts of the signal processing system, namely shaping amplifier and ADC are much lower than the contributions of the detector itself and the preamplifier, as discussed in chapter 3.5, therefore thermal noise of those devices can be neglected.

The best overall results, regarding noise, were achieved by N1 sample, during calibration measurements with  $^{241}\text{Am}$  referent gamma source. To assess the influence of low temperature on the noise figure of the detector/preamplifier system, we repeated those measurements at  $-47^\circ\text{C}$ . Figure 5.21 a) and b) shows spectrums obtained by N1 sample exposed to  $^{241}\text{Am}$  gamma source at room temperature and at  $-47^\circ\text{C}$ , respectively. The two histograms look nearly

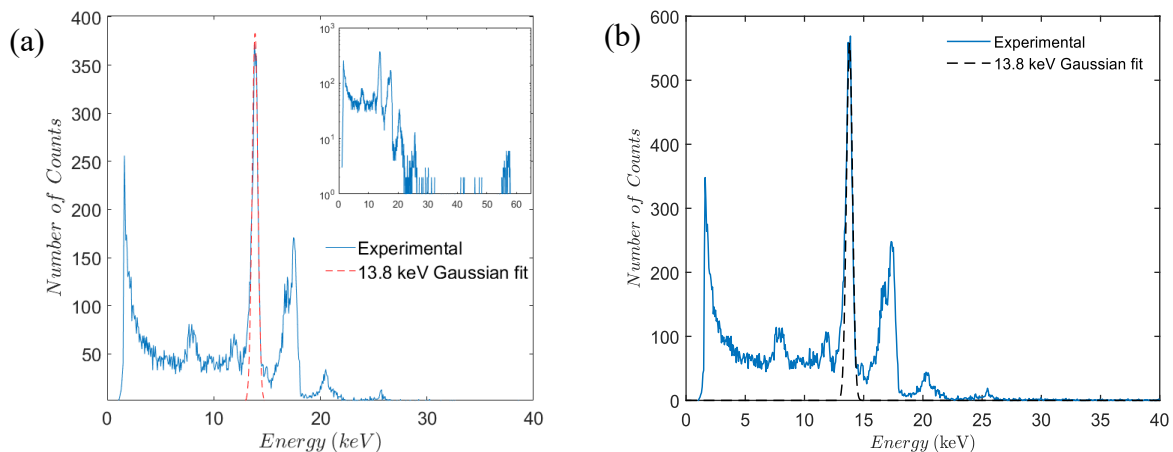


**Figure 5.21:**  $^{241}\text{Am}$  gamma spectrum obtained by N1 sample at: (a) room temperature [96] and (b)  $-47^\circ\text{C}$ .

## Results and discussion

the same, with differences being only the result of statistics – the low temperature spectrum having more detected events. Gaussian fit was made to a 13.8 keV peak in both spectrums resulting in FWHM of  $0.63 \pm 0.06$  keV at room and  $0.6 \pm 0.06$  keV at low temperature. The difference of 0.03 keV between the low and the room temperature measurements is far too small (lower than the uncertainty of the fit) to be attributed to the decrease in thermal noise. By lowering the temperature of the preamplifier by 70°C thermal noise decreases significantly. The fact that there is no significant decrease in the overall noise of the system indicates that thermal fluctuations in the velocity of charge carriers are not the predominant source of noise. The most probable source of noise in our system is interference from the surroundings. The  $\mu$ Probe end station is equipped with a beam scanner and several vacuum pumps, all inducing unwanted signal through both grounding and power lines. Sensitive electronics shares those lines with the digital part of the data acquisition system, whose current spikes can be noticed in the recorded signal if proper filters are not used. Even with using filters for power voltages of the preamplifier, and providing low impedance return path for both signal and power currents, it seems that interference still finds its way to the recorded signal. Supporting this is the fact that best results were achieved for shaping (peaking) time of 6  $\mu$ s, while for the lowest noise of the preamplifier the shaping time of 1  $\mu$ s is recommended by the manufacturer. In the attempt to reduce the interference, we used batteries to power the preamplifier; however, no improvement was achieved, indicating that the main noise path is through grounding of the chamber.

## 6 Conclusion

The aim of this work is to show that deterministic single ion implantation into diamond substrate can be achieved using commercially available crystals, and ion beam induced charge detection as an implantation verification technique. Three of the four samples were used for assembling prototype detectors, with features, such as thickness and electrode layout, designed to test the charge collection at different depths in the crystal, while providing high signal to noise ratio. Two main parameters of interest which have been studied in each experiment were charge collection efficiency and noise. The first one needed to be maximized while the second needed to be as low as possible. This was critical for detection of low energy, shallow penetrating ions, preferred for fabrication of quantum devices due to their low lateral straggling, enabling high density, deterministic implantation.

Although all the samples were single crystal electronic grade CVD diamonds, the highest purity available, not all of them had satisfactory characteristics as detectors. Diode like behavior, high leakage current and priming effect of D11 limited the performance of this sample significantly, essentially disqualifying it from being a candidate for low energy ion implantation. Nevertheless, the results obtained by D11 showed variation of CCE with the penetration depth, which set a benchmark for subsequent D12 sample and diamond detectors which rely on interstrip detection, in general. D12 sample showed that areas directly above bottom electrodes had higher CCE compared to the areas with no bottom electrodes underneath. This was confirmed with four different ion beams: 1 MeV, 400 keV, 100 keV protons and 140 keV copper ions, with penetration range of 8.1  $\mu\text{m}$ , 2.1  $\mu\text{m}$ , 0.44  $\mu\text{m}$  and 59 nm in diamond, respectively. The last being the least penetrating ion beam obtainable in the accelerator facility of Ruđer Bošković Institute. Successful detection of 140 keV copper ions represents the first major step towards deterministic implantation of shallow ions since their penetration depth is very similar to that of 50 keV nitrogen ions, the preferred ion species for creation of NV centers.

## Conclusion

Besides the excellent electric properties (low leakage current, no priming and low polarization), the key to D12 performance, was in using XGLab CUBE PRE\_031 low noise preamplifier (used for all measurements with D12 and D13) and RBI Implantation Board v2.0, the carrier PCB of both D12 and CUBE PRE\_031. High gain and low noise of the detector/preamplifier system enabled D12 to achieve the energy resolution of 6 keV at room temperature, with floating bottom electrodes. By applying biasing voltage to the bottom electrode and cooling the preamplifier down to  $-5^{\circ}\text{C}$ , energy resolution was improved to 3.7 keV. Unfortunately, D12 had a very low CCE for 140 keV copper ions ( $< 10\%$ ), and even for protons it wasn't higher than 50%. However, a far bigger problem with D12 was detection efficiency of the interstrip region. Whereas detection efficiency of areas under the top strip electrodes (especially under the sensing electrode) was good, detection efficiency in the interstrip region was very poor (large parts having detection efficiency of 0%), limiting the implantation site size to narrow areas close to the electrodes. For a successful deterministic single ion implantation, detection efficiency of 100% is needed, across the whole implantation area. D13 sample was designed specifically to address this issue. It demonstrated 100% detection efficiency for protons in case of 50  $\mu\text{m}$ , 30  $\mu\text{m}$  and 10  $\mu\text{m}$  circular implantation sites, while achieving up to 100% CCE. For 140 keV Cu ions detection efficiency was lower than 100%, only for 50  $\mu\text{m}$  implantation site. However, the CCE was low, on average around 20% close to the edge electrodes, and decreasing towards the middle of the sites, with the smallest site being the most uniform. Even though this is a significant improvement over D12 performance, the non-uniformity of CCE is undesirable for fabrication of quantum devices since it limits the minimum detectable energy of the system, whereas if the area of the implantation site is reduced for a more uniform CCE, the size of the quantum device that can be fabricated is reduced as well. To overcome this limitation a lateral electric field was used together with longitudinal field to enhance the CCE of 800  $\mu\text{m}^2$  implantation site created by two strip electrodes. The resulting uniformity of CCE was higher compared to that of 10  $\mu\text{m}$  circular site, even though the area of the interstrip region is an order of magnitude larger compared to 10  $\mu\text{m}$  hole. The energy resolution of D13 was 1.15 keV, while the minimum detectable energy was calculated to be 18.7 keV, taking into account the decrease of CCE at low penetration depth. Both values suggest that there should be no problem in detecting each 50 keV N ion across the whole implantation site. The best energy resolution, however, was demonstrated by N1 sample, a planar diamond detector. Its output was calibrated by a  $^{241}\text{Am}$  referent gamma source, resulting in 0.63 keV FWHM of the 13.8 keV peak, and successfully detected 5.9 keV gamma rays radiated by  $^{55}\text{Fe}$ . These results were used for calibration of data obtained by other samples. They demonstrate that front-end electronics

## Conclusion

used in this research is fully capable of processing low signals induced by impinging ions but emphasize the importance of low detector capacitance as well, since low capacitance of N1 is the main reason for its better energy resolution compared to D13.

The proposed technique based on IBIC detection has several advantages over the conventional deterministic implantation techniques, such as detection of secondary electrons and implantation from ion traps. Detection efficiency of 100 %, demonstrated for both for low energy protons and copper ions, is very difficult to achieve by detecting secondary electrons, especially for lighter, low energy ion species such as 50 keV N. While detection efficiency is not a problem for implantation from ion traps, since the ions are prepared in a deterministic way before the implantation itself, that technique relies on complicated and expensive equipment. Moreover, the implantation rate is low, due to the limited capacity of the ion traps. Whereas the technique proposed in this work is much more energy efficient and cost effective, being able to implant up to  $2 \times 10^5$  implants per implantation site in a matter of hours.

The proposed detector/preamplifier system demonstrated promising results and represents a big step towards fabrication of diamond-based quantum devices by ion beam implantation. However, there are still important issues to be solved. CCE for 140 keV Cu ions, although increased by lateral electric field, is still low. This is probably due to pulse height defect, characteristic for low energy heavy ions. Fortunately, this effect is not expected to be so prominent for nitrogen implantation. Nevertheless, the presented system should still be tested with low energy N ions to confirm the expected performance. For that purpose, a low energy ion implanter is currently being constructed at the Laboratory for Ion Beam Interactions at Ruder Bošković Institute. There is also space for improvement in noise reduction, mainly in reduction of thermal noise by cooling the preamplifier. The attempt to achieve this failed due to high background noise present at  $\mu$ Probe chamber. Therefore, a new experimental chamber, attached to the future ion implanter, should be designed for low noise measurements. Maybe the biggest obstacle in fabrication of diamond-based quantum devices is low efficiency in activation of the implanted ions and their conversion to functioning quantum centers. Without efficient activation of quantum centers there is no large-scale quantum device fabrication by ion beam implantation. Even though IBIC implantation offers no apparent solution for this problem, it can still help determine the parameters (such as number of ions implanted at each implantation site) for increasing the activation of implanted ions.

# Bibliography

- [1] P. W. Shor, “Algorithms for quantum computation: Discrete logarithms and factoring,” *Proc. - Annu. IEEE Symp. Found. Comput. Sci. FOCS*, pp. 124–134, 1994, doi: 10.1109/SFCS.1994.365700.
- [2] L. K. Grover, “A fast quantum mechanical algorithm for database search,” *Proc. Annu. ACM Symp. Theory Comput.*, vol. Part F129452, pp. 212–219, May 1996, doi: 10.48550/arxiv.quant-ph/9605043.
- [3] H. Sakhouf, M. Daoud, and R. Ahl Laamara, “Simple scheme for implementing the Grover search algorithm with superconducting qubits,” *J. Phys. B At. Mol. Opt. Phys.*, vol. 54, no. 17, p. 175501, Sep. 2021, doi: 10.1088/1361-6455/AC24AD.
- [4] A. Mandviwalla, K. Ohshiro, and B. Ji, “Implementing Grover’s Algorithm on the IBM Quantum Computers,” *Proc. - 2018 IEEE Int. Conf. Big Data, Big Data 2018*, pp. 2531–2537, Jan. 2019, doi: 10.1109/BIGDATA.2018.8622457.
- [5] R. P. Feynman, “Simulating Physics with Computers,” *Int. J. Theor. Phys.*, vol. 21, pp. 467–488, 1982.
- [6] F. Arute *et al.*, “Quantum supremacy using a programmable superconducting processor,” *Nat. 2019 5747779*, vol. 574, no. 7779, pp. 505–510, Oct. 2019, doi: 10.1038/s41586-019-1666-5.
- [7] I. L. Chuang, M. A. Nielsen, *Quantum Computation and Quantum Information*. New York: Cambridge University Press, 2000.
- [8] S. Schmitt *et al.*, “Submillihertz magnetic spectroscopy performed with a nanoscale quantum sensor,” *Science (80-. )*, vol. 356, no. 6340, pp. 832–837, May 2017, doi: 10.1126/SCIENCE.AAM5532.



## Bibliography

- [9] J. M. Boss *et al.*, “One- and Two-Dimensional Nuclear Magnetic Resonance Spectroscopy with a Diamond Quantum Sensor,” *Phys. Rev. Lett.*, vol. 116, no. 19, p. 197601, May 2016, doi: 10.1103/PhysRevLett.116.197601.
- [10] J. Wang *et al.*, “High-sensitivity temperature sensing using an implanted single nitrogen-vacancy center array in diamond,” *Phys. Rev. B*, vol. 91, no. 15, p. 155404, Apr. 2015, doi: 10.1103/PhysRevB.91.155404.
- [11] S. Hsieh *et al.*, “Imaging stress and magnetism at high pressures using a nanoscale quantum sensor,” *Science (80-. )*, vol. 366, no. 6471, pp. 1349–1354, Dec. 2019, doi: 10.1126/SCIENCE.AAW4352.
- [12] M. Pelliccione *et al.*, “Scanned probe imaging of nanoscale magnetism at cryogenic temperatures with a single-spin quantum sensor,” *Nat. Nanotechnol. 2016 118*, vol. 11, no. 8, pp. 700–705, May 2016, doi: 10.1038/nnano.2016.68.
- [13] J. Meinel *et al.*, “Heterodyne sensing of microwaves with a quantum sensor,” *Nat. Commun. 2021 121*, vol. 12, no. 1, pp. 1–8, May 2021, doi: 10.1038/s41467-021-22714-y.
- [14] P. Maletinsky *et al.*, “A robust scanning diamond sensor for nanoscale imaging with single nitrogen-vacancy centres,” *Nat. Nanotechnol. 2012 75*, vol. 7, no. 5, pp. 320–324, Apr. 2012, doi: 10.1038/nnano.2012.50.
- [15] R. Schirhagl, K. Chang, M. Loretz, and C. L. Degen, “Nitrogen-Vacancy Centers in Diamond: Nanoscale Sensors for Physics and Biology,” <http://dx.doi.org/10.1146/annurev-physchem-040513-103659>, vol. 65, pp. 83–105, Apr. 2014, doi: 10.1146/ANNUREV-PHYSCHEM-040513-103659.
- [16] D. Kim, M. I. Ibrahim, C. Foy, M. E. Trusheim, R. Han, and D. R. Englund, “A CMOS-integrated quantum sensor based on nitrogen–vacancy centres,” *Nat. Electron. 2019 27*, vol. 2, no. 7, pp. 284–289, Jul. 2019, doi: 10.1038/s41928-019-0275-5.
- [17] B. E. Kane, “A silicon-based nuclear spin quantum computer,” *Nat. 1998 3936681*, vol. 393, no. 6681, pp. 133–137, May 1998, doi: 10.1038/30156.
- [18] Y. Nakamura, Y. A. Pashkin, and J. S. Tsai, “Coherent control of macroscopic quantum states in a single-Cooper-pair box,” *Nature*, vol. 398, no. 6730, pp. 786–788, Apr. 1999, doi: 10.1038/19718.
- [19] Y. Nakamura, Y. A. Pashkin, and J. S. Tsai, “Rabi oscillations in a josephson-junction

## Bibliography

- charge two-level system,” *Phys. Rev. Lett.*, vol. 87, no. 24, pp. 246601-1-246601-4, Dec. 2001, doi: 10.1103/PHYSREVLETT.87.246601.
- [20] D. Castelvecchi, “Google’s quantum computer hits key milestone by reducing errors,” *Nature*, Feb. 22, 2023.
- [21] M. Steffen, D. P. Divincenzo, J. M. Chow, T. N. Theis, and M. B. Ketchen, “Quantum computing: An IBM perspective,” *IBM J. Res. Dev.*, vol. 55, no. 5, Sep. 2011, doi: 10.1147/JRD.2011.2165678.
- [22] V. Bouchiat, D. Vion, P. Joyez, D. Esteve, and M. H. Devoret, “Quantum coherence with a single cooper pair,” *Phys. Scr. T*, vol. 76, no. T76, pp. 165–170, Jan. 1998, doi: 10.1238/PHYSICA.TOPICAL.076A00165/XML.
- [23] J. D. Hidary, “Quantum Computing: An Applied Approach,” *Quantum Comput. An Appl. Approach*, 2019, doi: 10.1007/978-3-030-23922-0.
- [24] W. D. Oliver and P. B. Welander, “Materials in superconducting quantum bits,” *MRS Bull.*, vol. 38, no. 10, pp. 816–825, Oct. 2013, doi: 10.1557/MRS.2013.229.
- [25] J. I. Cirac and P. Zoller, “Quantum Computations with Cold Trapped Ions,” *Phys. Rev. Lett.*, vol. 74, no. 20, p. 4091, May 1995, doi: 10.1103/PhysRevLett.74.4091.
- [26] W. K. Hensinger, “Quantum computer based on shuttling trapped ions,” *Nat.* 2021 5927853, vol. 592, no. 7853, pp. 190–191, Apr. 2021, doi: 10.1038/d41586-021-00844-z.
- [27] T. Schenkel *et al.*, “Single ion implantation for solid state quantum computer development,” *Cit. J. Vac. Sci. Technol. B Microelectron. Nanom. Struct. Process.*, vol. 20, p. 2819, 2002, doi: 10.1116/1.1518016.
- [28] S. Pezzagna and J. Meijer, “Quantum computer based on color centers in diamond,” *Appl. Phys. Rev.*, vol. 8, no. 1, p. 011308, Feb. 2021, doi: 10.1063/5.0007444.
- [29] D. N. Jamieson *et al.*, “Controlled shallow single-ion implantation in silicon using an active substrate for sub-20-keV ions,” *Appl. Phys. Lett.*, vol. 86, no. 20, p. 202101, May 2005, doi: 10.1063/1.1925320.
- [30] T. Schenkel *et al.*, “Solid state quantum computer development in silicon with single ion implantation,” *J. Appl. Phys.*, vol. 94, p. 7017, 2003, doi: 10.1063/1.1622109.
- [31] J. Meijer *et al.*, “Concept of deterministic single ion doping with sub-nm spatial

## Bibliography

- resolution,” *Appl. Phys. A* 2006 832, vol. 83, no. 2, pp. 321–327, Feb. 2006, doi: 10.1007/S00339-006-3497-0.
- [32] A. M. Jakob *et al.*, “Deterministic Single Ion Implantation with 99.87% Confidence for Scalable Donor-Qubit Arrays in Silicon,” Sep. 2020, Accessed: Sep. 14, 2021. [Online]. Available: <http://arxiv.org/abs/2009.02892>.
- [33] B. Naydenov *et al.*, “Enhanced generation of single optically active spins in diamond by ion implantation,” *Appl. Phys. Lett.*, vol. 96, no. 16, p. 163108, Apr. 2010, doi: 10.1063/1.3409221.
- [34] S. D. Tchernij *et al.*, “Single-Photon-Emitting Optical Centers in Diamond Fabricated upon Sn Implantation,” *ACS Photonics*, vol. 4, no. 10, pp. 2580–2586, Oct. 2017, doi: 10.1021/ACSPHOTONICS.7B00904.
- [35] M. Di Paolo Emilio, “Diamond Thermal Solutions for High Power Electronics - EE Times Europe,” *EE Times Europe*, 2021.
- [36] G. S. Painter, D. E. Ellis, and A. R. Lubinsky, “*Ab Initio* Calculation of the Electronic Structure and Optical Properties of Diamond Using the Discrete Variational Method,” *Phys. Rev. B*, vol. 4, no. 10, p. 3610, Nov. 1971, doi: 10.1103/PhysRevB.4.3610.
- [37] A. Crnjac, N. Skukan, G. Provatas, M. Rodriguez-Ramos, M. Pomorski, and M. Jakšić, “Electronic Properties of a Synthetic Single-Crystal Diamond Exposed to High Temperature and High Radiation,” *Mater. 2020, Vol. 13, Page 2473*, vol. 13, no. 11, p. 2473, May 2020, doi: 10.3390/MA13112473.
- [38] M. Pillon *et al.*, “Radiation tolerance of a high quality synthetic single crystal chemical vapor deposition diamond detector irradiated by 14.8 MeV neutrons,” *J. Appl. Phys.*, vol. 104, no. 5, p. 054513, Sep. 2008, doi: 10.1063/1.2973668.
- [39] F. Pompili *et al.*, “Radiation and thermal stress test on diamond detectors for the Radial Neutron Camera of ITER,” *Nuclear Instruments and Methods in Physics Research, Section A: Accelerators, Spectrometers, Detectors and Associated Equipment*, vol. 936. Elsevier B.V., pp. 62–64, Aug. 21, 2019, doi: 10.1016/j.nima.2018.10.110.
- [40] S. Michimasa *et al.*, “Development of CVD diamond detector for time-of-flight measurements,” *Nucl. Instruments Methods Phys. Res. Sect. B Beam Interact. with Mater. Atoms*, vol. 317, no. PART B, pp. 710–713, Dec. 2013, doi: 10.1016/J.NIMB.2013.08.055.

## Bibliography

- [41] M. Pomorski *et al.*, “Development of single-crystal CVD-diamond detectors for spectroscopy and timing,” *Phys. status solidi*, vol. 203, no. 12, pp. 3152–3160, Sep. 2006, doi: 10.1002/PSSA.200671127.
- [42] E. Bossini and N. Minafra, “Diamond Detectors for Timing Measurements in High Energy Physics,” *Front. Phys.*, vol. 8, p. 538216, Jul. 2020, doi: 10.3389/FPHY.2020.00248/BIBTEX.
- [43] W. Zhu, “Defects in diamond,” in *Diamond: Electronic Properties and Applications*, New York: Springer Science+Business Media, 1995, pp. 175–240.
- [44] T. Iwasaki *et al.*, “Tin-Vacancy Quantum Emitters in Diamond,” *Phys. Rev. Lett.*, vol. 119, no. 25, p. 253601, Dec. 2017, doi: 10.1103/PHYSREVLETT.119.253601/FIGURES/4/MEDIUM.
- [45] Z. Ju, J. Lin, S. Shen, B. Wu, and E. Wu, “Preparations and applications of single color centers in diamond,” <https://doi.org/10.1080/23746149.2020.1858721>, vol. 6, no. 1, p. 1858721, 2021, doi: 10.1080/23746149.2020.1858721.
- [46] F. C. Waldermann *et al.*, “Creating diamond color centers for quantum optical applications,” *Diam. Relat. Mater.*, vol. 16, no. 11, pp. 1887–1895, Nov. 2007, doi: 10.1016/J.DIAMOND.2007.09.009.
- [47] P. Olivero *et al.*, “Focused ion beam fabrication and IBIC characterization of a diamond detector with buried electrodes,” *Nucl. Instruments Methods Phys. Res. Sect. B Beam Interact. with Mater. Atoms*, vol. 269, no. 20, pp. 2340–2344, Oct. 2011, doi: 10.1016/J.NIMB.2011.02.021.
- [48] J. Forneris *et al.*, “Electroluminescence from a diamond device with ion-beam-micromachined buried graphitic electrodes,” *Nucl. Instruments Methods Phys. Res. Sect. B Beam Interact. with Mater. Atoms*, vol. 348, pp. 187–190, Apr. 2015, doi: 10.1016/J.NIMB.2014.12.036.
- [49] R. Kalish, “Ion-implantation in diamond and diamond films: doping, damage effects and their applications,” *Appl. Surf. Sci.*, vol. 117–118, pp. 558–569, Jun. 1997, doi: 10.1016/S0169-4332(97)80142-0.
- [50] H. Hofsäss, H. Binder, T. Klumpp, and E. Recknagel, “Doping and growth of diamond-like carbon films by ion beam deposition,” *Diam. Relat. Mater.*, vol. 3, no. 1–2, pp. 137–142, Jan. 1994, doi: 10.1016/0925-9635(94)90045-0.

## Bibliography

- [51] S. P. Mehandru and A. B. Anderson, “Adsorption of H, CH<sub>3</sub>, CH<sub>2</sub> and C<sub>2</sub>H<sub>2</sub> on 2 × 1 restructured diamond (100): Theoretical study of structures, bonding, and migration,” *Surf. Sci.*, vol. 248, no. 3, pp. 369–381, Jun. 1991, doi: 10.1016/0039-6028(91)91183-X.
- [52] J. Van Der Weide and R. J. Nemanich, “Influence of interfacial hydrogen and oxygen on the Schottky barrier height of nickel on (111) and (100) diamond surfaces,” *Phys. Rev. B*, vol. 49, no. 19, p. 13629, May 1994, doi: 10.1103/PhysRevB.49.13629.
- [53] W. F. Wei and W. J. Leivo, “Photoelectric emission and work function of semiconducting diamonds,” *Carbon N. Y.*, vol. 13, no. 5, pp. 425–427, Jan. 1975, doi: 10.1016/0008-6223(75)90013-5.
- [54] “Ultra Rare Diamond Suggests Earth’s Mantle Has an Ocean’s Worth of Water - Scientific American.” <https://www.scientificamerican.com/article/oceans-worth-of-water-hidden-deep-in-earth-ultra-rare-diamond-suggests/> (accessed Jun. 29, 2023).
- [55] Y. Zhang *et al.*, “HPHT synthesis of large single crystal diamond doped with high nitrogen concentration,” *Diam. Relat. Mater.*, vol. 17, no. 2, pp. 209–211, Feb. 2008, doi: 10.1016/J.DIAMOND.2007.12.018.
- [56] F. N. Faili (Element Six), “Understanding Diamond As A Material For RF Packaging,” *RF Globalnet*, 2018.
- [57] S. Koizumi, H. Umezawa, J. Pernot, and M. Suzuki, “Power Electronics Device Applications of Diamond Semiconductors,” *Power Electron. Device Appl. Diam. Semicond.*, pp. 1–452, Jan. 2018, doi: 10.1016/C2016-0-03999-2.
- [58] N. Vaissiere, S. Saada, M. Bouttemy, A. Etcheberry, P. Bergonzo, and J. C. Arnault, “Heteroepitaxial diamond on iridium: New insights on domain formation,” *Diam. Relat. Mater.*, vol. 36, pp. 16–25, Jun. 2013, doi: 10.1016/J.DIAMOND.2013.03.010.
- [59] K. Ohtsuka, K. Suzuki, A. Sawabe, and T. Inuzuka, “Epitaxial growth of diamond on iridium,” *Japanese J. Appl. Physics, Part 2 Lett.*, vol. 35, no. 8 SUPPL. B, p. L1072, Aug. 1996, doi: 10.1143/JJAP.35.L1072/XML.
- [60] M. Nakhostin, “Signal processing for radiation detectors,” *Signal Process. Radiat. Detect.*, pp. 1–528, Nov. 2017, doi: 10.1002/9781119410225.
- [61] H. Bethe, “Zur Theorie des Durchgangs schneller Korpuskularstrahlen durch Materie,” *Ann. Phys.*, vol. 397, no. 3, pp. 325–400, Jan. 1930, doi: 10.1002/ANDP.19303970303.

## Bibliography

- [62] M. B. H. Breese, D. N. Jamieson, and P. J. C. Kind, *Materials Analysis Using a Nuclear Microprobe*, no. 1. New York: John Wiley & Sons, Ltd, 1996.
- [63] J. Lindhard and A. H. Sørensen, “Relativistic theory of stopping for heavy ions,” *Phys. Rev. A*, vol. 53, no. 4, p. 2443, Apr. 1996, doi: 10.1103/PhysRevA.53.2443.
- [64] “James Ziegler - SRIM & TRIM.” <http://www.srim.org/> (accessed Dec. 21, 2021).
- [65] R. E. Faw, J. K. Shultis, *Radiation Shielding*. American Nuclear Society, La Grange Park, IL, 2000.
- [66] J. Lilley, *Nuclear Physics, Principles and Applications*. Wiley-VCH, ISBN 0-471-97935-X, 2001.
- [67] “<http://nucleardata.nuclear.lu.se/toi/nuclide.asp?iZA=950241>.” [Online]. Available: <http://nucleardata.nuclear.lu.se/toi/nuclide.asp?iZA=950241>.
- [68] B. G. Lowe and R. A. Sareen, *Semiconductor X-ray detectors*. Boca Raton: CRC Press, 2013.
- [69] W. Shockley, “Currents to Conductors Induced by a Moving Point Charge,” *J. Appl. Phys.*, vol. 9, no. 10, pp. 635–636, Oct. 1938, doi: 10.1063/1.1710367.
- [70] S. Ramo, “Currents Induced by Electron Motion,” *Proc. IRE*, vol. 27, no. 9, pp. 584–585, 1939, doi: 10.1109/JRPROC.1939.228757.
- [71] L. Bardelli and G. Poggi, “Digital-sampling systems in high-resolution and wide dynamic-range energy measurements: Comparison with peak sensing ADCs,” *Nucl. Instruments Methods Phys. Res. Sect. A Accel. Spectrometers, Detect. Assoc. Equip.*, vol. 560, no. 2, pp. 517–523, May 2006, doi: 10.1016/J.NIMA.2005.12.249.
- [72] M. Flaska, M. Faisal, D. D. Wentzloff, and S. A. Pozzi, “Influence of sampling properties of fast-waveform digitizers on neutron-gamma-ray, pulse-shape discrimination for organic scintillation detectors,” *Nucl. Instruments Methods Phys. Res. Sect. A Accel. Spectrometers, Detect. Assoc. Equip.*, vol. 729, pp. 456–462, 2013, doi: 10.1016/J.NIMA.2013.07.008.
- [73] J. M. Los Arcos and E. García-Toraño, “A new digital pulse height analysis method for radiation spectroscopy,” *Nucl. Instruments Methods Phys. Res. Sect. A Accel. Spectrometers, Detect. Assoc. Equip.*, vol. 339, no. 1–2, pp. 99–101, Jan. 1994, doi: 10.1016/0168-9002(94)91786-8.

## Bibliography

- [74] M. Pomorski, “Electronic properties of single crystal CVD diamond and its suitability for particle detection in hardron physics experiments,” 2008.
- [75] W. Shockley and W. T. Read, “Statistics of the Recombinations of Holes and Electrons,” *Phys. Rev.*, vol. 87, no. 5, p. 835, Sep. 1952, doi: 10.1103/PhysRev.87.835.
- [76] C. Da Via *et al.*, “Advances in silicon detectors for particle tracking in extreme radiation environments,” *Nucl. Instruments Methods Phys. Res. Sect. A Accel. Spectrometers, Detect. Assoc. Equip.*, vol. 509, no. 1–3, pp. 86–91, Aug. 2003, doi: 10.1016/S0168-9002(03)01554-7.
- [77] E. Albuquerque *et al.*, “A Full Current-Mode Timing Circuit with Dark Noise Suppression for the CERN CMS Experiment,” *ESSCIRC 2022 - IEEE 48th Eur. Solid State Circuits Conf. Proc.*, pp. 177–180, 2022, doi: 10.1109/ESSCIRC55480.2022.9911529.
- [78] P. Kavrigin, P. Finocchiaro, E. Griesmayer, E. Jericha, A. Pappalardo, and C. Weiss, “Pulse-shape analysis for gamma background rejection in thermal neutron radiation using CVD diamond detectors,” *Nucl. Instruments Methods Phys. Res. Sect. A Accel. Spectrometers, Detect. Assoc. Equip.*, vol. 795, pp. 88–91, Jun. 2015, doi: 10.1016/j.nima.2015.05.040.
- [79] G. Kramberger *et al.*, “Investigation of irradiated silicon detectors by edge-TCT,” *IEEE Trans. Nucl. Sci.*, vol. 57, no. 4 PART 2, pp. 2294–2302, Aug. 2010, doi: 10.1109/TNS.2010.2051957.
- [80] “XGLab CUBE | The CMOS Preamplifier for Radiation Detectors.” <https://www.xglab.it/products/cube/> (accessed Mar. 29, 2023).
- [81] H. Pernegger *et al.*, “Radiation hard monolithic CMOS sensors with small electrodes for High Luminosity LHC,” *Nucl. Instruments Methods Phys. Res. Sect. A Accel. Spectrometers, Detect. Assoc. Equip.*, vol. 986, p. 164381, Jan. 2021, doi: 10.1016/J.NIMA.2020.164381.
- [82] H. Spieler, “Semiconductor Detector Systems,” *Semicond. Detect. Syst.*, vol. 9780198527, pp. 1–478, 2007, doi: 10.1093/acprof:oso/9780198527848.001.0001.
- [83] M. Vicentijevic, M. Jaksic, G. Provatas, and T. Suligoj, “Detection of Low-Penetrating Ions in Diamond at Room Temperature,” *IEEE Trans. Nucl. Sci.*, vol. 69, no. 11, pp. 2252–2261, Nov. 2022, doi: 10.1109/TNS.2022.3208929.

## Bibliography

- [84] E. Simoen *et al.*, “Radiation effects in advanced multiple gate and silicon-on-insulator transistors,” *IEEE Trans. Nucl. Sci.*, vol. 60, no. 3, pp. 1970–1991, 2013, doi: 10.1109/TNS.2013.2255313.
- [85] V. V. Gostilo, “Low-noise electronics for semiconductor detectors,” *Nucl. Instruments Methods Phys. Res. Sect. A Accel. Spectrometers, Detect. Assoc. Equip.*, vol. 322, no. 3, pp. 566–568, Nov. 1992, doi: 10.1016/0168-9002(92)91233-Y.
- [86] M. W. Lund, K. W. Decker, R. T. Perkins, and J. D. Phillips, “Low noise JFETs for room temperature x-ray detectors,” *Nucl. Instruments Methods Phys. Res. Sect. A Accel. Spectrometers, Detect. Assoc. Equip.*, vol. 380, no. 1–2, pp. 318–322, Oct. 1996, doi: 10.1016/S0168-9002(96)00473-1.
- [87] J. Hao, L. He, and Z. Deng, “A cryogenic low-background low-noise CMOS preamplifier for HPGe detectors,” *J. Instrum.*, vol. 17, no. 06, p. P06018, Jun. 2022, doi: 10.1088/1748-0221/17/06/P06018.
- [88] G. Gramegna, P. O’Connor, P. Rehak, and S. Hart, “Low-noise CMOS preamplifier-shaper for silicon drift detectors,” *IEEE Trans. Nucl. Sci.*, vol. 44, no. 3 PART 1, pp. 385–388, 1997, doi: 10.1109/23.603676.
- [89] J. Bieger and H. Seifert, “A Low-Noise CMOS Preamplifier Operating at 4.2 K,” *IEEE J. Solid-State Circuits*, vol. 29, no. 8, pp. 921–926, 1994, doi: 10.1109/4.297696.
- [90] P. O’Connor, G. Gramegna, P. Rehak, F. Corsi, and C. Marzocca, “Ultra Low Noise CMOS preamplifier-shaper for X-ray spectroscopy,” *Nucl. Instruments Methods Phys. Res. Sect. A Accel. Spectrometers, Detect. Assoc. Equip.*, vol. 409, no. 1–3, pp. 315–321, May 1998, doi: 10.1016/S0168-9002(97)01289-8.
- [91] R. Cardella *et al.*, “MALTA: an asynchronous readout CMOS monolithic pixel detector for the ATLAS High-Luminosity upgrade,” *J. Instrum.*, vol. 14, no. 06, p. C06019, Jun. 2019, doi: 10.1088/1748-0221/14/06/C06019.
- [92] I. Bogdanović Radović, “Ruđer Bošković Institute Accelerator Facility,” <https://doi.org/10.1080/10619127.2020.1752087>, vol. 30, no. 2, pp. 4–9, Apr. 2020, doi: 10.1080/10619127.2020.1752087.
- [93] M. Jakšić *et al.*, “New capabilities of the Zagreb ion microbeam system,” *Nucl. Instruments Methods Phys. Res. Sect. B Beam Interact. with Mater. Atoms*, vol. 260, no. 1, pp. 114–118, Jul. 2007, doi: 10.1016/J.NIMB.2007.01.252.



## Bibliography

- [94] D. Cosic, M. Bogovac, and M. Jakšić, “Data acquisition and control system for an evolving nuclear microprobe,” *Nucl. Instruments Methods Phys. Res. Sect. B Beam Interact. with Mater. Atoms*, vol. 451, pp. 122–126, Jul. 2019, doi: 10.1016/J.NIMB.2019.05.047.
- [95] A. Crnjac, “Influence of radiation and high temperatures on electronic properties of diamond detectors,” University of Zagreb, 2022.
- [96] M. Vićentijević, M. Jakšić, and T. Suligoj, “Implantation site design for large area diamond quantum device fabrication,” *Sci. Reports 2023 131*, vol. 13, no. 1, pp. 1–8, Aug. 2023, doi: 10.1038/s41598-023-40785-3.
- [97] “A250 Charge Sensitive Preamplifier – Amptek – X-Ray Detectors and Electronics.” <https://www.amptek.com/internal-products/a250-charge-sensitive-preamplifier> (accessed Jul. 28, 2023).
- [98] “Table of Isotopes decay data.” <http://nucleardata.nuclear.lu.se/toi/nuclide.asp?iZA=950241> (accessed Dec. 21, 2021).
- [99] A. Fidanzio, G. Stimato, L. Azario, and A. Piermattei, “Investigation of natural diamond detector priming effect during electron beam irradiation,” *Nucl. Instruments Methods Phys. Res. Sect. B Beam Interact. with Mater. Atoms*, vol. 245, no. 2, pp. 421–426, Apr. 2006, doi: 10.1016/J.NIMB.2005.11.051.
- [100] “COMSOL Multiphysics® Software - Understand, Predict, and Optimize.” <https://www.comsol.com/comsol-multiphysics> (accessed Apr. 06, 2023).
- [101] E. Vittone, F. Fizzotti, A. Lo Giudice, C. Paolini, and C. Manfredotti, “Theory of ion beam induced charge collection in detectors based on the extended Shockley–Ramo theorem,” *Nucl. Instruments Methods Phys. Res. Sect. B Beam Interact. with Mater. Atoms*, vol. 161–163, pp. 446–451, Mar. 2000, doi: 10.1016/S0168-583X(99)01000-9.
- [102] D. A. Broadway *et al.*, “Spatial mapping of band bending in semiconductor devices using in situ quantum sensors,” *Nat. Electron. 2018 19*, vol. 1, no. 9, pp. 502–507, Sep. 2018, doi: 10.1038/s41928-018-0130-0.
- [103] J. Henshaw *et al.*, “Nanoscale solid-state nuclear quadrupole resonance spectroscopy using depth-optimized nitrogen-vacancy ensembles in diamond,” *Appl. Phys. Lett.*, vol. 120, no. 17, p. 174002, Apr. 2022, doi: 10.1063/5.0083774.
- [104] B. D. Wilkins, M. J. Fluss, S. B. Kaufman, C. E. Gross, and E. P. Steinberg, “Pulse-

## Bibliography

- height defects for heavy ions in a silicon surface-barrier detector,” *Nucl. Instruments Methods*, vol. 92, no. 3, pp. 381–391, Apr. 1971, doi: 10.1016/0029-554X(71)90414-9.
- [105] B. Aspacher and A. C. Rester, “Compton continuum suppression by analog pulse shape analysis,” *Nucl. Instruments Methods Phys. Res. Sect. A Accel. Spectrometers, Detect. Assoc. Equip.*, vol. 338, no. 2–3, pp. 511–515, Jan. 1994, doi: 10.1016/0168-9002(94)91335-8.

# Biography

Milan Vićentijević was born in Belgrade, Serbia, on 30. October 1991. He finished primary school in Belgrade and secondary school at “Katedralskolan” in Lund, Sweden, in 2011, after which he started his studies in Electrical Engineering and Computing at the School of Electrical Engineering and Computing at the University of Belgrade. He received his BSc in 2015. with a thesis entitled “Virtual source model for field effect transistors”, and MSc in 2016. with the final thesis entitled “Modification of 2D Material Exfoliation Methods and Fabrication of Van der Waals Heterostructures”. The research for the thesis was done at Institute of Physics in Belgrade, Serbia. Since 2017. he is working at the Laboratory for Ion Beam Interactions at Ruđer Bošković Institute as a professional associate, on designing control systems for particle accelerators. He participated in several international conferences and contributed to five research articles, two of which as the main author.

## List of publications

1. D. Verheij, Milan Vićentijević, Milko Jakšić, Marco Peres, Luís Cerqueira Alves, Susana Cardoso, Eduardo Alves, Christophe Durand, Joël Eymery, Wolfhard Möller, and Katharina Lorenz, “Charge Collection Efficiency of Single GaN Core–Shell Wires Assessed by High-Precision Ion-Beam-Induced Charge Measurements,” *ACS Appl. Electron. Mater.*, Feb. 2024, doi: 10.1021/ACSAELM.3C01584.
2. M. Vićentijević, M. Jakšić, and T. Suligoj, “Implantation site design for large area diamond quantum device fabrication,” *Sci. Reports* 2023 131, vol. 13, no. 1, pp. 1–8, Aug. 2023, doi: 10.1038/s41598-023-40785-3.

## Biography

3. T. Tadić, T. Dunatov, S. Fazinić, D. D. Cosic, M. Jakšić, Z. Siketić, M. Vićentijević, W. Kada and C. D. Hardie, “Development of the Dual-Beam Ion Irradiation Facility for Fusion Materials (DiFU),” *Mater.* 2023, Vol. 16, Page 1144, vol. 16, no. 3, p. 1144, Jan. 2023, doi: 10.3390/MA16031144.
4. M. Vićentijević, M. Jaksic, G. Provatas, and T. Suligoj, “Detection of Low-Penetrating Ions in Diamond at Room Temperature,” *IEEE Trans. Nucl. Sci.*, vol. 69, no. 11, pp. 2252–2261, Nov. 2022, doi: 10.1109/TNS.2022.3208929.
5. M. Pezzarossa, E. Cepparrone, D. Cosic, M. Jakšić, G. Provatas, M. Vićentijević and E. Vittone, “Polychromatic angle resolved IBIC analysis of silicon power diodes,” *Nucl. Instruments Methods Phys. Res. Sect. B Beam Interact. with Mater. Atoms*, vol. 488, pp. 50–63, Feb. 2021, doi: 10.1016/J.NIMB.2020.12.006.
6. M. Jakšić, D. D. Cosic, A. Crnjac, S. Fazinić, V. Grilj, W. Kada, G. Provatas, N. Skukan and M. Vićentijević, “In situ irradiation and IBIC probing using pulsed and dual ion microbeams,” *Nucl. Instruments Methods Phys. Res. Sect. B Beam Interact. with Mater. Atoms*, vol. 456, pp. 49–52, Oct. 2019, doi: 10.1016/J.NIMB.2019.06.037.

## List of conference contributions

1. M. Jakšić, D. Cosic, A. Crnjac, G. Provatas and M. Vićentijević, “IBIC Characterisation of Single Crystal Diamond Devices Operating in Extreme Conditions”, International Conference on Materials for Advanced Technologies ICMAT, A-2603, 2023.
2. A. Crnjac, M. Rodriguez Ramos, G. Provatas, M. Vićentijević and M. Jakšić, “scCVD diamond detector signal properties investigated with ion microbeams at elevated temperatures”, Advanced Diamond Assemblies Workshop, ADAMAS, 2019.
3. M. Vukšić, T. Tadić, S. Fazinić, M. Jakšić, A. Kovačić, Ž. Periša, Z. Siketić, N. Skukan, D. Španja, M. Vićentijević, D. D. Čosić, Z. Kolar, M. Capor, R. Gracin, W. Kada and C. Hardie, “Development of the Dual-beam ion irradiation facility for FUSion materials (DiFU) at RBI, Zagreb”, European Conference on Accelerators in Applied Research and Technology, P-B-30, 1, 2019.
4. M. Vićentijević, M. Jakšić and T. Suligoj, “Detection of Single Low-Penetrating Ions in Diamond”, 26th International Conference on the Application of Accelerators in Research and Industry, SN-STDS-01, 106, 2022.
5. T. Dunatov, T. Tadić, S. Fazinić, M. Jakšić, Z. Siketić, M. Vićentijević, D. D. Cosic, Z. Kolar, M. Capor, R. Gracin and C. Hardie, “Development and operation of the Dual-

## Biography

beam ion irradiation facility for FUsion materials (DiFU) at RBI, Zagreb”, 32nd Symposium on Fusion Technologies, 2022.

6. M. Vićentijević, M. Jakšić, Z. Siketić, G. Provatas and T. Suligoj, “Detection of Single Low-Penetrating Ions in Diamond”, 22nd International Conference on Ion Beam Modification of Materials, ABS: 149, 2022.
7. A. Crnjac, M. Jakšić, M. Rodriguez Ramos, M. Vićentijević and G. Provatas, “Spectroscopic properties and radiation hardness of scCVD diamond detectors investigated at elevated temperatures using MeV ion microbeam”, SBDD XXV - Hasselt Diamond Workshop, 2020.

# Životopis

Milan Vićentijević rođen je u Beogradu, u Srbiji, 30.10.1991. Osnovnu školu završio je u Beogradu a srednju “Katedralskolan” u Lundu, u Švedskoj, 2011. godine, te potom upisuje studij elektrotehnike i računarstva na Elektrotehničkom fakultetu Sveučilišta u Beogradu. Diplomirao je 2015. godine na temu “Model virtualnog sourcea za tranzistore sa efektom polja”, te magistrirao 2016. godine na temu “Modifikacije metode mehaničke eksfolijacije 2D materijala i tehnika fabrikacije Van der Waalsovih heterostruktura”. Istraživanje za završni rad sprovedeno je na Institutu za fiziku u Beogradu, u Srbiji. Od 2017. godine radi u Laboratoriju za interakcije ionskih snopova na Institutu Ruđer Bošković kao stručni suradnik. Sudjelovao je na nekolicini međunarodnih konferencija, te je autor i koautor pet radova objavljenih u časopisima sa međunarodnom recenzijom.